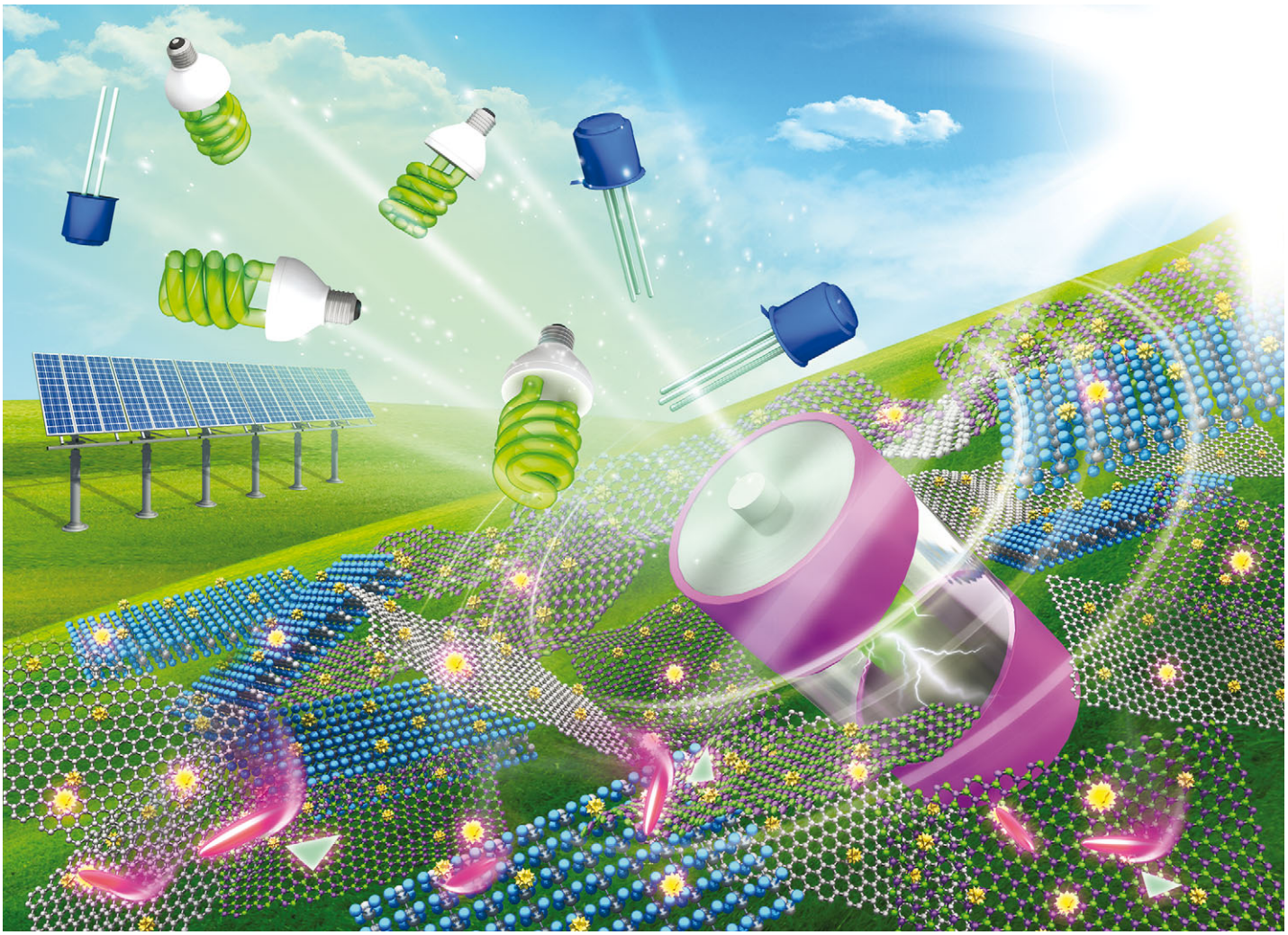

Featuring work from the research group of Professor Bingqing Wei, Northwestern Polytechnical University, Xi'an, China and University of Delaware, Newark, USA.

Hybrid nanostructures of metal/two-dimensional nanomaterials for plasmon-enhanced applications

Hybrid nanostructures composed of 2D nanomaterials and plasmonic metals have been extensively studied. This review discusses the preparation, optical properties and plasmon-enhanced applications of metal/2D material hybrid nanostructures.

As featured in:

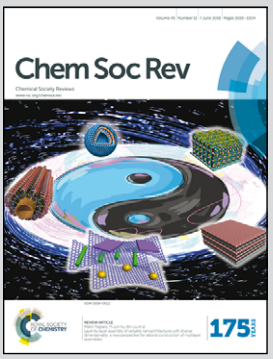

See Bingqing Wei *et al.*, *Chem. Soc. Rev.*, 2016, **45**, 3145.

ROYAL SOCIETY OF CHEMISTRY

www.rsc.org/chemsocrev

Registered charity number: 207890

Chem Soc Rev

REVIEW ARTICLE

View Article Online
View Journal | View Issue

Cite this: *Chem. Soc. Rev.*, 2016, **45**, 3145

Hybrid nanostructures of metal/two-dimensional nanomaterials for plasmon-enhanced applications

Xuanhua Li,[a] Jinmeng Zhu[a] and Bingqing Wei*[ab]

Received 9th March 2016

DOI: 10.1039/c6cs00195e

www.rsc.org/chemsocrev

Hybrid nanostructures composed of graphene or other two-dimensional (2D) nanomaterials and plasmonic metal components have been extensively studied. The unusual properties of 2D materials are associated with their atomically thin thickness and 2D morphology, and many impressive structures enable the metal nanomaterials to establish various interesting hybrid nanostructures with outstanding plasmonic properties. In addition, the hybrid nanostructures display unique optical characteristics that are derived from the close conjunction of plasmonic optical effects and the unique physicochemical properties of 2D materials. More importantly, the hybrid nanostructures show several plasmonic electrical effects including an improved photogeneration rate, efficient carrier transfer, and a plasmon-induced "hot carrier", playing a significant role in enhancing device performance. They have been widely studied for plasmon-enhanced optical signals, photocatalysis, photodetectors (PDs), and solar cells. In this review, the developments in the field of metal/2D hybrid nanostructures are comprehensively described. Preparation of hybrid nanostructures is first presented according to the 2D material type, as well as the metal nanomaterial morphology. The plasmonic properties and the enabled applications of the hybrid nanostructures are then described. Lastly, possible future research in this promising field is discussed.

1. Introduction

Two-dimensional (2D) nanosheets as emerging nanomaterials exhibit unique properties that originate from their atomically thin thickness and 2D morphological features, such as a high surface area and specific physicochemical properties, making them promising building blocks and platforms for both

[a] *Center for Nano Energy Materials, State Key Laboratory of Solidification Processing, School of Materials Science and Engineering, Northwestern Polytechnical University, Xi'an, 710072, China. E-mail: weib@udel.edu*
[b] *Department of Mechanical Engineering, University of Delaware, Newark, DE19716, USA*

Xuanhua Li

Xuanhua Li received his BS degree from the Wuhan University of Technology in 2007, and MS degree from USTC in 2010. After that, he started his doctoral studies under the direction of Dr Wallace Choy and received a PhD degree at HKU in 2014. After a brief research at the Institute of Intelligent Machines, CAS, he began his career at the Center for Nano Energy Materials, Northwestern Polytechnical University as a professor. His research is focused on the synthesis of 2D nanomaterials and novel metal NPs. He is also interested in plasmon-enhanced solar cells, photocatalytic reactions, and optical sensors.

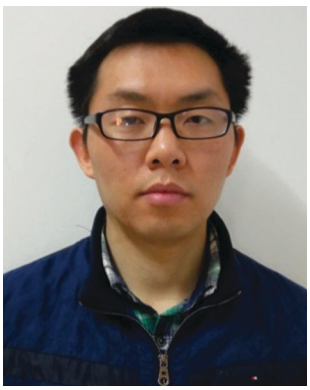

Jinmeng Zhu

Jinmeng Zhu received his bachelor's degree in Mineral Processing and Engineering at Henan Polytechnic University in 2008. Then, he moved to the Xi'an University of Science and Technology to do research on the SiO_2 aerogel and received his master's degree in 2012. During post-graduation, he developed great interest in the synthesis and application of nanomaterials. Now, he is pursuing his doctoral degree at Northwestern Polytechnical University under the supervision of Professor Bingqing Wei and Professor Xuanhua Li. His research focuses on the synthesis and related applications of two-dimensional nanosheets (e.g. graphene, BN, MoS_2) and their hybrids.

scientific studies and technological development.[1–7] As typical examples, graphene and graphene oxide (GO) demonstrate various applications in photovoltaic devices, photocatalysis, batteries, supercapacitors, sensors, fuel cells, and surface-enhanced Raman scattering (SERS), exhibiting superior performances compared to other conventional nanomaterials, such as inorganic metal oxide and organic semiconductors.[8–18] Recently, 2D MX_2 type nanomaterials (M = W, Mo, Ta, Ti, Nb, Re, *etc.*; X = Se, S, Te), *i.e.*, transition metal dichalcogenides (TMDs), have also gained significant attention due to their interesting optical and electrical properties.[17,18] To date, TMDs have been extensively studied in photoelectronic devices, sensors, photocatalytic reactions, and emitters.[19–25] In addition, other types of 2D materials are increasingly reported, such as phosphorene, graphitic carbon nitride (g-C_3N_4), boron nitride (BN), silicene, transition metal oxides, germanene, borophene, and atomically thin 2D perovskites, and have received considerable research interest due to their unique optical, mechanical, chemical, and electronic properties in the past few years.[26–33]

However, the thickness of graphene and other 2D materials is too thin to absorb sufficient light, which inevitably restricts their efficient applications, in particular for some light-driven-related applications, such as photocatalytic reactions, optical sensors, optoelectronics, and visual images.[1,34–40] Specifically, their light absorption is only 2.3% and 5.6% for graphene monolayers and MoS_2 monolayers, respectively, which is considerably weak compared to the bulk materials.[3] Thus, efficiently enhancing the light absorption of 2D materials to satisfy the requirements of practical applications has become an important issue.[36–42] Among promising strategies, integration of plasmonic metal nanomaterials with 2D materials to form hybrid nanostructures of plasmonic metal/2D materials has attracted much interest. One main reason for integrating 2D materials with plasmonic metal nanomaterials is to enhance light absorption through the plasmonic effect of the metal component and then to channel the absorbed light energy to the 2D material part for technologically important light-involved applications, such as photocatalysis, optical sensing, and optoelectronics.[43–59] In addition, the plasmonic electrical effects, including an enhanced photogeneration rate, the plasmon-induced "hot electrons", and improved conductivity of the hybrid nanostructures, also play a significant role in enhancing the photocatalytic reactions and the performance of photoelectric devices.[60–62] Furthermore, the combination of two individual properties derived from the metal and the 2D material with different functionalities into one hybrid nanostructure system also provides an attractive, multifunctional platform with enhanced performance for various applications in biotechnology and medicine.[63,64] Moreover, the production of new physical phenomena is interesting and worthwhile for researchers to study.[40,65,66]

Here, we provide an overview of the recent research on the hybrid nanostructures of plasmonic metal/2D materials, including their preparation, unique optical properties, and plasmon-enhanced applications in optical sensors, photocatalytic reactions, and photoelectronics. In this review article, the following points should be noted. (1) Two types of metal nanomaterials including metal nanoparticles (NPs) (*i.e.*, clear-cut nanospheres, nanocubes, nanowires, nanorods, *etc.*) and noble metal nanostructures (*i.e.*, periodic patterns and rough metal films) are included because both of them have been intensively studied in the hybrid nanostructures of metal/2D materials. (2) Only plasmonic metals possessing strong plasmonic effects such as Au, Ag, Cu, and Al are discussed. Other plasmonic metals, such as Pt and Pd, are not included here.

2. Preparation of hybrid nanostructures of metal/2D materials

As we discussed in the Introduction section, the integration of metal nanomaterials into graphene and other 2D materials can further optimize and efficiently enhance the optical properties of 2D materials as well as improve their applications in a wide variety of fields. Thus, preparation of efficient hybrid nanostructures, such as Ag NPs/graphene,[67] Au NPs/GO,[68] and Cu NPs/GO,[69] is extremely important. In general, a particular application decides the method used to build the hybrid nanostructures of metals and 2D materials. Several key points should be considered to make efficient hybrid nanostructures when integrating the metal nanomaterials and 2D materials together. First, the pre-prepared metal nanomaterials should have a strong plasmonic effect and the pre-prepared 2D materials should have good physical and chemical properties depending on a particular application (*i.e.*, mobility, conductivity, absorbance, mechanical flexibility, and specific surface area). Second, the overall configuration of hybrid nanostructures and mutual contacts between these two types of materials should be extensively considered. The interface design between the metal nanomaterials and the 2D materials is dependent on a particular application. Taking a plasmon-enhanced optical signal device as an example, an insulator layer should be

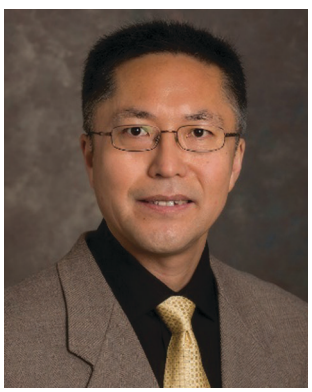

Bingqing Wei

Dr Bingqing Wei is a Professor in the Department of Mechanical Engineering at the University of Delaware, USA. He was an Assistant Professor in the Department of Electrical & Computer Engineering and Center for Computation & Technology at Louisiana State University from 2003 to 2007. He was a Research Scientist at Rensselaer Polytechnic Institute, Department of Materials Science and Engineering and Rensselaer Nanotechnology Center from 2000 to 2003. Dr Wei was a visiting scientist at Max-Planck-Institut für Metallforschung, Stuttgart, Germany in 1998 and 1999. From 1992 to 2001, he was a faculty member at Tsinghua University in Beijing.

inserted between the two components when the hybrid nanostructures are designed so that electron transfer between the metal nanomaterials and the 2D materials is restrained.[53,70,71] In contrast, the two components should be in tight contact with each other for smooth electron transfer. Third, damage to the surface and structure of the two parts should be avoided during the integration process.

In this section, various methods for the preparation of hybrid nanostructures of metal/graphene and other 2D materials developed recently are reviewed. Development of each component, such as metal NPs, metal nanostructures, as well as 2D materials, has been discussed in literature and will not be included in this report.[5,19–21,23,48,54,72,73] To facilitate the discussion, the hybrid nanostructures of metal/2D materials are divided into two parts, the hybrid nanostructures of metal NPs/2D materials and the hybrid nanostructures of metal nanostructures/2D materials. In the discussion of each part, the preparation of metal/graphene composites is first reviewed as the majority of the discussion, followed by the preparation of metal/other 2D materials.

2.1 Preparation of hybrid nanostructures of metal NPs/2D materials

The hybrid nanostructures of metal NPs/2D materials are commonly used in SERS and photocatalytic reactions, and as the interlayers of solar cells.[74–81] There are certain preparation requirements for specific applications, such as a large surface area for SERS and photocatalytic reactions, and solution processing for the interlayers of solar cells. To better attain the application requirements, many methods have been developed for fabricating these hybrid nanostructures. Here, six typical methods are discussed, including physical deposition, chemical reduction, photocatalytic reduction, an electrochemical method, a solvothermal method, and wave-assisted reduction.

2.1.1 Physical deposition to synthesize the hybrid nanostructures of metal NPs/2D materials. Physical deposition is a convenient method that can rapidly and efficiently deposit metal NPs on 2D nanosheets.[82,83] Sputter deposition, electron-beam evaporation, and thermal evaporation are three main physical deposition methods.[82,83] 2D materials need to be synthesized first, followed by conversion of the bulk metal into small metal NPs in a vacuum or an inert atmosphere to construct the hybrid nanostructures of metal NPs/2D materials. Hybrids of metal NPs/2D materials with different densities, shapes, and thicknesses of metal NPs can be obtained using this method, which is very beneficial for tuning the plasmonic effect.[84–86] Wilson *et al.* performed the deposition of Au or Ag NPs on GO by using the sputter deposition technique.[87] Sometimes, an annealing treatment is needed to obtain nanospheres. For example, by adjusting the annealing temperature and time, Au nanospheres can be obtained on graphene sheets.[88] Recently, our group also fabricated Ag NPs/graphene composite nanostructures using thermal evaporation.[63] As shown in Fig. 1, sandwiched graphene hybrid nanostructures were fabricated by transferring a monolayer of graphene on top of an Ag film, followed by placing Ag NPs on the graphene surface through thermal evaporation (Fig. 1(a)).[63]

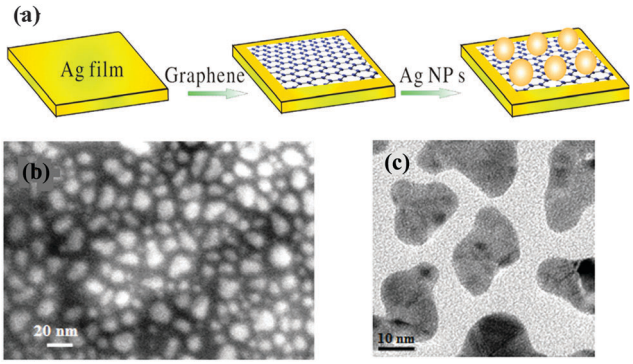

Fig. 1 (a) The schematics of the Ag NP/graphene composite with the structure of Ag film/graphene/Ag NPs, (b) the SEM image of Ag film/graphene/Au NPs, and (c) the TEM image of evaporated Ag NPs on top of graphene. Reproduced with permission.[63] Copyright 2014, Wiley-VCH Verlag GmbH & Co. KGaA, Weinheim.

The tightly distributed Ag NPs with irregular shapes can be clearly observed on the graphene surface (Fig. 1(b)). Because the evaporation rate is very slow, the inter-particle distance is only 5 nm (Fig. 1(c)). If the thermal treatment is applied on the evaporated Ag NPs, *e.g.*, 200 °C for 10 min, the inter-particle distance will increase, and the irregular Ag NPs will evolve into spherical NPs. Furthermore, we also realized graphene-sandwiched Cu NP-film coupling systems with a structure of Cu film/graphene/Cu NPs by thermal evaporation of Cu NPs on top of graphene grown on a Cu film.[89]

In addition, the physical deposition method is also applicable to other 2D materials for constructing metal/2D composites.[90] For instance, Chabal *et al.* obtained the hybrid nanostructures of Au NPs/MoS_2 and Ag NPs/MoS_2 by depositing Au and Ag NPs on as-synthesized MoS_2 flakes using electron-beam evaporation.[90] In general, the physical method is relatively simple and does not require the introduction of additional species for fabricating hybrid nanostructures. However, the size and distribution of metal NPs deposited on 2D materials are difficult to control using physical deposition methods.

2.1.2 Chemical reduction to synthesize the hybrid nanostructures of metal NPs/2D materials. Chemical reduction is the simplest and most efficient method for anchoring metal NPs onto 2D materials with the assistance of various chemical reagents in a solution.[91] From a broad point of view, the hybrid nanostructures of metal NPs/2D materials can usually be described as various metal NPs (Au, Ag, Cu, *etc.*) with uniform or different shapes that are decorated on graphene or other 2D materials.[92–97] Technically, the hybrid nanostructures of metal NPs/graphene are prepared *via* two routes: (1) mixing and reducing either the metal precursors or GO precursors and (2) simultaneously mixing and reducing the metal precursors and GO precursors.[98–100]

For the former, a typical procedure involves pre-synthesizing GO from a modified Hummer's method, which is then mixed with metal precursors, followed by reduction of metal precursors to form metal NPs. For example, Au/graphene can be synthesized by the direct reduction of $HAuCl_4$ in the presence of GO and

reduced graphene oxide (RGO) using ascorbic acid (AA), hydrazine hydrate, and $NaBH_4$.[96,101–103] The final products can be obtained by repeated centrifugation and washing with water or an organic solvent. However, one of the problems is that the prepared hybrids may suffer from aggregation. In addition, the hybrids of metal NPs and 2D materials are not stable or these two components not in tight contact, which inevitably damages the device performance, such as light trapping or electron transfer between the metal NPs and 2D materials, with respect to a particular application. To tackle these problems, linker molecules, such as oleylamine (OLA), octadecylamine (ODA), polydopamine (PDA), and deoxyribonucleic acid (DNA), used to anchor metal NPs on graphene have been reported, with which stable and less-aggregated hybrids can be obtained.[103–112] In addition, bovine serum albumin (BSA) can also be used as a linker molecule for the synthesis of noble Au NPs coated with single-layered GO and RGO nanosheets.[113] As illustrated in Fig. 2(a), as-prepared GO was modified with BSA at pH 8 at room temperature and then mixed with as-synthesized Au NPs.[113] The same steps were carried out to synthesize RGO/Au NPs, in which BSA-modified RGO was obtained by simultaneously reducing GO when decorating it with BSA at 55–90 °C and pH 12. As a result, the hybrid nanostructures of Au NPs/GO (Fig. 2(b)) and Au NPs/RGO with well-distributed Au NPs were obtained (Fig. 2(c)).[113] Using a chemistry-based method, metal NPs can also be decorated on two sides of graphene. Symmetric decoration (the same metal) and asymmetric decoration (different metals) have been reported for the preparation of bi-metal graphene sandwiches. In this way, the loading of the metal NPs has been increased, and the synergistic effect of metal catalysts has been enhanced, which is beneficial for photocatalytic applications.[114] Furthermore, hybrid nanostructures such as Au NPs/graphene with variably shaped Au NPs can be synthesized by the chemical reduction method for obtaining the shape-dependent plasmonic effect.[115,116] For example, Xu *et al.* synthesized Au NPs/GO composites with Au rods, octahedra, branches, and spheres.[117] Berry *et al.* grew dendritic Au nanostructures on GO by reducing $HAuCl_4$ using hydroxylamine.[118] Zhang *et al.* synthesized Au nanowires/GO and tadpole-shaped Au nanowires/GO hybrids using $HAuCl_4$ and 1-amino-9-octadecene.[119] In addition to the metal/GO composites, Au nanowires have been recently obtained on MoS_2 nanosheets through the strong Au–S bonding that confines the oriented growth of Au nanomaterials despite the 8% lattice mismatch between Au and MoS_2.[120] Moreover, through pre-modifying the MoS_2 films using a focused laser beam to obtain active surface areas with unbound sulfur, the Au NPs are selectively and preferentially anchored into the modified regions.[121] Generally, decorating differently shaped metal NPs on 2D materials or placing metal NPs on a particular substrate is a very efficient method for tailoring the plasmonic effect in the hybrid nanostructures, which finally improves the device performance.

For the latter, simultaneously mixing and reducing 2D material precursors and metal precursors can also be used to synthesize hybrids of metal NPs/2D materials. Primo *et al.* synthesized Cu NPs/graphene hybrids through the pyrolysis of alginate or chitosan as the graphene precursor and Cu salts as the Cu precursors with boric acid as the reductant.[122] However, realization of well-dispersed metal NPs decorated on 2D materials remains challenging. Recently, Yan *et al.* proposed and prepared

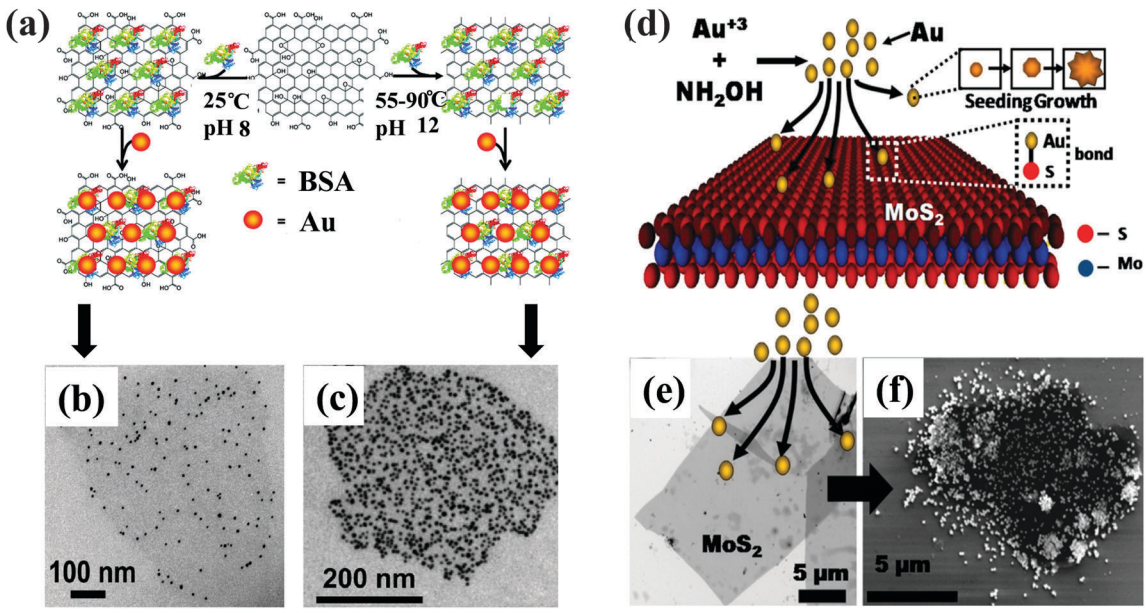

Fig. 2 A chemical reduction method for preparing Au NPs/GO and Au NPs/RGO using BSA as linker molecules between the Au NPs and GO: (a) schematic diagram, (b) TEM image of Au NPs/GO, and (c) TEM image of Au NPs/RGO. Reproduced with permission.[113] Copyright 2010, American Chemical Society. Chemical reduction method for preparing Au NPs/MoS_2: (d) schematic depicting the anchoring of Au nanoparticles on MoS_2 *via* chemical reduction of the mixture of MoS_2 and $HAuCl_4$, (e) TEM image of MoS_2 nanosheets, and (f) FESEM image of the hybrid Au/MoS_2 nanostructures. Reproduced with permission.[124] Copyright 2013, American Chemical Society.

uniform sized metal/GO catalysts with high loading by a three-step protocol, including intercalation, the popping of GO, and reduction steps. The popping of GO is beneficial for separating the nucleation and growth of the metal nanoparticles, generating high-surface-area graphene, and efficiently decomposing the metal salt precursor into small metal NPs anchored strongly on the graphene surface.[123] Chemical methods can also be used to decorate metal NPs on semiconducting MoS_2 and insulating h-BN. Berry *et al.* synthesized Au NPs/MoS_2 sheet composites using hydroxylamine as the reducing agent.[124] As shown in Fig. 2(d), Au^{3+} was reduced to Au NPs with the help of NH_2OH.[124] The freshly generated, small Au NPs were bonded to the S of MoS_2, followed by seeded growth. Eventually, Au NPs with different shapes were incorporated into MoS_2 (Fig. 2(e) and (f)).[124] Using $NaBH_4$, Huang *et al.* obtained Ag/MoS_2 and Ag nanoplates/MoS_2 hybrid nanomaterials.[125] Lin *et al.* synthesized dispersed aqueous Ag NP-decorated h-BN nanosheets by reducing Ag-acetate mixed with an aqueous dispersion of h-BN nanosheets using hydrazine.[126]

In general, the chemical reduction method is a low-cost, solution-processed process and it is therefore commonly used in various plasmon-enhanced applications.[74–81] In addition, the shapes and coverage of metal NPs decorated on the 2D materials can be controlled well by the experimental parameters, which is beneficial for obtaining a strong plasmonic effect and enhanced device performance.[115,116] However, the biggest drawback of the chemical reduction approach is the use of reducing agents, which may introduce undesirable species into the hybrid systems.[103–111]

2.1.3 Photocatalytic reduction to synthesize the hybrid nanostructures of metal NPs/2D materials. Photocatalytic reduction is a green, rapid, and simple approach to synthesize metal NPs/2D materials. Metal ions anchored on 2D material sheets in solution media are reduced *in situ* due to electron transfer or other reduction reactions caused by different light sources.[127,128] The typical process involves mixing metal salts with as-synthesized 2D materials and then subjecting them to illumination by various light sources such as ultraviolet (UV) light,[127,128] lasers,[121,129–131] white light,[132] and others.[133,134] Among these light sources, UV light is the most popular. Fig. 3(a) shows the preparation of hybrid nanostructures of Ag NPs/graphene materials using the UV light reduction method. The graphene placed on a flexible substrate is first treated with oxygen plasma to produce O^- functional groups, and a 2 wt% Ag nitrate solution is then dipped on the surface of graphene. During this process, an electrostatic connection between Ag^+ and the O^- from the oxygen plasma-treated graphene is formed. After the UV light is illuminated on the samples, the Ag^+ can be reduced to Ag NPs. As shown in Fig. 3(b), uniform Ag NPs with small sizes are well decorated on graphene.[135] In addition, both the metal precursor and 2D material precursor can be reduced simultaneously using the photocatalytic reaction. For instance, Ramaprabhu *et al.* synthesized Au and Ag NPs/RGO by simultaneously reducing GO and metal precursors using natural sunlight focused by a convex lens.[136] Moreover, considering that the electrons produced by light during the reduction reaction play a significant role in reducing the metal

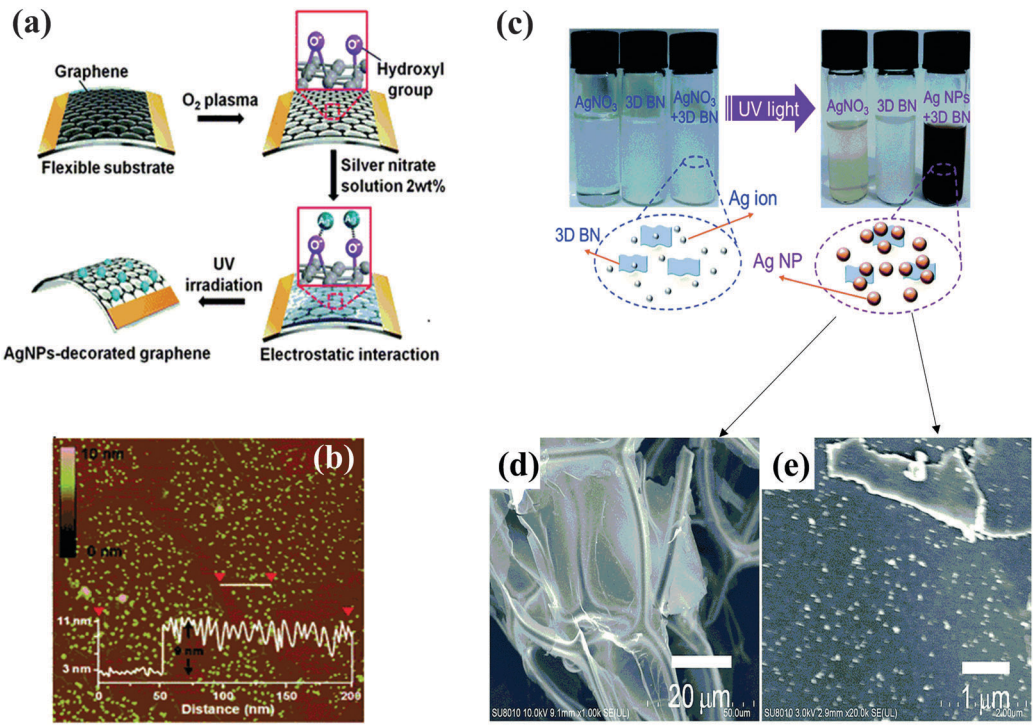

Fig. 3 (a) Schematic diagram of synthesis of Ag NPs/graphene using UV light, and (b) the corresponding AFM image of Ag NPs/graphene with a thickness of 8–11 nm. Reproduced with permission.[135] Copyright 2012, Royal Society of Chemistry. (c) Synthesis schematic diagram of Ag NPs/3D h-BN, and (d) the SEM image and (e) high-magnification SEM image of Ag NPs/3D h-BN. Reproduced with permission.[139] Copyright 2015, Royal Society of Chemistry.

precursors to metal NPs, other semiconductors can be introduced into the synthetic systems to produce more electrons and holes for a more efficient photocatalytic reduction reaction.[137]

Using photocatalytic reduction, metal NPs can also be deposited on other 2D materials. For example, Kalantar-Zadeh *et al.* synthesized Ag nanoplatelets on MoS_2 nanosheets through light-driven growth.[138] Using this method, Zeng *et al.* obtained a hybrid nanostructure of Ag/3D h-BN with Ag NPs uniformly distributed on 3D h-BN.[139] As shown in Fig. 3(c), the pure $AgNO_3$ and 3D h-BN solution did not apparently change color when subjected to UV light, but a significant change in color occurred after the same treatment of a mixed solution of $AgNO_3$ and 3D h-BN, demonstrating the successful synthesis of the Ag/3D BN composite. SEM images showed that Ag NPs are uniformly distributed on 3D h-BN (Fig. 3(d) and (e)).[139] In summary, small and uniform metal NPs can be decorated on 2D materials using photocatalytic reduction, as shown in Fig. 3(b) and (e).[135,139] In the preparation process, parameters such as light intensity, the distance between the light source and the reaction system, and illumination time are important for synthesizing hybrids of various metal NPs/2D materials through the photocatalytic reduction method.[139]

2.1.4 Electrochemical method to synthesize the hybrid nanostructures of metal NPs/2D materials. Due to its simple, fast, environmentally friendly, and green characteristics, the electrochemical reduction method can be used to synthesize metal NPs/2D materials.[140] There are two ways to produce metal NPs/2D materials by electrochemical reduction. One involves immersing an electrode coated with 2D materials in a metal precursor solution and then subjecting it to cyclic voltammetry. The other involves immersing an electrode alone in a solution consisting of metal precursors and 2D materials and then subjecting it to cyclic voltammetry. Using the second method, Tang *et al.* synthesized hybrid nanostructures of Au NPs/graphene by immersing an electrode in a solution consisting of homogeneously dispersed GO and $HAuCl_4$.[141] SEM images showed that the layered composites composed of alternating layers of metal NPs and graphene sheets were obtained (Fig. 4(a) and (b)).[141] Parameters such as the scan rate, cyclic potential, and concentration of 2D materials (such as GO) must be precisely controlled to synthesize high-quality hybrid nanostructures of metal NPs/2D materials.

Similar to the chemical reduction, linker molecules can be used as an assisting medium for better electrodeposition of metal NPs onto 2D materials.[142] Nossol *et al.* fabricated the hybrid nanostructures of Ag NPs/RGO and Cu NPs/RGO using a one-step electrodeposition method with the assistance of 7,7,8,8-tetracyanoquinodimethane (TCNQ).[142] Other reagents are also employed in electrochemical reduction. For instance, hybrid nanostructures of Cu NPs/graphene were synthesized using the electrochemical reduction method by adding two assisting media, polyacrylic acid 5000 (PAA5000) and cetyltrimethylammonium bromide (CTAB), to efficiently prevent the agglomeration of graphene sheets.[1,83,143] In summary, the desired hybrid nanostructures of metal NPs/2D materials with different shapes of metal NPs and different 2D materials can be obtained

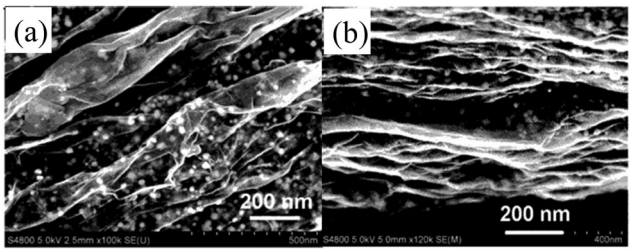

Fig. 4 (a) The top-view SEM image and (b) cross-sectional SEM image of the hybrid nanostructures of Au NPs/graphene synthesized by direct electrodeposition. Reproduced with permission.[141] Copyright 2011, Wiley-VCH Verlag GmbH & Co. KGaA, Weinheim.

using electrochemical deposition.[128,144] The advantage of the electrochemical method is that the 3D layered hybrid nanostructures with alternating metal NPs and 2D materials tend to be fabricated.[141] As a result, a large surface area and well-organized metal NPs and 2D materials are achieved, which are very beneficial for the plasmon-enhanced catalytic reaction.[141]

2.1.5 Solvothermal method to synthesize the hybrid nanostructures of metal NPs/2D materials. The solvothermal method is a simple and economical way to synthesize metal NP/2D material nanocomposites.[145,146] A mixture of metal precursors, chemical reagents, and pre-synthesized 2D materials are poured into a Teflon autoclave and then maintained at an established temperature for a certain amount of time. Metal NPs were reduced and deposited on the 2D material sheets during the reaction.[145,146] For example, Li *et al.* synthesized Cu NP/MoS_2 hybrids by placing 1-hexadecylamine (HDA), glucose, copper chloride, and as-synthesized MoS_2 in a Teflon-lined stainless steel autoclave and heating it in an oil bath at 120 °C for 1 h.[147] Moreover, a 3D hybrid structure of metal NPs/2D materials can also be synthesized by the hydrothermal method. Wang *et al.* produced 3D hybrid structures of Au NPs/graphene by placing a mixture of $HAuCl_4$, a GO suspension, and glucose in a Teflon-lined stainless-steel autoclave and heating it at 120 °C for 20 h.[148] It should be noted that one of the common disadvantages of this method is that the final product may suffer from a certain degree of aggregation.

2.1.6 Wave-assisted reduction method to synthesize the hybrid nanostructures of metal NPs/2D materials. Wave-assisted reduction is a rapid, green, and low-energy-consuming method to synthesize the hybrid nanostructures of metal NPs/2D materials. In this methodology, waves such as microwaves,[149–151] ultrasound,[152–155] and gamma rays,[156] can be employed. The typical preparation procedure involves mixing the metal precursors, the reducing agent, and as-synthesized 2D materials and the metal precursors are then reduced to metal NPs upon irradiation with the waves. The energy provided by the waves influences the metal ions or metal particles in high dielectric solvents such as water and reduces the metal ions to metal NPs with the assistance of a reducing agent. Because of uniform heating, well-distributed metal NPs deposited on 2D materials can be obtained. Chen *et al.* synthesized the hybrid nanostructures of Cu NPs/graphene by mixing $Cu(NO_3)_2{\cdot}3H_2O$ and pre-synthesized GO in ethylene glycol.[157] With the assistance of

microwaves (400 W, 3 min), ethylene glycol reduced Cu^{2+} to Cu NPs and simultaneously modified GO slightly. Hence, the hybrid nanostructures of Cu NPs/GO were obtained.[157] Adjusting the content of $Cu(NO_3)_2{\cdot}3H_2O$, such as 5 wt% and 15 wt%, resulted in the hybrid nanostructures of Cu NPs/GO with different Cu coverages.[157] In addition, the exposure intensity and time also strongly affect the metal NP coverage on the 2D material sheets.[124]

Metal NPs with different shapes can also be directly decorated on 2D materials without adding a linker agent with the assistance of waves, which is different from the chemical reduction and electrochemical methods.[158] Wang *et al.* reported the hybrid nanostructures of Ag NPs/graphene with different shapes.[158] As shown in Fig. 5(a), expandable graphite was heated to 950 °C for 20 s under Ar gas to obtain expanded graphite, which was subjected to sonication in NMP.[158] The resulting dispersion was centrifuged, and the well-dispersed graphene solution was obtained by collecting the top half of centrifuge tube's contents. The pre-synthesized Ag NPs (dispersed in ethanol) with different morphologies were mixed with the contents resulting from centrifugation. After sonication of the mixture, the resultant suspension was held steady for several hours, and the hybrid nanostructures of Ag nanospheres/graphene (Fig. 5(b)), Ag nanocubes/graphene (Fig. 5(c)), and Ag nanoplates/graphene (Fig. 5(d)) were formed through spontaneous adsorption of Ag NPs onto the pristine graphene surface.[158]

2.2 Preparation of hybrid nanostructures of metal nanostructures/2D materials

The hybrid nanostructures of metal nanostructures/2D materials are used in plasmon-enhanced optical signals, including SERS, plasmon-enhanced photoluminescence (PL),[159,160] and plasmon-enhanced photodetection, because of their fabrication technique and 2D structural features.[161–163] Thus, there are some functional requirements for the design and manufacture of these hybrid nanostructures in addition to some specific demands depending on a particular application. First, the metal nanostructures should have a strong plasmonic effect, and the 2D material film should be of high quality. Second, avoiding damage to the two components and ensuring tight contact between the two components are critical during the integration of metal nanostructures and 2D materials. Compared to the preparation of hybrid nanostructures of metal NPs/2D materials, which can be obtained by various methods, the fabrication of hybrid nanostructures of metal nanostructures/2D materials primarily uses a physical method. Three steps are needed: fabrication of the metal nanostructures, preparation of the 2D materials, and integration of the metal nanostructures and 2D materials.

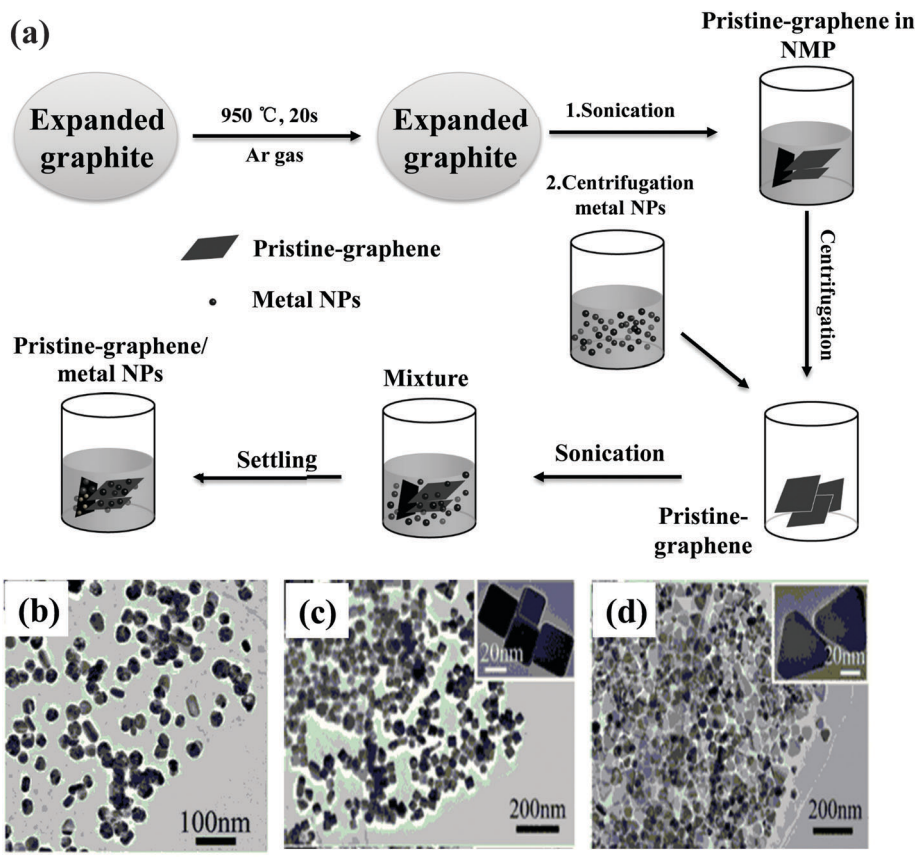

Fig. 5 (a) Schematic illustration of the synthesis of the hybrid nanostructures of metal NPs/graphene, and the corresponding TEM images of (b) Ag nanospheres/graphene, (c) Ag nanocubes/graphene, and (d) Ag nanoplates/graphene hybrids. Reproduced with permission.[158] Copyright 2013, Wiley-VCH Verlag GmbH & Co. KGaA, Weinheim.

Thus, obtaining the two single components is a prerequisite for these hybrid nanostructures. After preparation of the two individual components, realizing the integration of the metal component and the 2D component becomes the crucial step.

In recent years, simple hybrid nanostructures with a single metal component and a single 2D component have been reported by placing the 2D materials on top of the pre-fabricated metal nanostructures[164–168] or by directly fabricating the metal nanostructure on top of the 2D materials.[161–163,169–174] The advantage of the former method is that it is easier to obtain the hybrid nanostructures and very suitable for studying the plasmon-enhanced optical signals and fabricated tunable plasmonic resonance. As shown in Fig. 6(a), PMMA can be first spin-coated on top of pre-prepared graphene grown on the Cu foil, and the Cu foil is then etched away. Then, the graphene is transferred to cover the Au voids, which have been fabricated by nanosphere lithography (NSL) in advance.[167] After the PMMA covering the graphene has been dissolved, the hybrid nanostructures of metal voids/graphene can be obtained. Following a similar procedure, a monolayer graphene covering an annular gap array of Au with a gap size of 2 nm as a hybrid device for terahertz (THz) transmission was fabricated (Fig. 6(b)).[165] In addition to the hybrid nanostructures of metal nanostructures/graphene, hybrids of metal nanostructures with other 2D materials have also been reported, such as single-layered MoS_2 coated with Au nanorod arrays fabricated by combining electron beam lithography (EBL), chemical vapor deposition (CVD), and a transfer technique.[175] The integration process and quality of 2D materials have substantial effects on the device performance and application. Two key points should be considered. (1) The roughness of the metal nanostructures should be controlled to reduce wrinkles or other damage to the 2D materials. (2) The surface wetting properties of the metal nanostructures and 2D materials are also significant issues that affect the integration of these materials. For example, although the typical metal films and graphene are hydrophobic, it is hard to scoop the graphene floating on the water using metal nanostructures. Thus, surface decoration is necessary to modify hydrophobicity.

In the latter method, the metal nanostructures are fabricated on the 2D materials. As shown in Fig. 6(c), a nanoarray of Au nanorods made using the focused ion beam (FIB) technique is placed on top of graphene.[176] The pre-obtained graphene can be realized by transferring the CVD-grown graphene from other substrates. Through a similar method, the hybrid nanostructures of metal nanostructures/MoS_2 materials have also been reported, such as hybrid nanostructures of Ag bowtie nanoantenna arrays

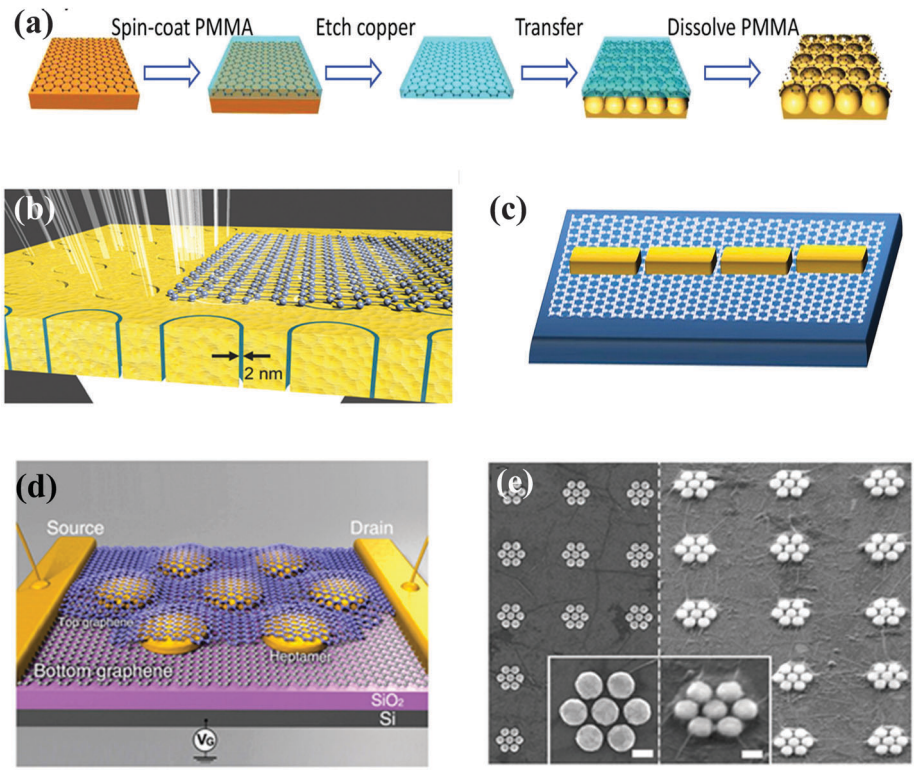

Fig. 6 (a) Schematic illustration of the metal voids/graphene hybrid nanostructures by transferring graphene to the top of the metal voids. Reproduced with permission.[167] Copyright 2013, American Chemical Society. (b) Schematic diagram of THz transmission coupled to monolayer graphene onto an annular gap array with a gap size of 2 nm. Reproduced with permission.[165] Copyright 2015, Wiley-VCH Verlag GmbH & Co. KGaA, Weinheim. (c) Schematic of an end-to-end coupled antenna array, Reproduced with permission.[176] Copyright 2013, American Chemical Society. (d) Schematic illustration of a single Au heptamer sandwiched between two monolayer graphene sheets. V_g is the gate voltage used to dope electrostatically the graphene, and (e) the corresponding SEM image of the as-fabricated device before (left) and after (right) deposition of the second graphene layer. Reproduced with permission.[178] Copyright 2013, American Chemical Society. The scale bar of the inset of (e) is 100 nm.

sitting on top of a chemically grown MoS_2 monolayer[160] and Ag nanodisk arrays placed on top of a MoS_2 monolayer.[177] From the viewpoint of fabrication, this method is also very easy, and this type of architecture is very compatible for plasmon-enhanced optoelectronics and electrically tunable plasmonic resonance applications. Compared to the former method, the latter avoids the transfer of 2D materials to metal nanostructures and reduces the formation of wrinkles in 2D materials. The second method involves the fabrication of metal nanostructures directly on top of 2D materials; efficiently realizing the metal nanostructures and avoiding damage to 2D materials are key technological issues.

In addition to simple hybrid nanostructures composed of single parts of metal nanostructures and single parts of 2D materials, relatively complicated hybrid nanostructures have also been reported.[179–181] Recently, Halas *et al.* designed the Au heptamers sandwiched between monolayer graphene sheets.[178] As shown in Fig. 6(d), the first graphene monolayer was placed on top of the SiO_2 substrate; then, Au heptamer nanostructures were fabricated on the substrate. Afterward, a second graphene monolayer was transferred onto the top of the Au nanostructures. This complicated hybrid nanostructure can be designed for optoelectronics. Fig. 6(e) shows the corresponding SEM images of the as-fabricated device, the Au nanoarrays of heptamers are sitting on the first graphene monolayer (left). After the second graphene monolayer is placed on top of the Au heptamers, graphene wrinkles can be observed around the edge of the Au heptamers (Fig. 6(e)).[178] In addition, other complicated hybrid nanostructures have been designed and fabricated. To achieve an ultrahigh field enhancement and photoresponse, Paria *et al.* reported arrays of plasmonic dimers separated by atom-thick graphene.[182] They first made Ag NPs on top of silica spheres using oblique angle deposition. A single-layered graphene was transferred on top of the Ag NPs using the standard graphene transfer protocols, and the second layer of Ag NPs arrays was deposited on graphene using the same oblique angle deposition. After an annealing treatment, the Ag NP dimers with graphene as the nanospacer were obtained.[182] Because the distance is tiny (*i.e.*, 0.34 nm), very strong plasmonic coupling can be achieved, which can be used for high-performance photodetectors. Hybrid graphene/h-BN/Ag nanodisc nanoarrays have also been fabricated to study plasmon-induced optical anisotropy. h-BN introduced as a sub-nanospacer layer functioned as an effective barrier to electron transfer when the light–matter interaction between graphene and metal nanostructures was studied.[183] Compared to the simple hybrid nanostructures, relatively complicated hybrid nanostructures will possibly produce a stronger light–matter interaction or possess additional functions for various applications. The design of other complex hybrid nanostructures with additional or specific features will become increasingly important and interesting.

2.3 Summary of preparation of hybrid nanostructures of metal nanomaterials/2D materials

For the preparation of hybrid nanostructures of metal NPs/2D materials, six methods have been discussed and compared, including physical deposition, chemical reduction, photocatalytic reduction, an electrochemical method, a solvothermal method, and a wave-assisted reduction method. The features, disadvantages, and applications have been summarized in Table 1. The physical deposition of metal NPs directly on the 2D materials does not require any chemical agents (*i.e.*, reduction agents) and avoids the introduction of any additional residuals in the hybrid nanostructures. However, the disadvantage of this method is that the size and distribution of the metal NPs deposited on the 2D materials are difficult to control.[63] Compared to the physical deposition of metal NPs on 2D materials, the other five methods are solution-processed, which, to some extent, reduces the fabrication cost. Fabricating hybrid nanostructures with high specific surface areas is another advantage of these solution-processed methods.[74–81] The possible drawback of the solution-processed method is that some additional residuals or impurities will be

Table 1 Comparisons the six methods discussed in the preparation of hybrid nanostructures of metal NPs/2D materials

Methods	Features	Disadvantages	Applications
Physical deposition	Fast, efficient, without addition species	Size and distribution of metal NPs are not easy to control	SERS, PL, PD
Chemical reduction	Simple, facile, efficient, large surface area	Assistant agent needed, impurities introduced	SERS, PL, photocatalytic reaction, interlayer of solar cells
Photocatalytic reduction	Green, facile, large surface area, metal NPs with small size well distributing on the 2D materials	Light intensity and illumination time have significant influences on the synthesis of the hybrids	SERS, PL, photocatalytic reaction, interlayer of solar cells
Electrochemical method	Simple, green, large surface area, layered hybrid nanostructures with alternating metal NPs and 2D materials	Assistant agent needed	SERS, PL, photocatalytic reaction, interlayer of solar cells
Solvothermal method	Simple, cost-effective, facile, large surface area	Hybrids suffer from a certain degree of aggregation	SERS, PL, photocatalytic reaction, interlayer of solar cells
Wave-assisted reduction	Rapid, green, facile, low-consuming energy, large surface area	Synthesis of hybrids is sensitive to wave intensity and radiation time	SERS, PL, photocatalytic reaction, interlayer of solar cells

introduced during the preparation process.[103–111] In addition, solution-processed 2D materials always have some defects that will affect the electronic properties of hybrid nanostructures. Among these methods, chemical reduction is the primary method. By introducing another driving force as an assisting agent into the chemical reduction system, new and advanced methods have been developed, *e.g.*, introducing light for photocatalytic reduction, introducing electricity for electrochemical processes, introducing high pressure and high temperature for solvothermal methods, and introducing waves for the wave-assisted reduction technique. For chemical reduction and electrochemical reduction, additional linkers added into the reduction system are beneficial to avoid the aggregation of the hybrid nanostructures and to keep the metal NPs tightly anchored on the 2D materials.[103–111,135,142] When these solution-processed methods are applied, various structural features are observed. For example, subtle metal NPs are always synthesized and well decorated on the 2D materials when using the photocatalytic reduction method, if the experimental parameters are well controlled.[174] The layered hybrid nanostructures with alternating metal NPs and 2D materials are inclined to be fabricated when electrochemical deposition is applied.[141]

For the preparation of hybrid nanostructures of metal nanostructures/2D materials, two crucial points should be emphasized: realizing unique metal nanostructures with specific requirements using lithography methods such as EBL, FIB, and NSL[175] and successfully integrating the metal nanostructures with 2D materials without damage to the physical and chemical properties of the two components.

We should mention again the particular requirements for the preparation of hybrid nanostructures of metal/2D materials, which is dependent on the plasmon-enhanced application. For example, the large specific surface area is beneficial to the plasmon-enhanced photocatalytic reaction. To achieve this goal, all of the solution-processed methods are possible. Optical sensitivity and selectivity are necessary for photodetectors and should be obtained using physical deposition to design precisely the hybrid nanostructures of metal nanostructures/2D materials.[178] Restrained electron transfer for plasmon-enhanced PL can be realized by introducing an additional dielectric layer between the metal nanomaterials and 2D materials.[53,70,71]

However, there are currently several difficulties in the fabrication of hybrid nanostructures. In the hybrid nanostructures of metal nanomaterials/2D materials, the metal nanomaterials are not tightly anchored on the 2D materials. The poor contact between the metal nanomaterials and 2D materials will greatly block the charge transfer. In addition, the morphology and structures of the metal nanomaterials and the film quality of the 2D materials are always destroyed during the integration of the two components, which will ultimately have an adverse impact on device performance. To tackle these problems, a fundamental understanding of the physical and chemical properties of the two components is necessary. Improving the existing preparation techniques and developing new fabrication methods are expected.

3. Optical properties of the hybrid nanostructures of plasmonic metal/2D materials

To discuss the optical properties of the hybrid nanostructures of metal/2D materials, we should understand the fundamental properties of the individual noble metal component and the 2D materials, respectively. Considering that each component has already been widely reported and reviewed recently,[11,25,36,43,48,58,59,70,73,184–188] we will briefly introduce the plasmonic effects derived from metal NPs and nanostructures and the various properties of 2D materials and then mainly review the optical properties of the hybrid nanostructures in this section.

3.1 Plasmonic effects from metal NPs and metal nanostructures

Metal NPs (*e.g.*, discrete nanospheres, nanorods, nanocubes, and nanoprisms) and nanostructures (*e.g.*, arrays of nanopatterns, metal slits) that reveal strong light–matter interactions between the electromagnetic field and free electrons make them useful materials for achieving plasmonic effects.[59] The principle of the metal plasmonic effect can be understood by comparison with a simple harmonic oscillator. Metals can be regarded as heavy, positive nuclei surrounded by a cloud of free electrons. When an oscillating optical electric field is incident on the metal acting as the applied force, the electrons surrounding the metal are driven and move along the field direction. At the same time, the Coulombic attraction between the delocalized electron cloud and the nuclei acts as the restoring force, which is opposite to the displacement of electrons. At a certain resonant frequency, the oscillations caused by the Coulombic attraction become in phase with the oscillating electric field. As a result, the incident light is absorbed by the metal; effective energy is stored in the metal; and a very strong electric field is produced around the metal. Typically, plasmonic effects can be divided into two types: the localized surface plasmon (LSP) effect and the surface plasmon polariton (SPP) effect.[189,190] Materials that can support the plasmonic effect in the visible and near-infrared regions are required to have free charge-carrier concentrations of up to 10^{21} cm^{-3}.[191,192] Metals, such as Au, Ag, and Cu with enough free electrons, are suitable materials for supporting the plasmonic effect in the visible and near-infrared regions.[70]

The LSP effect is mainly attributed to the confined electrons on the surface of the metal NPs.[59] The modes of non-propagating plasmons primarily arise from interactions between the incident light and the sub-wavelength metal NPs.[185,193] The underlying physics is that the curved protuberance from the NPs will generate an efficient restoring force on the driven electrons, which will induce a resonance and finally amplify the electromagnetic field in the near-field region outside the metal NPs (see Fig. 7(a)).[193] The Mie theory analytically solving Maxwell's equations can be utilized for characterizing the excitation of resonance modes. The extinction (σ_{ext}),

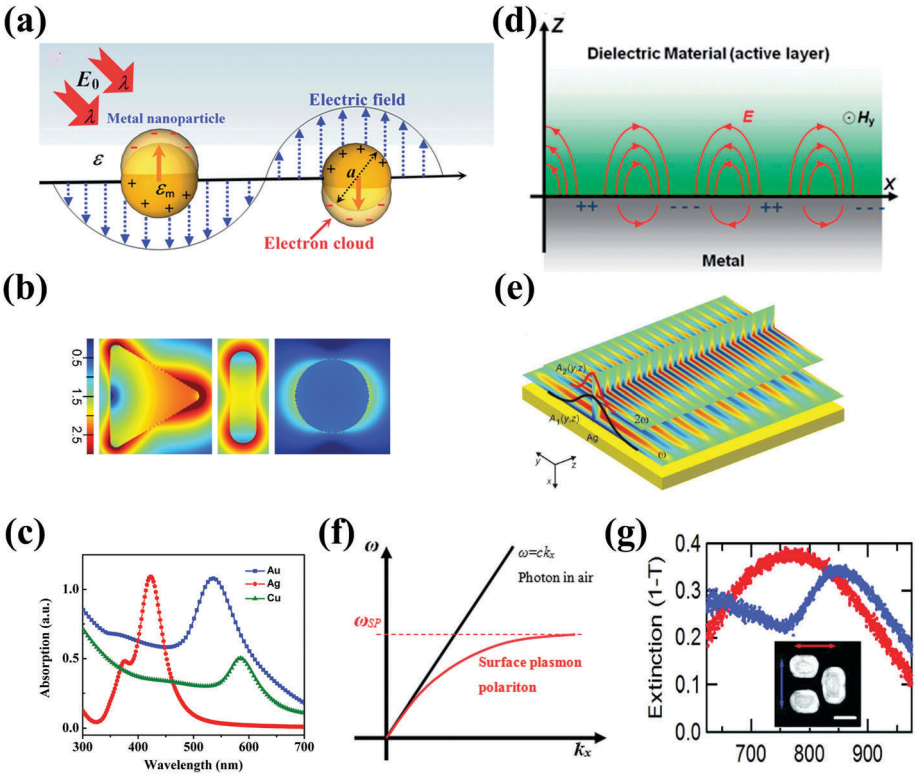

Fig. 7 (a) Illustration of the LPR effect on nanospheres. Reproduced with permission.[193] Copyright 2014, Royal Society of Chemistry. (b) The electric field intensity enhancement of differently shaped Au nanocrystals, including from left to right the nanoprism with an edge length of 87 nm and a thickness of 10 nm, a nanorod with a length of 103 nm and a diameter of 30 nm, and a nanosphere with a diameter of 50 nm. Reproduced with permission.[70] Copyright 2014, Wiley-VCH Verlag GmbH & Co. KGaA, Weinheim. (c) The absorption spectra of different metal components, including Au nanospheres, Ag nanospheres, and Cu nanospheres with a diameter of 50 nm. (d) Illustration of the SPP effect between the metal and dielectric layer. Reproduced with permission.[193] Copyright 2014, Royal Society of Chemistry. (e) The propagating SPP near-field profile of grating with soliton geometry, Reproduced with permission.[199] Copyright 2015, IOP Publishing. (f) Dispersion curve of a typical SPP mode, where a momentum mismatch exists between the light and the SPP. Reproduced with permission.[193] Copyright 2014, Royal Society of Chemistry. (g) The extinction spectra of the dolmen nanoantenna shown in the inset of the panel. The structure (200 nm side) is illuminated by light with different polarization (red and blue arrows). Reproduced with permission.[203] Copyright 2009, American Chemical Society.

scattering (σ_{scat}) and absorption cross section (σ_{abs}) of metal nanospheres are given as follows:[194]

$$\sigma_{ext} = \frac{2\pi}{k^2}\sum_{l=1}^{\infty}(2l+1)\mathrm{Re}\{a_l + b_l\} \quad (1)$$

$$\sigma_{scat} = \frac{2\pi}{k^2}\sum_{l=1}^{\infty}(2l+1)\left(|a_l|^2 + |b_l|^2\right) \quad (2)$$

$$\sigma_{abs} = \sigma_{ext} - \sigma_{scat} \quad (3)$$

where

$$a_l = \frac{m\psi_l(mx)\psi_l'(x) - \psi_l(x)\psi_l'(mx)}{m\psi_l(mx)\xi_l'(x) - \xi_l(x)\psi_l'(mx)}$$

$$b_l = \frac{\psi_l(mx)\psi_l'(x) - m\psi_l(x)\psi_l'(mx)}{\psi_l(mx)\xi_l'(x) - m\xi_l(x)\psi_l'(mx)}$$

in which ψ_n and ξ_n are the Riccati–Bessel cylindrical functions, k is the wavenumber of the incident light in the dielectric medium, the size parameter is $x = kR$, R is the radius of metal nanospheres and $m = n_m/n_d$ is the relative refractive index. Here, $n_m = \sqrt{\varepsilon_m}$, $n_d = \sqrt{\varepsilon_d}$, ε_m and ε_d are the permittivities of metal nanospheres and the surrounding dielectric medium, respectively.

When the nanoparticle size is much smaller than the incident wavelength, the metal nanoparticle can be considered as a dipole and the electrostatic approximation is an efficient tool for characterizing and understanding the resonance of the metal nanoparticle. The polarizability (α) of a metal nanosphere can be expressed as follows:

$$\alpha = 4\pi R^3\frac{\varepsilon_m - \varepsilon_d}{\varepsilon_m + 2\varepsilon_d} \quad (4)$$

According to eqn (4), the near field reaches a maximum when the real part of permittivity $\mathrm{Re}\{\varepsilon_m\}$ is equal to $-2\varepsilon_d$. The wavelength in this situation is called the localized surface plasmon resonance (LSPR) wavelength. When the excited light is at the LSPR wavelength, the dipolar resonance can be excited.

The expressions of absorption, scattering and extinction cross section of small metal nanospheres are given as follows:[200]

$$\sigma_{abs} = \frac{k^4}{6\pi}|\alpha|^2 = \frac{8\pi}{3}k^4R^6\left|\frac{\varepsilon_m - \varepsilon_d}{\varepsilon_m + 2\varepsilon_d}\right|^2 \quad (5)$$

$$\sigma_{scat} = k\mathrm{Im}\{\alpha\} = 4\pi kR^3\mathrm{Im}\left\{\frac{\varepsilon_m - \varepsilon_d}{\varepsilon_m + 2\varepsilon_d}\right\} \quad (6)$$

$$\sigma_{ext} = \sigma_{abs} + \sigma_{scat} \quad (7)$$

The resonant properties of the LSP effect can be efficiently modified by changing the shape, material composition, and size of the metal NPs.[44,45,54] Regarding the shape, a high field enhancement occurs around the curvature of metal NPs. As shown in Fig. 7(b), the Au NPs with different shapes show different field intensity increases. Compared to Au nanospheres, nanoprisms and nanorods show stronger field enhancements around the tip regions. In general, the maximum field enhancement for plasmonic metal NPs reported from theoretical calculation ranges from *ca.* 50 to *ca.* 10 000, strongly dependent on the metal shapes.[70] In addition, the shape of plasmonic metal NPs also affects the plasmonic resonance. By changing the geometry, the LSP peak can be tailored from the violet to the visible region and the infrared region.[195] Recently, a novel black plasmonic colloidosome assembled from Au nanospheres has been reported, which showed broadband absorption.[196] Regarding the metal component, the permittivity of materials has direct effects on the plasmonic resonance. Typical plasmonic metal components including Au, Ag, and Cu have different permittivities. As a result, the well-dispersed Au NPs, Ag NPs, and Cu NPs with a diameter of 50 nm show an LSP peak at 512 nm, 400 nm, and 576 nm, respectively (Fig. 7(c)). Regarding the size of plasmonic metal NPs, in general, smaller metal nanospheres (*i.e.*, 20 nm Au) are primary absorbers due to a strong near-field enhancement, whereas relatively large metal nanospheres (*i.e.*, 80 nm Au) have a more noticeable scattering due to far-field enhancement.[53] In addition, the environment surrounding the metal component also has a strong effect on the plasmonic resonance. A change in the dielectric constant will lead to a shift in plasmonic resonance. The large dielectric constant of a medium around the plasmonic metal results in a more obvious red-shift of plasmonic resonance. Based on this principle, the plasmonic metal can be used as an ultrasensitive sensor for detecting environmental pollutants and bio-molecules.[197]

Another type of plasmonic effect is the SPP effect, which typically propagates evanescent waves bound around interfaces between metal nanostructures and dielectrics due to the coupling of the electromagnetic fields and the oscillation of the electrons in the metal nanostructures (Fig. 7(d)).[198] Based on Maxwell's equations, the dispersion relationship can be described by the following equation:[198]

$$K_{sp} = \frac{w}{c}\sqrt{\frac{\varepsilon_d\varepsilon_m}{\varepsilon_d + \varepsilon_m}} \quad (8)$$

where K_{sp} is the wave vector; ε_d and ε_m are the relative permittivities of the dielectric and metal materials, respectively; and w and c are the angular frequency and the speed of light in a vacuum, respectively. Fig. 7(f) shows the dispersion curve of a typical SPP. The excitation of surface plasmon polaritons can be explored by the dispersion curve combined with the phase-matching condition. In general, the dispersion line of SPP is on the right side of the light line which means the wave vector K_{sp} is small than the k_x. Thus, the incident light cannot easily excite the surface plasmon polaritons. The Kretschmann method and Otto configuration are two typical methods to excite the surface plasmon polaritons through utilizing a prism to provide an additional wave vector and achieve the phase-matching condition.[200,201] Meanwhile, the periodic arrangement of the metal-dielectric configuration (*i.e.*, grating) can also provide an additional wave number $\Delta k = 2\pi/P$. The momentum matching condition of the grating structure is

$$k_x = k_0\sin\theta + l\Delta k = \frac{\omega}{c}\sqrt{\frac{\varepsilon_d\varepsilon_m}{\varepsilon_d + \varepsilon_m}} = K_{sp}, \quad l = 0, \pm1, \pm2, \ldots \quad (9)$$

Therefore, the overcome of the phase mismatch ultimately generates surface plasmon modes, leading to a highly localized electromagnetic field. Under the excited light, the metal nanostructures, such as Au gratings, display a strong plasmonic near-field enhancement along the metal surface, as shown in Fig. 7(e).[199] Over the past five years, increasing numbers of novel metal nanostructures with various configurations have been designed and fabricated, and unique plasmonic properties have been intensively studied, including in-plan Fresnel zone plates (FZPs) for SPP propagation, focusing, and coupling; symmetry broken plasmonic nanocorals for nanoscale enhancement focusing and phase controlling; plasmonic Fano resonance with a single sliced metal nanodisc, second harmonic generation as a typical nonlinear plasmonics, *etc.*[52,202] Specific optical property functions of metal nanostructures can be realized by designing a unique configuration, such as broadband absorption, polarization independence, or infrared sensitivity. Recently, a dolmen-shaped nanostructure composed of three Au nanorods with similar dimensions (100–200 nm) was designed. As shown in Fig. 7(g), the novel nanostructure supports a Fano resonance in the near-infrared region.[186,203] When the nanostructure was irradiated with light polarized along the red arrow, the extinction spectrum in red showed a broad peak at approximately 780 nm. After the incident polarization rotates along the blue arrow's direction, a narrow dip at the same wavelength is observed. The produced asymmetric spectra reflect the formation of a Fano resonance in the system.[203] Periodic asymmetric nanostructures made of aluminum have also been reported recently, which show a high symmetry-broken color rendering effect.[204] A chiral plasmonic system has been studied for its significant chiroptical responses.[205] Because plasmonic metal nanostructures enable an efficient transfer of electromagnetic energy from the near- to far-field and *vice versa*, they are widely considered as nano-antennae for extensive applications, such as photodetectors, optical sensors, and emitters.[52,206,224]

To conclude, of the optical properties of plasmonic nanomaterials including metal NPs and metal nanostructures, the first important one is that plasmonic nanomaterials exhibit very strong light–matter interactions under resonant excitation.[207] Very significant absorption and scattering at the LSP and SPP wavelengths can be achieved. The absorption-induced scattering and surface plasmon out-coupling have also been reported, which make the optoelectronic application of metasurfaces practical.[208] Second, both absorption and scattering cross-sections can be tailored by changing the size, shape, metal composition, and environment of the metal NPs and metal nanostructures over a broad wavelength region from violet and visible to infrared wavelengths.[70,209] Another important property of plasmonic NPs and nanostructures is electric field localization, which enables plasmonic resonance to break the diffraction limit and trap light in a nanoscale region.[54,210–213]

3.2 Properties of 2D materials

As discussed above, the unique structures and properties of 2D materials enable them to be excellent building blocks not only for designing hybrid nanostructures but also in promising photonic and electric devices. To better understand and create the hybrid nanostructures of metals/2D materials, various properties of 2D materials, including the mobility, conductivity, absorbance, mechanical flexibility, and specific surface area, will be comprehensively discussed in this section.[3,271]

Graphene is a zero-bandgap semiconductor with the highest carrier mobility at room temperature ($\sim$40 000 cm^2 V^{-1} s^{-1}) reported to date.[214] The schematic structure and electric band structure of graphene are shown in Fig. 8.[272] The sheet resistance R_s of a graphene monolayer is $\sim$62.4 Ω sq^{-1}, enabling it to hold a potential in high-frequency electronic devices and highly transparent conductive electrodes.[215] Because of its emergent electronic structure with massless Dirac fermions, ballistic carrier transport was achieved in suspended graphene.[216] Regarding its absorbance, the optical conductivity is mainly contributed by interband carrier transitions in the visible range. For the cases of intrinsic or lightly doped graphene, the absorbance is constant ($\sim$2.3%) in the visible range.[3,6] In contrast, the optical conductivity of graphene in the THz range is primarily contributed by intraband scattering.[3,6] Compared to metal nanomaterials showing a plasmonic effect in the near-infrared and visible regions, graphene exhibits a tunable plasmonic effect due to its ability for low losses and high confinement in the THz range and the mid-infrared range.[217–223] Through chemical and electrical doping, the permittivity (*i.e.*, charge density and conductivity) and plasmonic characteristics (*i.e.*, confinement and wavenumber) of graphene can be tuned.[224] Therefore, graphene can be potentially used for optical modulators. A possible coupling between metal nanomaterials and graphene can also be achieved if the plasmonic resonance of their wavelengths is tuned to overlap each other.[225] Furthermore, as one of the strongest materials, the 3D Young's modulus and the intrinsic breaking strength of graphene can reach up to $\sim$1.0 TPa and $\sim$130 GPa, respectively, making it a promising material for flexible optical and electronic devices. Graphene also has a large surface area. As recently reported, graphene nanomaterials with a surface area of 2150 m^2 g^{-1} were synthesized using a chemical exfoliated method, indicating that graphene has prospective applications in photocatalytic reactions, sensors, and solar cells.

GO is a type of intermediate material between graphite and graphene.[226] The structure and properties of GO are different from that of graphene because oxygen bonding forms sp^3 hybridization on graphene.[226] The introduction of oxygen atoms, which have a larger electronegativity than carbon atoms, causes GO to exhibit distinct p-type doping properties.[227] The bandgap of GO is strongly affected by the oxidation level.[227] In addition, the GO bandgap can also be tuned by doping or functionalization.[228,229] Furthermore, GO synthesized by solution-processed methods exhibits one of the largest specific surface areas among the 2D materials. Both the structural features and related chemical and physical properties make GO an ideal photocatalyst for water splitting, optical sensing for biotechnology,[230–234] and buffer layers for photovoltaics.[235,236]

Another class of 2D materials, semiconducting TMD monolayers, have a direct band gap (Fig. 8).[272] As two typical examples of TMDs, the MoS_2 multilayer is an n-type semiconductor with a reported mobility of 980 cm^2 V^{-1} s^{-1}, and WSe_2 exhibits a p-type semiconductor property with a recorded mobility of 500 cm^2 V^{-1} s^{-1}. A single-layer MoS_2 field effect transistor (FET) shows a mobility of 10–30 cm^2 V^{-1} s^{-1} and an on/off ratio exceeding 10^6.[237,238] Compared to that of graphene, the conductivity of 2D TMDs is very low. A MoS_2 monolayer has an absorbance of 5–10%, which is relatively higher than that of graphene, Si, and GaAs of the same thickness. Therefore, 2D TMDs can potentially be used for photoelectronic devices and photocatalytic reactions. In addition, the MoS_2 monolayer has a direct band gap of 1.8 eV. Specifically, MoS_2 can produce a high PL, which enables MoS_2 as an emitter and optical imager in biotechnology.[239,240] Moreover, 2D TMDs also have relatively large surface areas. For instance, a recently reported MoS_2 showed a specific surface area of 210 m^2 g^{-1}. In summary, based on the properties of 2D TMDs, including a moderate mobility, good absorbance, low conductivity, and large surface area, MoS_2 can be applied in sensing,[241–243] photovoltaics,[244–246] optical catalytic reactions,[247,248] and photodetector applications.[249–257]

Recently, much attention has been focused on the optical properties of h-BN insulators.[17,73,258] The schematic structure and electric band structure of h-BN are shown in Fig. 8.[73,273] They have a wide bandgap of $\sim$5.9 eV and do not exhibit any optical absorption in the visible region of 390–700 nm. Compared to plasmon polaritons in graphene, the phonon polaritons in h-BN possess extremely high confinement and even lower loss.[259,260] h-BN shows natural hyperbolicity,[261,262] which can potentially be used for strong spontaneous deep UV emission enhancement around $\sim$210–220 nm,[258] Raman enhancement,[263] and biosensors.[154] Recently, scanning near-field optical microscopy (SNOM) has been adopted for studying the plasmonics of graphene in the mid-infrared region.[264–268] By combining graphene and h-BN to form a heterostructure, highly confined low-loss plasmons can be observed using

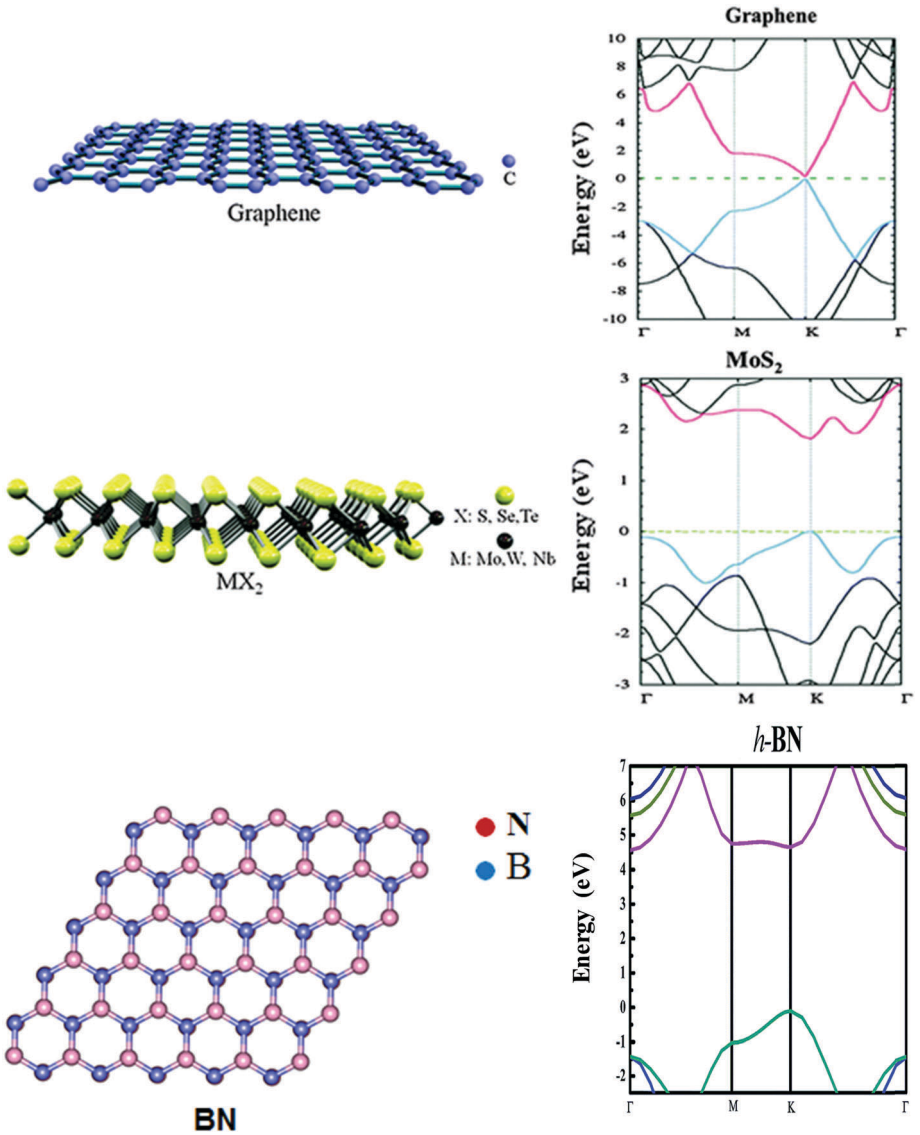

Fig. 8 The schematic structures of graphene and MX_2 type crystals. Reproduced with permission.[272] Copyright 2015, Royal Society of Chemistry. The schematic structures of h-BN. Reproduced with permission.[73] Copyright 2014, Royal Society of Chemistry. The electric band structures of graphene and MoS_2. Reproduced with permission.[272] Copyright 2015, Royal Society of Chemistry. The electric band structures of h-BN. Reproduced with permission.[273] Copyright 2015, Royal Society of Chemistry.

SNOM which shows high sensitivity.[259] A graphene moiré superlattice has been created by placing a graphene monolayer on an h-BN film, producing collective oscillations of electrons contributing to infrared plasmons.[269,270]

3.3 Properties of hybrid nanostructures of metal/2D materials

Because of the strong plasmonic effect induced by the metal nanomaterials in the hybrid nanostructures, some properties of the 2D material component, *e.g.*, photocatalysis, PL, and optoelectronics, will be altered and enhanced by the metal part. To date, the hybrid nanostructures of metal nanomaterials/2D materials have been widely explored in various plasmon-enhanced applications, including plasmon-enhanced optical signals (*i.e.*, PL, SERS, and SPR sensors), plasmon-enhanced photocatalytic reactions (*i.e.*, photodegradation of organic pollutants and water splitting), and plasmon-enhanced optoelectronic devices (*i.e.*, solar cells and photodetectors). We will discuss these applications in the section on plasmon-enhanced applications (Section 4). On the other hand, the plasmonic resonance of the metal component will be greatly tailored after hybridization with the 2D material component because plasmonic resonance is highly dependent on the dielectric function of the surrounding medium.[59] In addition, an active plasmon-exciton reaction triggers the "hot electron" transfer from the metal NPs to the 2D materials, which will dampen the plasmonic resonance of metal nanostructures or change the absorption of the 2D materials, *etc.*[274–277] In this section, three typical types of optical properties of the hybrid nanostructures will be reviewed, including the synthetically tunable plasmon resonances of metal NPs, the electrically tunable plasmon

resonances of metal nanostructures, and the tunable absorption of 2D materials.

3.3.1 Synthetically tunable plasmon resonances of metal NPs. The integration of metal NPs with graphene as a hybrid nanostructure offers a means of tailoring the LSPR of metal NPs. After being combined with graphene, the LSPR of metal NPs exhibits redshifts due to the large dielectric functions of graphene compared to those of water, air, or organic capping molecules.[278–280] For instance, when Ag NPs are located on top of graphene, the LSPR of the metal NPs can be systematically tuned by changing the layers of graphene.[278] Fig. 9(a) shows the transmittance spectra of 4 nm-diameter Ag NPs on bare glass and graphene of 1, 2, and 3 layers on glass. The LSPR of the Ag NPs is approximately 420 nm when the Ag NPs are on the bare glass. However, the LSPR of the Ag NPs shifts to 425, 430, and 440 nm when the layer of graphene added between the Ag NPs and the glass substrate is increased from 1 to 2 and 3, respectively.

In addition, if the imaginary part of the dielectric function of the 2D nanomaterial component is large, such as graphene (n_g = 2.4 + i·1 for graphene),[278] the LSPR of the metal component can be drastically dampened and become broad. As shown in Fig. 9(b), the plasmonic resonance of Ag NPs on graphene is dampened and broadened to some extent with increasing graphene layers, compared to Ag NPs on the bare glass. The intensity of plasmonic resonance is decreased from 0.60 to 0.52 after 3 layers of graphene are inserted between the metal NPs and the glass.[278] This variation may be primarily attributed to the energy (or hot electrons produced *via* plasmon excitation) transfer from Ag NPs to graphene, which dissipates the electric-field concentration on the surface of Ag NPs, resulting in a decrease in the amplitude of their plasmonic resonance. Recently, a strong coupling through charge transfer and local electric fields was proven in the hybrid nanostructures of metal NPs/graphene.[274–277] The time scale of energy relaxation after

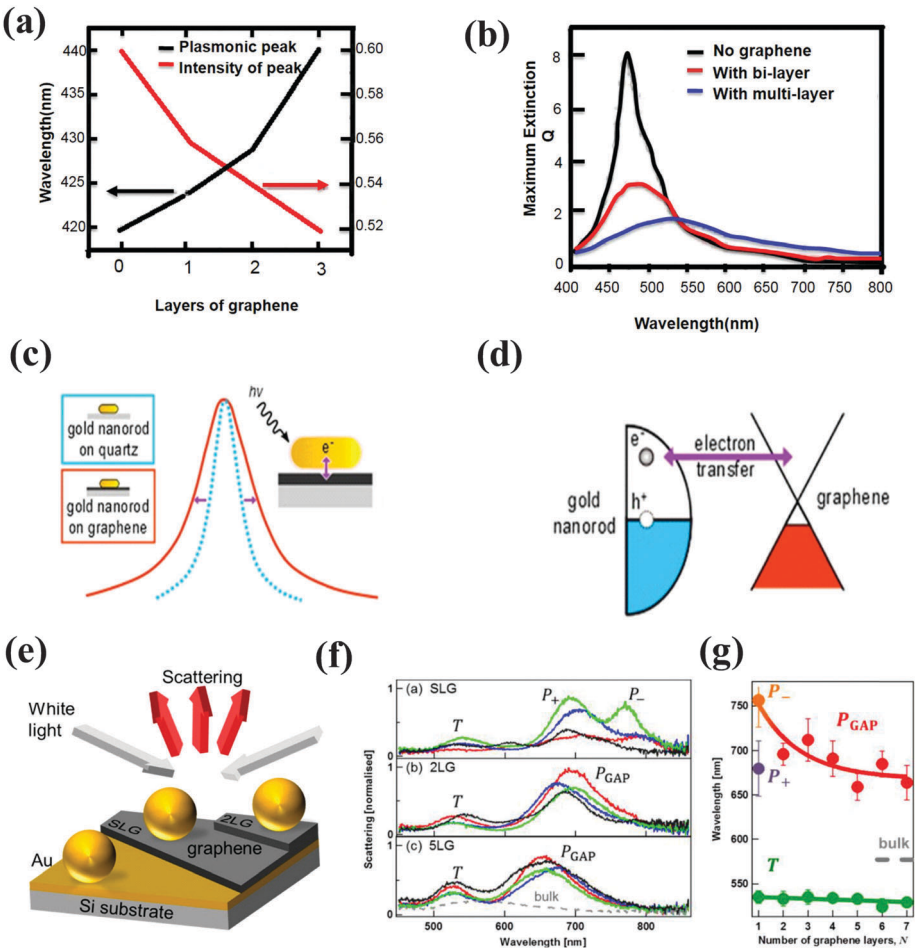

Fig. 9 (a) Plasmonic resonance frequency and amplitude with respect to the number of graphene layers, and (b) simulated Q-values of Ag disks with 10 nm thickness and 40 nm diameter without graphene, with a 0.7 nm graphene layer, and with a 2 nm graphene layer between the Ag disk and the glass substrate. Reproduced with permission.[278] Copyright 2012 Wiley-VCH Verlag GmbH & Co. KGaA, Weinheim. (c) Schematic of the plasmon linewidth in plasmonic nanorods with or without graphene, and (d) a schematic energy diagram illustrating charge transfer between an Au nanorod (left) and graphene (right) following plasmon-induced hot electron generation. Reproduced with permission.[281] Copyright 2013, American Chemical Society. (e) Schematic of a graphene sandwiched plasmonic coupling system, (f) dark-field single particle scattering spectra of four Au NPs on SLG, 2LG, and 5LG, and (g) resonance wavelength of the plasmonic T, P^+, P^-, and P_{GAP} modes for increasing the numbers of graphene layers, N. Reproduced with permission.[284] Copyright 2013, American Chemical Society.

photo-excitation and the efficiency of electron transfer between the Au NPs and graphene were determined by comparing the line widths obtained from the individual metal NPs on glass and graphene using single-particle dark-field scattering and PL spectroscopy. As shown in Fig. 9(c), the plasmonic resonance of the metal NPs exhibited a 13 nm broadening due to the presence of graphene. Analysis of the plasmonic line width yields an average electron transfer time of 160 ± 30 fs, and charge transfer between the Au nanorods and the graphene support occurs with an efficiency of ~10%.[281] Understanding the hot electron transfer is very important for future applications of light harvesting with plasmonic metal NPs and efficient hot electron acceptors in plasmon-assisted chemical reactions. On the contrary, it is not beneficial for plasmon-enhanced sensors if the damping of the metal NP plasmons on the graphene layer exists, which reduces the localized light intensity. Inserting a thin dielectric such as HfO_2, Al_2O_3, or water between the graphene layer and the metal NPs is an efficient method to reduce the plasmon damping process on graphene.[282,283]

Although the plasmonic resonance of metal NPs is tunable by simply placing the metal NPs and graphene together, *i.e.*, the metal NPs are placed on top of graphene, the shift is too slight to attain adequate light modulation. Based on experimental studies of plasmons in NP dimers, the plasmonic resonance can also be tailored through a spacer component between the NPs.[285–296] Recently, graphene was introduced into an NP-film coupling system to realize substantial spectral tuning in the visible-to-near-infrared region.[284,297] As shown in Fig. 9(e–g), the hybrid nanostructures are composed of a film/spacer/NP coupling system by introducing different layers of graphene between the upper Au NPs and the lower Au film as a sub-nanospacer. The coupling mechanism for this system is mainly due to the plasmonic coupling between the particle and its image within the metal substrate.[284] From the scattering spectrum (Fig. 9(f)), three plasmonic peaks can be observed when a graphene monolayer is used as the nanospacer, which is attributed to three modes, transverse plasmons (T) at approximately 500–600 nm, dipolar resonance (P^-, $P^- = P_{CTP} - P_{GAP}$), and quadrupolar plasmonic resonance (P^+, $P^+ = P_{CTP} + P_{GAP}$) at approximately 700–900 nm.[298,299] The P_{CTP} presents the charge-transfer plasmon (CTP) between the upper Au NPs and their image. The P_{GAP} plasmon gives the dipole located near the gap (“GAP plasmon”). As the layer of graphene is increased from 1 to 6, the P^+ disappears, and the dipolar resonance blue-shifts undoubtedly occur from 800 nm to 650 nm (Fig. 9(f) and (g)).[284,297] Thus, a wavelength shift of nearly 150 nm is observed, which implies that the plasmonic graphene-sandwiched hybrid design is a very efficient light modulator. The screening effect of graphene plays a significant role in modulating the plasmonic resonance.[297] The nature of the charge transfer and gap plasmon hybridization depends on the conductivity of the gap; and thus, different effects may be expected for graphene and other 2D materials such as h-BN. It is worth saying that the system of NP-film coupling system is used as a model system to provide a very controlled and experimentally reproducible equivalent of an Au NP dimer. Otherwise, it is very difficult to achieve a coupling system with a sub-nanometer gap. Therefore, understanding the tunability of plasmonic resonance in the NP-film coupling system by 2D materials is very important because an efficient modulation of light has a high potential for perfect absorbers,[300–302] Raman enhancement,[303,304] and light-harvesting applications.[182]

Other 2D materials such as MoS_2 and h-BN also have the ability to tailor the plasmonic resonance of metal NPs because the 2D materials can affect the surrounding media of the metal NPs when they hybridize with the metal NPs.[126,155] In addition, electron transfer from the metal to the 2D materials is also possible.[305]

3.3.2 Electrically tunable plasmon resonances of metal nanostructures. The surface conductivity of a single layer of graphene can be expressed by two terms, which represent the intra- and interband transitions, respectively and are given by the following expressions in the low-temperature limit:[164]

$$\sigma_{\text{intra}}(\omega) = \frac{ie^2}{\pi\hbar}\left[\frac{E_F}{\hbar(\omega + i\gamma)}\right] \quad (10)$$

$$\sigma_{\text{inter}}(\omega) = \frac{ie^2 k_B T}{4\pi\hbar}\left[\ln\left|\frac{\hbar\omega - 2E_F}{\hbar\omega + 2E_F}\right| - i\pi\theta(\hbar\omega - 2E_F)\right] \quad (11)$$

Due to the Pauli blocking of the interband transition, the Fermi level of a single layer of graphene can be electrostatically controlled by applying different gate voltages to the FET structure. Regarding eqn (10) and (11), the surface conductivity of graphene is largely dependent on the Fermi level E_F, and E_F can be modified *in situ* by the applied back-gate voltages determined by the following equation:

$$E_F(\Delta V_{CNP}) = \hbar v_F \sqrt{\pi a \Delta V_{CNP}} \quad (12)$$

where $\Delta V_{CNP} = V - V_{CNP}$ is the voltage difference between the applied back-gate voltage and the back-gate voltage close to the charge neutral point (CNP), $v_F = 10^6$ m s^{-1} is the Fermi velocity, and the parameter $a = 7.56 \times 10^{14}$ m^{-2} V^{-1} is estimated using a simple capacitor model.[272]

With the capability to modulate the Fermi level by applying different gate voltages, the *in situ* control of the optoelectronics becomes possible. Recently, the modulation of the plasmonic resonance frequency of metal nanostructures has been successfully realized by exploiting the electrically tunable optical transitions of graphene in the hybrid metal–graphene system.[306] By tailoring the Fermi level of graphene, the plasmonic resonance range can be efficiently modulated over a broad region from the terahertz (THz) and infrared to the visible wavelength region.[172,307–309]

The tunable resonance around the THz region in the metal/graphene system was first demonstrated by applying a gate voltage.[172] The active control of the wave in a range of 0.25 to 2.75 THz was realized based on the coupling of the CVD-grown graphene and the metal materials, as shown in Fig. 10(a). With the FET structure, a modulation depth of 11.5% with an applied bias of 10.6 V was realized by the split-ring resonator that was directly evaporated on top of the large area of graphene grown by CVD (Fig. 10(b)).[172] Murphy *et al.* reported an Au/graphene

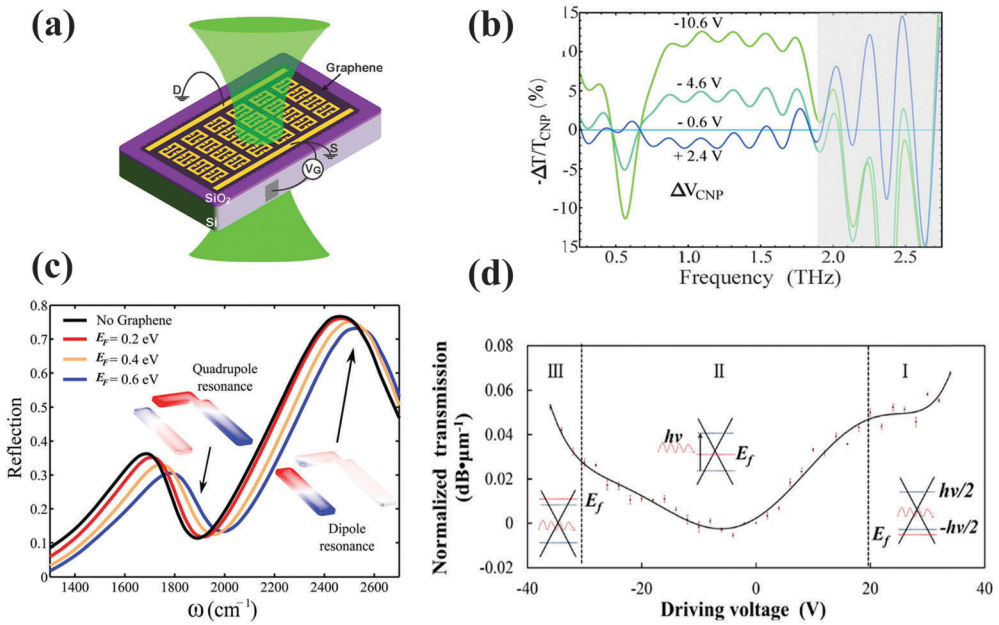

Fig. 10 (a) The schematic of the gated CVD graphene/THz-metal material device for back-gate voltages, and (b) the corresponding transmittance normalized to the value near the charge neutral point (CNP) for a selection of spectra. Reproduced with permission.[172] Copyright 2013, American Chemical Society. V_g = 0, 2, 4, 6, 8, 10, 11, 12, 13, and 14 V, with $\Delta V_{CNP} = V_g - V_{CNP}$. (c) Reflectivity spectrum from the metal surface without (black) and with graphene calculated using COMSOL simulations. Reproduced with permission.[164] Copyright 2013, American Chemical Society. Insets: Charge distribution on the metal surface at the dipolar (right) and the quadrupolar (left) resonances. (d) The main panel shows the modulation depth at different driving voltages, which is normalized to the zero bias transmission (dB μm^{-1}). Reproduced with permission.[308] Copyright 2014, American Chemical Society. The gray dashed lines represent the boundary of three regions that correspond to the different injection state of the graphene sheet denoted by I, II, and III. Correspondingly, the three insets show the energy band diagram of graphene in the three regions, and the arrow in the inset of region II represents the absorption of an incident photon.

modulator comprised of a periodic array of narrow slots in a metal layer patterned on top of a graphene sheet. They observed that plasmons from the graphene can be confined to conductive boundaries; thus, a 100% tunable resonance peak in transmission could be predicted.[310]

A broad electrical tuning of a graphene-loaded plasmonic dipole antenna was also demonstrated in the mid-infrared region.[307] With the double resonant antenna, the maximum modulation depth can be larger as 30% over a broadband of 650 nm ($\sim$140 cm^{-1}, $\sim$10% of the resonance frequency).[176] In addition, the tunable optical response of the dipole nanoantenna can be switched on and off by different gate voltages. By tuning the Fermi level of graphene, the resonant wavelength at approximately 3200 nm was spilt into two resonant peaks at 2900 nm and 3050 nm due to the in-phase and out-phase coupling between the graphene plasmonic and metal plasmonic.[291]

The controlled Fano resonance of metal nanostructures around this infrared region was realized in the metal nanostructure–graphene system by applying a gate voltage. The effects of plasmonic damping in a Fano resonance at approximately 2 μm have been observed.[174] A blue shift of the Fano resonance of the metal nanostructures without noticeable damping of its spectral sharpness has been observed in the hybrid metal surface/graphene system. As shown in Fig. 10(c), reflectivity spectra from the metal surface without (black) and with graphene obtained using the COMSOL theoretical simulation were plotted.[164] The quadrupolar resonance and the dipole resonance (*i.e.*, charge distribution on the metal surface at the dipolar resonance) shifted to the blue wavelength region after graphene was introduced. Then, the blue shift of plasmonic resonance continues after applying a gradually increasing gate voltage. A widely controlled metal surface consisting of plasmonic antennae on graphene integrated with an optical cavity can be created as an electrically tunable perfect absorber and a high speed (20 GHz) and ultrathin (thickness below $\lambda_0/10$) optical modulator with a modulation depth of 100% over a broad wavelength range (5–7 μm) can be achieved.[173]

Visible range SPP modulation with a static modulation depth of up to 0.07 dB μm^{-1} was realized based on a graphene–Ag nanowire hybrid structure (Fig. 10(d)).[308] The dual confinement of charge density and electromagnetic energy in the vicinity of the nanowire dramatically enhanced the light–matter interaction and caused the optical response to be in the visible range. By applying more than 25 V to the gate electrode, the charge carrier concentration around the Ag nanowire reached nearly 0.921×10^{14} cm^{-2}, which is very efficient for tailoring the Fermi level for visible light.

3.3.3 Tunable absorption peaks of 2D materials. In addition to the fact that the plasmonic resonance of metal nanomaterials can be tailored by 2D materials, the absorption peak of 2D materials can also be changed in the hybrid nanostructures of metal nanomaterials and 2D materials.[283] Theoretically, the

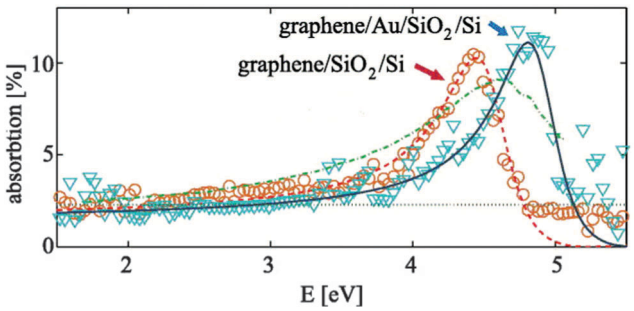

Fig. 11 The absorption of a graphene layer when the graphene is placed on the Au/SiO_2/Si film and SiO_2/Si film. A blue shift (0.35 eV) of the prominent absorption peak was observed. Reproduced with permission.[283] Copyright 2015, AIP Publishing LLC.

plasmonic resonance-induced local fields with high electromagnetic energy near the interface of metal NPs and the medium modify the dielectric/optical properties of the medium.[311] The optical properties of graphene (Fig. 11) in the ultraviolet (UV) range are dominated by the excitonic red-shifted interband transition near the *M*-point in the Brillouin zone of graphene, resulting in a dominant asymmetric absorption peak positioned at approximately 4.6 eV. By changing the doping level of graphene, the balance between the electron–electron (e–e) interactions and the electron–hole (e–h) interactions can be modified, which causes a change in the shape and position of the absorption peak. A useful strategy to introduce doping of graphene is through interaction with metal nanomaterials.[283] After combining graphene with a metal film (*i.e.*, transferring graphene to the top of an Au or a Cu film), the absorption peak of graphene was found to be blue-shifted (350 meV) and symmetrical. The main reason for this result is that interaction with the metal substrate suppresses e–h interactions. The charge transfer between graphene and the metal substrate can be reduced by inserting a dielectric layer between graphene and metal substrate.[283]

In addition, the absorption peaks of other 2D materials, such as h-BN, have also been tailored using metal plasmonics in hybrid nanostructures.[155] Upon plasmonic excitation, the penetration of the surface of the plasmonic field into the interfacing 2D materials with spatial decay kinetics modifies the dielectric/optical properties of the 2D materials. The typical absorption spectrum of the h-BN nanomaterials at approximately 230 nm is red-shifted to 310 nm after hybridization with Au NPs. The shifting of the absorption peak of the h-BN nanomaterials is attributed to the reduction in the bandgap as a result of the strong near-field energy close to the interface. Electronic rearrangement at the metal/h-BN interface results in the equalization of the Fermi levels and lowering of the energy bandgap relative to the work functions at the interface. Considering that the magnitude of the modified energy bandgap depends on the radially penetrating depth and propagation of transient plasmonic waves at the interface, the optical properties of h-BN can be efficiently tailored using plasmonic nanomaterials.[311]

3.3.4 Summary of the optical properties of hybrid nanostructures of plasmonic metal/2D materials. In this section, three types of optical properties of hybrid nanostructures have been discussed, including synthetically tunable plasmon resonances of metal NPs, electrically tunable plasmon resonances of metal nanostructures, and tunable absorption of 2D materials.

First, the plasmonic peak of metal nanomaterials can be tuned after 2D materials are integrated with metal nanomaterials because the plasmonic peak is strongly affected by the surrounding environment.[54] Compared to pure metal nanomaterials, the plasmon absorption of the metal nanomaterials in the hybrid nanostructures can be drastically dampened and broadened, mainly due to the "hot electron transfer" from the metal nanomaterials to the 2D materials.[274–277] To restrain the "hot electron transfer", a dielectric layer should be inserted between the metal NPs and 2D materials.[274,282,283]

Second, the modulation of the plasmonic resonance frequency of metal nanostructures has been successfully realized by exploiting the electrically tunable optical transitions of graphene in the hybrid metal–graphene system. To tailor the Fermi level of graphene by applying different gate voltages with FET structure, the plasmonic resonance range can be efficiently modulated in a broad region from the THz and infrared regions to the visible wavelength region. Currently, the modulation depth is 11.5%, 30% (100% for Fano resonance of metal nanostructures), and 0.07 dB μm^{-1} in the THz, infrared, and visible wavelength regions, respectively.[172,307,308] To achieve more efficient modulation, two key points should be considered: (1) strategically designing specific metal nanostructures that exhibit a resonance frequency near the region to be controlled, and (2) the plasmonic resonance of the designed metal structures should be sensitive to the electrical doping of graphene.

Third, the absorption peak of 2D materials has also been changed in the hybrid nanostructures of metal nanomaterials and 2D materials. These 2D materials are chemically doped through interactions with metal nanomaterials. As a result, the bandgap of 2D materials can be modified. The magnitude of the amended energy bandgap depends on the radially penetrating depth and propagation of transient plasmonic waves at the interface.[311] Thus, the optical properties of 2D materials can be efficiently tailored using plasmonic nanomaterials.

4. Plasmon-enhanced applications

Hybrid nanostructures display unique optical characteristics that are derived from a close conjunction of the localized plasmon resonance from metal NPs or metal nanostructures and the unique physicochemical properties of 2D materials, as well as the synergistic interactions between the two components. They have been widely studied in areas such as device physics, energy science, environmental science, information science, and biotechnology.[312] Here, we will mainly introduce and discuss three research directions, plasmon-enhanced optical signals, plasmon-enhanced photocatalytics, and plasmon-enhanced photoelectronics, using fundamental concepts, device principles, and application examples. From the viewpoint of applications, the solution-processed hybrid nanostructures of metal NPs/2D materials always have a large specific surface area; therefore,

they are widely used in plasmon-enhanced photocatalytic reactions, SERS, and as interfacial materials in solar cells.[74–81] The hybrid nanostructures of metal nanostructures/2D materials prepared using physical methods have a precise design and are compatible with micro- and nanofabrication techniques; therefore, they are commonly used in photodetectors (PDs), surface plasmonic resonance (SPR) sensors, and electrodes of solar cells.[161–163]

4.1 Plasmon-enhanced optical signals

Some 2D materials (*i.e.*, GO, MoS_2, and h-BN) can exhibit distinct PL. However, their atomically thin dimensions provide a significant challenge for the interaction of light with the materials and results in reduced light absorption and emission, which restricts their use in a variety of applications such as sensor/detector applications.[313] The introduction of metal nanomaterials into 2D semiconductors can efficiently solve this problem *via* active plasmon-enhanced effects. Recent papers describing the hybrid nanostructures of metal NPs and 2D semiconductors used for applications involving PL can be reviewed from several aspects. First, mutual interactions between the plasmonic effect of metal nanomaterials and the PL of the 2D semiconductors in the hybrid nanostructures can enhance or quench the original optical responses of 2D semiconductors.[71,305] PL broadening or shift can also be observed in intense plasmonic-exciton interactions.[71,305] Second, the hybrid nanostructures can also be employed as sensors for tailoring the optical response of other visual species, such as fluorescers.[314] In addition, hybrid metal NP/2D materials can efficiently enhance the Raman signals of the analytes attached to the hybrid nanostructures, which is termed SERS. Moreover, the use of hybrid nanostructures as SPR sensors has also been widely reported.[315–317]

4.1.1 PL enhancement

4.1.1.1 PL enhancement of 2D semiconductors by the plasmonic effect. In a hybrid nanostructure consisting of a metal component and a 2D semiconductor, a very strong plasmonic electric field in the vicinity of the metal nanomaterial can enhance the PL of the 2D semiconductor itself if an appropriate hybrid nanostructure is rationally designed. The electrons in 2D semiconductor will be in the excited state after the absorption of photons, there are two decay channels for such excited state electrons in relaxation process: non-radiative (*i.e.* in the form of phonons) and radiative (*i.e.* in the form of photons) transition. The re-emission of photons is attributed to the radiative recombination of the excited electron. The utilization of the plasmonic effect in the hybrid structure not only increases the absorption of a 2D semiconductor due to the strengthened electric field but also has the capability to optimize the decay channel of non-radiative and radiative transition.[70] There are several non-radiative pathways by which an excited semiconductor may be de-excite. Among these pathways, electron transfer is one of the important non-radiative de-excitation routes, which is strongly affected by the spacing between the metal nanomaterials and semiconductors. Generally, direct contact or adequate small spacing facilitates electron transfer. In addition, there are some longer-distance non-radiative pathways, such as the non-radiative pathway of plasmon excitation. This process may still happen even in quite considerable spacing between excited semiconductors and the metal nanomaterials. In metal/2D semiconductor hybrid nanostructures, the metal nanomaterials and the 2D semiconductors can be designed to be in direct contact with each other or separated by a spacer layer. When the 2D semiconductors are directly attached to the metal NPs surface or separated by a very thin spacing, electron transfer is usually increased, and the PL intensity is typically decreased.[305] When the 2D semiconductors and metal nanomaterials are separated by an appropriate spacer layer, electron transfer may be blocked, and the non-radiative transition (*i.e.* electron transfer, particularly) will be restrained.[71] The final PL depends on the overall contribution of the excitation, radiative, and non-radiative decay rates.[318]

In addition to the change in PL intensity caused by the plasmonic effect, peak broadening and shift can also be observed using different contact types between metal nanomaterials and 2D semiconductors.[319,320] Fang *et al.* examined the PL of MoS_2 in hybrid nanostructures.[305,321] By direct deposition of Au NPs on top of a MoS_2 monolayer, a hybrid nanostructure without a spacer between Au NPs and the MoS_2 monolayer was obtained. As shown in Fig. 12(a), after the Au NPs were applied to the MoS_2 surface, a slight decrease in PL peaks at approximately 652 nm and 682 nm was observed. Moreover, the addition of Au NPs also resulted in the red-shifting and broadening of the MoS_2 PL spectra. The main reason for this result is that if the metal NPs directly contact the 2D semiconductor, plasmon-induced hot electrons can be transferred from the metal NPs to the MoS_2 by a non-radiative process, leading to the narrowing of the MoS_2 band gap and a phase transition.[319]

To restrain the non-radiative process, a dielectric layer can be inserted between the 2D materials and metal NPs. Recently, silica–Au–PVP (poly-4-vinylpyridine) core–shell NPs have been used to obtain a hybrid metal NP/2D semiconductor.[71] Because the insulating PVP can block the electron transport between Au NPs and MoS_2, the non-radiative process is effectively reduced. As a result, a PL intensity that was nearly twice as large was obtained, as shown in Fig. 12(b). To further enhance the PL intensity, a MoS_2 sandwiched plasmonic coupling system consisting of an Au nanocube/PVP/MoS_2/HfO_2/Au film structure has also been reported.[322] The PL of the MoS_2 was enhanced by 2000-fold compared to the pure MoS_2 for two principal reasons: (1) the dielectric PVP and HfO_2 layers efficiently restrained the quenching and (2) strong plasmonic coupling was formed in the cavity between the Au nanocube and the Au film.[322] Based on the principle of plasmon-enhanced PL, other dielectric materials, such as Al_2O_3 and small organic molecules, can also be used as insulator spacers to optimize the competition between exciton quenching and plasmonic field enhancement.[274,282,283]

In addition to the integration of metal NPs in 2D semiconductors,[175,177] the combination of 2D semiconductors with metal nanostructures for PL enhancement has been recently reported.[160] Researchers have found that both emission enhancement due to metal nanostructure scattering and absorption enhancement of the 2D semiconductor due to the localized near-field effect play important roles in enhancing the PL intensity.

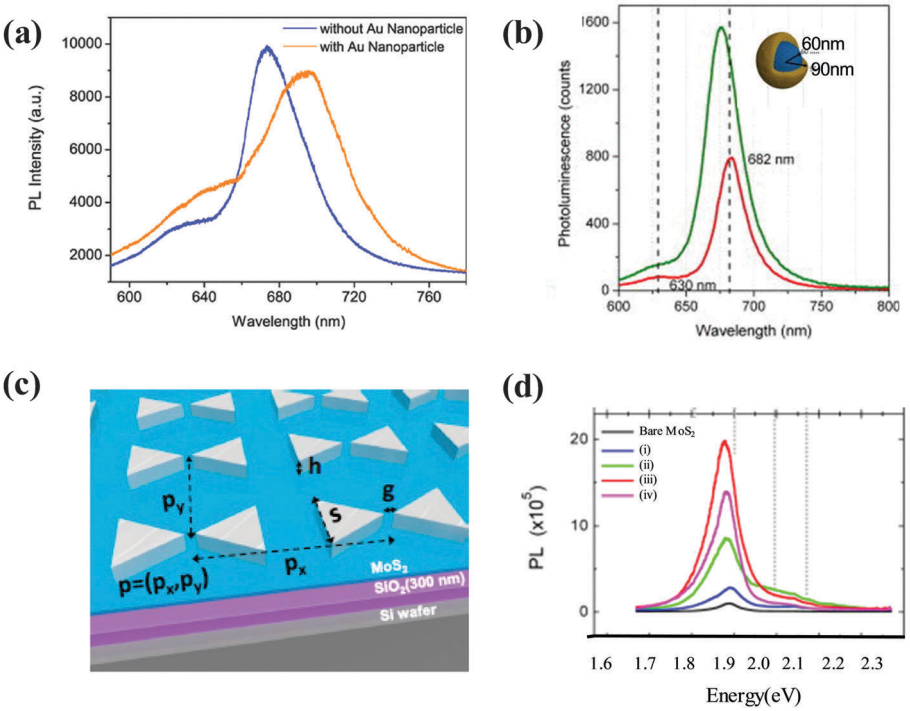

Fig. 12 (a) PL spectrum red-shifting and broadening were found after the 5 nm diameter Au NPs were deposited on the MoS_2 structure. Reproduced with permission.[305] Copyright 2014, Wiley-VCH Verlag GmbH & Co. KGaA, Weinheim. (b) PL spectra of monolayer MoS_2 on silica with (green) and without (red) Au nanoshells. Reproduced with permission.[71] Copyright 2014, AIP Publishing LLC. The nanoshell dimensions are indicated in the inset graphic. (c) Device schematic showing the geometrical factors of a bowtie array: gap separation (g), the thickness of the metal deposition (h), the side length of a triangle (s), and unit cell dimension or pitch ($p = (p_x, p_y)$). (d) PL spectra of bare MoS_2 (black) and four different patterns. Reproduced with permission.[160] Copyright 2015, American Chemical Society. (i) s = 100 nm, p = (400 nm, 500 nm); (ii) s = 100 nm, p = (400 nm, 300 nm); (iii) s = 100 nm, p = (300 nm, 200 nm); and (iv) s = 170 nm, p = (500 nm, 800 nm).

Agarwal *et al.* reported a PL enhancement in a MoS_2 semiconductor with an integrated plasmonic nanoantenna array.[160] As shown in Fig. 12(c), an Ag-bowtie nanoantenna array supporting SPR has been added to the top of the MoS_2 monolayer. The strong exciton–plasmon coupling enables considerable light–matter interaction in the excitation and emission stages, resulting in significant PL enhancement. To demonstrate the effect of the plasmon resonance frequency in the metal nanostructures on the excitation of MoS_2, the authors fabricated four patterns with different plasmonic resonance frequencies by changing the array architectures. Fig. 12(d) shows the PL spectra of a bare MoS_2 and four different hybrid nanostructures, in which the PL spectrum depends strongly on the positions of the plasmonic resonance frequency. For example, the plasmonic absorption peak in the metal arrays (iii) is well-matched with the wavelength of the excitation laser; the largest PL enhancement of nearly 40-fold is achieved mainly due to the absorption enhancement excited by the localized plasmonic near-field. In addition, a maximum PL enhancement in the high-energy region occurs in the array (ii) due to strong scattering in the area shown in the array (ii), which enhances the emission of MoS_2. Therefore, emission enhancement is also necessary for overall PL enhancement.

In addition to the MoS_2 2D semiconductor showing a high PL in the visible region, h-BN 2D materials also exhibit a bright luminescence in the deep-violet region.[258] Considering the biocompatible nature of h-BN, it is possible that this material may be used in bioimaging applications. To further enhance the PL properties of h-BN 2D materials, researchers could consider producing a plasmonic effect in the violet region. Al NPs are an excellent candidate material and show an efficient plasmonic effect in the violet region.[323]

In summary, the PL intensity of 2D materials with hybrid nanostructures can be enhanced by enhanced light absorption, reduced non-radiative rates, and improved emission, which enables the creation of highly efficient emitters and optical imaging devices.

4.1.1.2 PL enhancement of other species by the plasmonic effect and PL sensors based on the hybrid nanostructures. The PL enhancement of other species can also be realized. On the one hand, the optical response of outside fluorescent molecules can be directly enhanced by a metal NPs/2D semiconductor. For example, a 40-fold PL enhancement of Rhodamine B (RhB) molecules has been achieved using a graphene monolayer inserted between the RhB molecules and Ag NPs. The reason for this effect is attributed to π–π stacking interactions between graphene and the RhB fluorophore that lead to efficiently radiated emission and strong plasmonic enhancement.[324]

On the other hand, hybrid nanostructures of metal NPs and 2D semiconductors can be designed for efficient optical

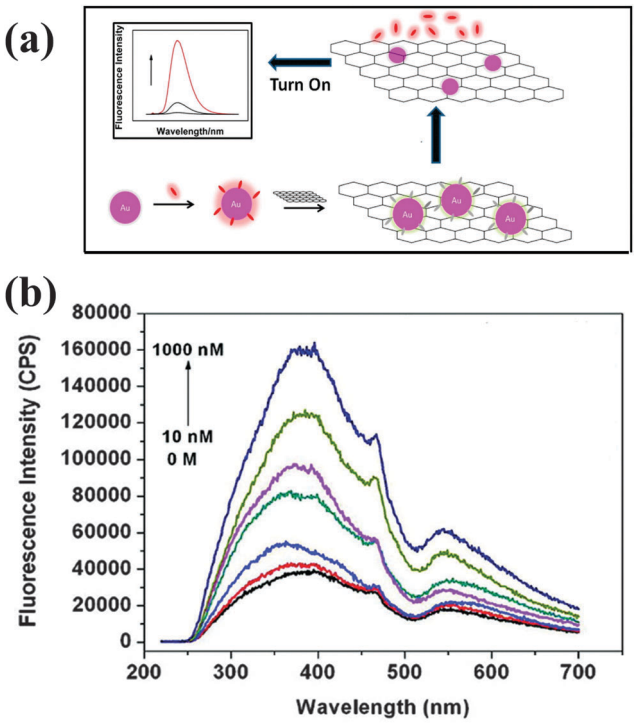

Fig. 13 (a) Schematic illustration of fluorescence sensing based on fluorescence quenching of GO by decorating Au NPs and enhancement by the leaching of Au NPs. Reproduced with permission.[314] Copyright 2014, American Chemical Society. (b) Fluorescence spectra of G–Au NCs in 5 mM glycine solution upon the addition of increasing concentrations of Pb^{2+} ions (0 M–1000 nM) under optimal conditions.[330] Copyright 2012, American Chemical Society.

sensing by tailoring the PL of GO. GO shows intrinsic and tunable fluorescence in the red/near-infrared, visible, and ultraviolet light regions and offers exciting opportunities for nanomedicine and chemo-biosensing.[326] The principle is shown in Fig. 13(a).[314] GO exhibits inherent fluorescence enhancement at a particular wavelength. When the metal NPs are attached to the surface of GO, the fluorescence of GO is entirely quenched by fluorescence resonance energy transfer between GO sheets and metal NPs, which is a fundamental requirement for designing this type of sensor. However, the strong fluorescence will recover if new additives are introduced. The degree of recovery of the fluorescence of GO in the hybrid system is proportional to the concentration of the new additives, which is called "Turn-on" fluorescence detection. With this mechanism, the metal NP/2D semiconductor composite can be used as an efficient sensor to detect biomolecules and heavy metal ions.[314,327] Recently, hybrid nanostructures of metal NPs/GO have been widely used as "Turn-on" fluorescence detectors[325,328–330] and "Turn-off" fluorescence detectors for environmental detection and biotechnology applications.[314] For example, detection of Pb^{2+} was reported by designing a hybrid Au/graphene system as a novel "turn-on" fluorescent sensor, as shown in Fig. 13(b).[330] In this system, the PL of GO was quenched by Au NPs without the target antigen because of the fluorescence resonance energy transfer between the GO and Au NPs. After the Pb^{2+} was attached to the surface of hybrid nanostructures, the PL of GO was gradually enhanced depending on the Pb^{2+} concentration, mainly due to the GO probe quenched initially by Au NPs, which accelerated the leaching of Au NPs by the Pb^{2+} in the presence of both $S_2O_3^{2-}$ and 2-mercaptoethanol. After measuring a series of PL intensities of the GO probes with different concentrations of Pb^{2+} ranging from 50–1000 nM, a linear relationship between the PL intensity and Pb^{2+} concentration was obtained, and the detection limit for Pb^{2+} was 10 nM. Moreover, a selectivity detection test was also performed by detecting other metal ions, such as Zn^{2+}, Ca^{2+}, Mg^{2+}, Cd^{2+}, Al^{3+}, Li^{+}, Cr^{3+}, and Ni^{2+}, and the intensity of the GO probes was not apparently changed, which was attributed to their weak ability to leach Au NPs. Therefore, the integration of metal nanomaterials with 2D materials can be used to produce efficient PL sensing with high detection sensitivity and selectivity.

4.1.2 SERS. SERS is a physical phenomenon in which weak Raman signals of analytes are remarkably enhanced when they are close to the surface of plasmonic nanomaterials. To date, substantial efforts have been made to design and fabricate efficient SERS substrates with ultrasensitive detection, high reproducibility, and even multifunctional applications for environmental detection, clinical diagnosis, and chemical analysis.[331,332] The SERS mechanism is mainly attributed to chemical and electromagnetic enhancements. It is well accepted that metal nanomaterials can produce an electromagnetic field enhancement due to the strong plasmonic effect.[333–336] In addition, 2D materials (*i.e.*, graphene and GO) with significant chemical enhancements have been reported, and the charge transport between the detection molecules and 2D materials is the main reason for this phenomenon.[278,337–342] Recently, the Raman enhancement effect has been demonstrated in an h-BN monolayer due to dipole formation between the h-BN and detection molecules.[263] In addition to the plasmonic effect, charge transport, and dipole formation, which are the main determining factors of SERS enhancement, some structural characteristics of 2D materials also play important roles in improving the Raman signals of detection molecules, such as the π–π structure, which traps more molecules, and the large surface area, which concentrates more molecules.[63] Therefore, the hybridization of metal nanomaterials and 2D materials enables the detection of signals at the maxima, allowing hybrid nanostructures as promising SERS substrates.[74–79]

4.1.2.1 Hybrid nanostructures as SERS substrates for detection of target molecules. Great achievements have been made in the design and fabrication of hybrid nanostructured SERS substrates. Initially, hybrid metal/graphene systems that were used as SERS substrates were fabricated using thermal evaporation of Ag nanospheres on top of CVD grown graphene.[278] SERS experiments demonstrated that the hybrid device showed a stronger SERS enhancement than that of single Ag nanospheres or the graphene SERS substrate.[79,343,344] Because the morphology of metal NPs strongly affects SERS signals, other shaped metal NPs have also been added to the graphene surfaces of hybrid SERS substrates.[345] Au nanorods with graphene or GO have

shown to significantly enhance the SERS signal of crystal violet (CV) and allow the detection of pesticides with a limit of detection of approximately 5×10^{-7} M.[346,347] The Raman signals of nitro explosives can be enhanced by four orders of magnitude when a GO–Au nanocage hybrid platform is applied.[348] In addition, Au nanohexagons on graphene and a cooperative graphene–Au nanopyramid system have also been reported as excellent SERS substrates.[349,350]

In addition to simple combinations of metal NPs with graphene used as hybrid SERS substrates, some unique hybrid nanostructures have been reported recently. Because molecules directly absorbed on the plasmonic metal surface will induce unfavorable disturbances including chemical adsorption-induced vibrations, charge transfer between the metal and molecules, photo-induced damage, and metal-catalyzed side reactions, researchers have attempted to use an ultrathin layer of 2D materials as an inert shell.[159,351] Zhang *et al.* placed CVD-grown graphene on top of a tightly packed Au nanosphere film and demonstrated an active, graphene-veiled plasmonic metal SERS substrate.[159] Tian *et al.* also reported graphene shell isolated metal NP enhanced Raman scattering.[352] In addition, metal NPs added to vertical graphene sheets have been used as a 3D SERS substrate with high reproducibility.[77] Recently, a sandwiched metal NP/graphene/metal film hybrid system has received increased attention due to its promise of being used in SERS applications.[284,297,303,353–356] As shown in Fig. 14(a), the sandwiched hybrid structure is composed of Ag NPs with a diameter of 20 nm residing on an ultrathin graphene spacer layer covering an Ag film.[63] Due to the 2D nature of graphene, very strong plasmonic coupling was achieved *via* the sub-nanometer gap between the upper metal NPs and the lower metal film. In addition, the increased ability of graphene to absorb and concentrate target molecules further makes it an attractive candidate for SERS applications (Fig. 14(b)).[63] Because Au and Ag materials are rare and expensive, researchers have attempted to find other less expensive metal materials to use them as efficient SERS substrates. Cu NPs are a promising SERS substrate and are widely used in biotechnology. However, the enhancement factor (EF) of Cu NPs is only 1.57×10^4, which is considerably lower than that of Au and Ag NPs. Our group has proposed the construction of a Cu NP/graphene/Cu film coupling system by directly evaporating Cu NPs on top of graphene grown on a Cu foil.[89] Using two strategies, including the coupling between Cu NPs and Cu film and the use of optimized incident light to enhance the vertical component of the electrical field in the interaction with the Cu-NP image, one of the highest EF values (1.89×10^7) for the Cu SERS substrates has been achieved (Fig. 14(c) and (d)).

In addition to graphene and GO, which are popularly reported to combine with metal NPs and create excellent SERS substrates, hybrid nanostructures of metal NPs with other 2D materials (*i.e.*, h-BN, MoS_2) have recently been reported.[121,126,130,155,357–359] However, the hybrid nanostructures reported to date involve the straightforward combination of metal NPs with an h-BN or MoS_2 monolayer. More unique and complicated hybrid nanostructures with stronger interactions between metal NPs and h-BN and MoS_2 need to be further developed.

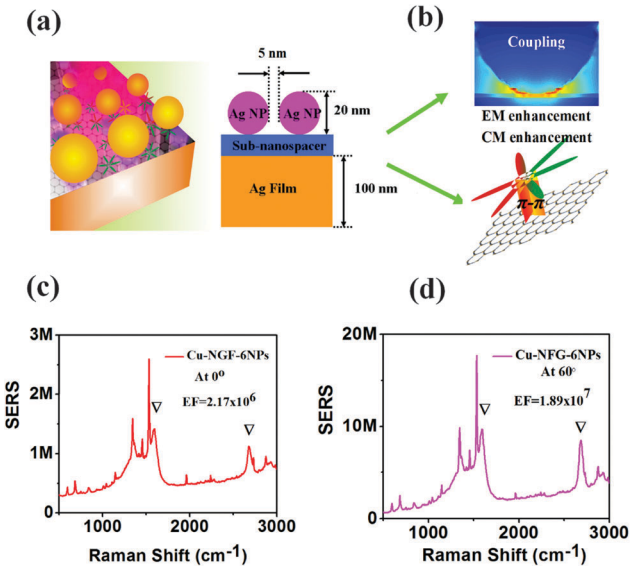

Fig. 14 (a) The 3-dimensional and cross-sectional schematic of graphene sandwiched with an Ag coupling system as a strong SERS substrate and (b) the impressive features of the SERS substrate possess a strong near-field due to NP-film coupling and a chemical mechanism enhancement from the monolayer graphene sub-nanospacer through interacting with target analytes owing to a strong π–π interaction. Reproduced with permission.[63] Copyright 2014, Wiley-VCH Verlag GmbH & Co. KGaA, Weinheim. CuPc Raman spectra detected on the Cu NPs/graphene/Cu film coupling system (Cu–NGF–6NPs) with the incident light (c) at 0 deg. and (d) at 60 deg. Reproduced with permission.[89] Copyright 2015, Royal Society of Chemistry. "∇" denotes the Raman signals from the monolayer graphene in the Cu–NGF system. The excitation wavelength is 532 nm. The accumulated time is 20 s, and the laser power is 5 mW.

4.1.2.2 Hybrid nanostructures as SERS tools to study other physical phenomena. First, hybrid nanostructures can be used to evaluate plasmonic near-field enhancement using the SERS technique because SERS enhancement is strongly related to its plasmonic near-field enhancement in plasmonic nanostructures. Because graphene and other 2D materials have well-known Raman spectra, they function as appropriate test materials for investigating the plasmonic effects of hybrid systems. Reich *et al.* demonstrated the strong near-field coupling in a hotspot between two Au nanodisks using Raman scattering of graphene (Fig. 15(a)).[166] Because near-field enhancement is hard to evaluate directly, they introduced a monolayer of graphene on top of an Au nanodisk dimer to study the coupling between the two Au nanodisks.

As shown in Fig. 15(b), the Raman intensity of graphene was significantly enhanced after the Au nanodisk dimer was applied, which indirectly reflects the strong near-field coupling between the two Au nanodisks. We also used the Raman spectrum of graphene to explain the strong plasmonic coupling between the upper Cu NPs and lower Cu film when graphene was used as a nanospacer.[112] It is important to note that a very recent report showed that quantum mechanical effects will emerge if the thickness between the upper metal NPs and the lower metal film approaches the atomic length scale in metal NP/metal film coupling systems.[361–364] Thus, it is imperative to

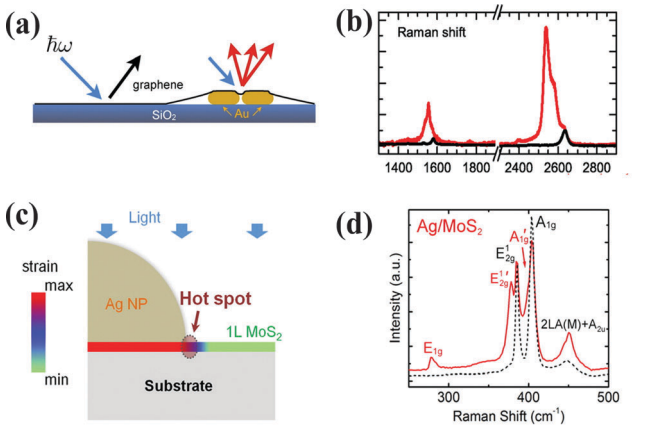

Fig. 15 (a) Schematic description of monolayer graphene covered on two Au nanorods, and (b) the Raman spectra of graphene obtained from graphene with (red line) or without (black line) plasmonic enhancement. Reproduced with permission.[166] Copyright 2012, American Chemical Society. (c) Schematic description of detecting strain using the plasmonic effect, and (d) the corresponding Raman spectra of MoS_2 with (red line) or without (black line) applying strain. Reproduced with permission.[360] Copyright 2014, American Chemical Society.

determine if a quantum effect exists in the NP/graphene/film hybrid system in the future when the SERS technique is used to study the plasmonic effects.

The powerful plasmonic enhancement can also be used to observe fine Raman bands that are not observed using normal Raman spectra. Recently, Baumberg *et al.* probed confined phonon modes using the SERS technique in CdSe nanoplatelets sandwiched between Au NPs and an Au film.[61] In addition, the hybrid nanostructure of an SERS substrate can also be used to monitor morphological changes in a 2D monolayer.[365] The Raman spectrum of a material with vibration information is its fingerprint. When the material morphology changes, its Raman spectrum also varies. However, a challenge remains in collecting Raman information from some nanomaterials such as MoS_2 without the assistance of the plasmonic effect. Tiny variations in morphology are particularly difficult to observe. Using a MoS_2 layer sandwiched with a strong plasmonic coupling between the metal NPs and the metal film, the morphological changes in the middle MoS_2 layer have been well studied.[365] Moreover, local strain in the hybrid nanostructures can also be detected using the SERS technique because the Raman spectra of materials are strongly affected by the local stress. Wang *et al.* found that the hybrid nanostructures of SERS substrates can be used to probe the local strain at MoS_2 film/Ag NP boundaries.[360] Fig. 15(c) shows a schematic description of the strain detection using the plasmonic effect.[360] When Ag NPs are placed on top of the MoS_2 surface, local strain occurs near the MoS_2/Au NP boundaries. As a result, the Raman spectra of MoS_2 that undergoes local strain are changed, and the minimum change in the Raman spectra can be greatly amplified (Fig. 15(d)). Based on the change, the local strain can be evaluated. In conclusion, any physical phenomenon in hybrid metal/2D material systems that affects the Raman spectra of 2D materials, such as the plasmonic near-field, morphological changes, and local strain, can be studied using the SERS technique.

4.1.3 SPR sensor. In addition to the plasmon-enhanced PL and SERS, which have been extensively studied, an SPR sensor composed of metal/2D hybrid nanostructures has also been developed recently.[315–317] Using the refractive index sensitivity of SPR, plasmonic metal nanostructures can be used for chemical and biological sensing applications because a chemical or biological receptor–analyte interaction leads to a change in the plasmonic oscillation frequency. In addition, 2D materials have a large surface area, rich π-conjugation structures, and a flat surface, which make them promising building blocks for detecting molecules.[315] Therefore, the integration of 2D materials with metal NPs and nanostructures will further amplify the detection of signals and extend the application of these materials to different fields.[366–368]

An SPR sensor composed of a hybrid metal/2D material system has a typical structure of prism/metal film/2D materials/host molecules, as shown in Fig. 16(a).[179] Host molecules are added to the sensor to trap the analytes of interest, resulting in sensitive detection and efficient selection. A Kretschmann configuration can be used to excite surface plasmon-polariton on the 2D material–Au surface.[72,315,317] The following equation is used:

$$k_0 n_p \sin(\theta_r) = R_e(k_{sp}) = \mathrm{Re}\left(\frac{2\pi}{\lambda}\sqrt{\frac{\varepsilon_m \varepsilon_d}{\varepsilon_m + \varepsilon_d}}\right) \quad (13)$$

where k_0 is the free space wave vector of the excitation light, λ is the wavelength, K_{sp} is the wave vector of surface plasmon-polaritons, n_p is the refractive index of the prism, θ_r is the resonance angle, and ε_m and ε_d are the dielectric constants of the 2D material-coated metal surface and dielectric medium on the surface, respectively. If detecting molecules are attached to the surface, the refractive index of the hybrid nanostructures changes,[317] which can be obtained by measuring the SPR phase changes or angle of the reflected light.[317,366,369] The SPR sensors based on the hybrid nanostructures of metal/2D materials exhibit several advantages, including no requirement for labels, real time monitoring, and high sensitivity detection.

Based on recent studies, two key principles should be considered when designing a sensitive SPR sensor. The first is to create a hybrid nanostructure that shows a keen sensitivity to the refractive index of the environment. The second is to add host molecules to the hybrid nanostructures that have a strong selectivity for the analytes of interest. Among the hybrid nanostructures of metal/2D materials that function as SPR sensors, graphene covering a metal surface is a typical example.[317,370,371] Cosnier *et al.* reported the construction of an SPR immunosensor by adding a monolayer of graphene to an Au film.[370] Graphene was noncovalently functionalized using nitrilotriacetic acid (NTA) with polypyrrole and the pyrene groups and biotinylated cholera toxin (b-CT) as a receptor to detect the anti-cholera toxin in rabbits (anti-CT). As shown in Fig. 16(b), the SPR angle shifts after anti-CT introduction using pure Au (red) and graphene–Au (black) with NTA on the surface at two different anti-CT concentrations. At the same anti-CT concentration, the introduction of the graphene monolayer enhances the detection sensitivity by

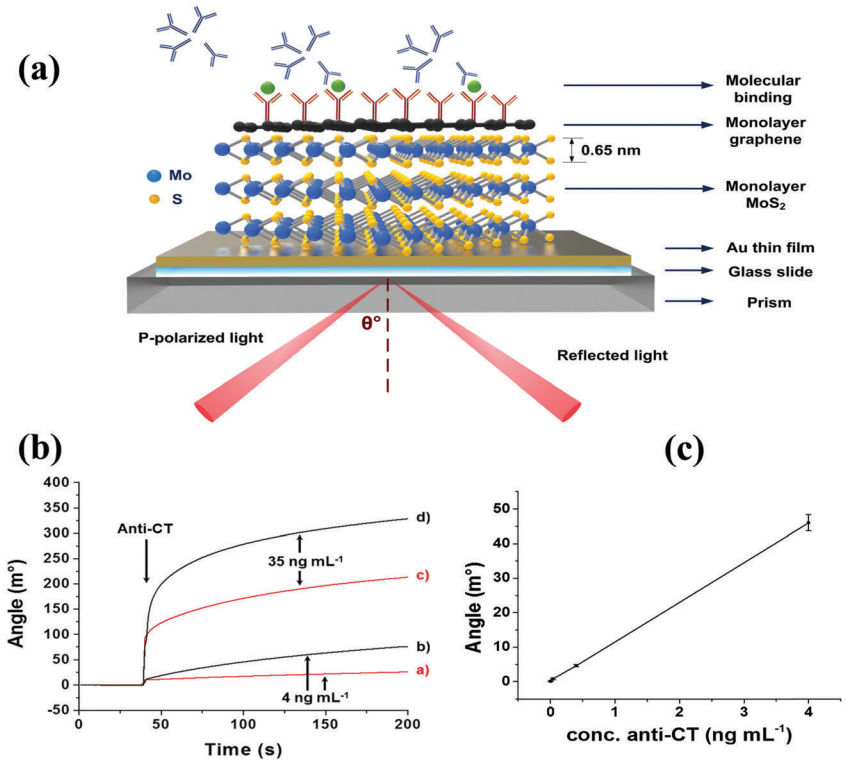

Fig. 16 (a) Schematic diagram of a graphene–MoS_2 enhanced SPR biosensor. Reproduced with permission.[179] Copyright 2015, Elsevier B.V. (b) The SPR angle shifts after anti-CT injection using pure Au (red) and graphene–Au (black) surfaces functionalized with polypyrrole–NTA/Cu^{2+}/b-CT at two different anti-CT concentrations (a and b: 4 ng mL^{-1} and c and d: 35 ng mL^{-1}), and (c) linear range of the graphene-based SPR immunosensor toward anti-CT. Reproduced with permission.[370] Copyright 2015, American Chemical Society.

approximately 2-fold. In addition, the SPR angle of the graphene/Au hybrid nanostructures is increased along with the anti-CT concentration from 4 ng mL^{-1} to 35 ng mL^{-1}. The SPR response was recorded by plotting the SPR angle and the anti-CT concentration after 50 s, and a linear relationship was obtained between the SPR angle and the anti-CT concentration between 0.004 and 4 ng mL^{-1} with a lower limit of detection (LOD) of approximately 4 pg mL^{-1} (Fig. 16(c)). To further enhance the sensitivity of the sensors, more than one type of 2D material has been integrated to utilize their collective advantages.[179] It has recently been reported that a phase-sensitivity enhancement factor of more than 500-fold was obtained in the proposed hybrid nanostructures of metal film/graphene–MoS_2 2D materials compared to the SPR sensing design without graphene–MoS_2 or with only graphene introduction.[179] Compared to other detection methods, such as amperometry or photoelectrochemical transduction, the SPR sensor based on the hybrid nanostructures of metal/2D materials has a lower LOD, implying promise for chemical and biological sensing applications in the future.[370]

4.2 Plasmon-enhanced catalytic reactions

A solar-driven photocatalytic reaction based on electron–hole pair generation in semiconductors is an economical and practical solution for green and renewable energy and has attracted an extensive interest in recent years. Many reports and reviews have been published regarding plasmon-enhanced catalytic reactions performed by utilizing the hybrid nanostructures of metal NP/inorganic semiconductor photocatalysts, especially for metal NP/metal oxide semiconductors hybrids (*i.e.*, TiO_2 and ZnO).[70] Recently, the incorporation of plasmonic metal NPs in 2D semiconductors (*i.e.*, GO, MoS_2) has resulted in the improved performance of high-efficiency photocatalysis.[372] Here, we will mainly focus on the plasmonic effect in the hybrid nanostructures of plasmonic metal/2D semiconductors and discuss their principles and applications in the photodegradation of organic pollutants and photocatalytic production of hydrogen.

4.2.1 Mechanisms for plasmon-enhanced catalytic reactions.

Three mechanisms have been reported for plasmon-enhanced chemical reactions with plasmonic metal/semiconductor hybrid nanostructures. The first mechanism involves the use of a strongly enhanced local field induced by metal NPs to improve light absorption of the 2D semiconductors in the hybrid nanostructures. As discussed in Section 3.1, the plasmonic effect produces an enhanced local electromagnetic field near the metal surface. The near-field enhancement caused by plasmon excitation decays nearly exponentially as the distance from the metal surface increases and extends from to 10 nm to 50 nm, depending on the shape and size of the metal NPs.[189] By using the high near field, the light absorption of semiconductors can be significantly improved, especially in the region that is close to the metal NPs in 2D semiconductors (Fig. 17(a)).[70] Because the electron/hole pair generation rate of a 2D semiconductor is proportional to the absorption intensity of the 2D

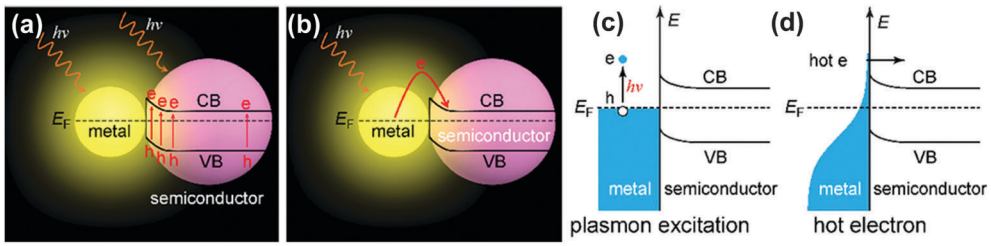

Fig. 17 Schematic illustration of the mechanisms for plasmon-enhanced chemical reactions with metal/semiconductor hybrid nanostructures. Reproduced with permission.[70] Copyright 2014, Wiley-VCH Verlag GmbH & Co. KGaA, Weinheim. (a) Plasmonic absorption enhancement. (b) Hot-electron effect. (c and d) Processes involved in the hot-electron effect. CB and VB represent the conduction and valence bands of the semiconductor, respectively. E_F refers to the Fermi energy level.

semiconductor, it is critical for the 2D semiconductor to absorb more light trapped by the metal NPs. To maximize the plasmonic absorption enhancement in the semiconductor, perfect spectral overlaps among the incident light, absorption of the 2D semiconductor, and LSPR of the metal NPs are highly desired. In addition, the structure and morphology of the hybrid structures are also critical factors because the local electric field enhancement derived from plasmon excitation is strongly dependent on the shape of the metal NPs and the distance from the metal surface.

The second confirmed mechanism for plasmon-enhanced chemical reactions is electron transfer.[62] Upon plasmonic excitation, the electron transfer process from the metal to the semiconductor occurs at the metal/semiconductor interface (Fig. 17(b)).[70] In general, the Fermi level of a 2D semiconductor is different from that of metal Au or Ag nanomaterials. Thus, a Schottky barrier forms at the junction interface between the metal and the semiconductor in the hybrid nanostructures, which blocks the electron transfer from the metal to the semiconductor. However, with the strong plasmonic excitation induced by the metal NPs, the hot electrons can transfer from the metal to the conduction band of the semiconductor. During this process, the plasmon quantum with the highest electron energy can decay non-radiatively into an electron/hole pair.[373] The decay rate depends on the size of the metal NPs and the radiative behavior of the plasmonic mode. In general, subradiant plasmon modes or small metal NPs can quickly generate electron/hole pairs. As shown in Fig. 17(c), the electron/hole pair is created when an electron is excited by the plasmon quantum from the Fermi level to an unoccupied state. Subsequently, coherence in the excited hot electron is lost, and a non-equilibrium Fermi–Dirac-type distribution is followed (Fig. 17(d)).[70] If photogenerated hot electrons have sufficient energies to overcome the Schottky barrier formed between the metal NPs and the semiconductor, they can successfully transfer to the CB of the semiconductor. As a result, even if a semiconductor has a weak ability to absorb light in the visible region, it obtains additional electrons from the metal NPs and thus conducts chemical reactions.[374,375] In addition, the holes remaining in the metal NPs show a slight oxidation ability and can be used for chemoselective oxidation reactions.[376,377]

The third possible mechanism is the scattering mechanism.[378] Metal NPs with sizes larger than 50 nm can efficiently scatter the resonant photons. Using this channel, the path length of photons near the semiconductors can be increased, thus enhancing the light absorption of the semiconductors. In addition to the large size, which is preferable for scattering, the shape and loading level of metal NPs in the hybrid metal NPs/2D semiconductor system also strongly influences scattering. Compared to the metal nanospheres, metal nanocubes, which have more edges and corners, show more efficient optical scattering. Excessively low or high loading of metal NPs is not beneficial for maximum light scattering.

In summary, the configurations of the hybrid metal/semiconductor systems and detailed arrangements of the two single components determine which mechanism is dominant in a particular photocatalytic reaction.[70,378] Plasmon-induced hot electron transfer occurs when the electrons in metal NPs are excited above the CB of the semiconductor. Close contact between the metal NPs and semiconductors is necessary for electron transfer. If a non-conductive spacer is inserted between the metal NPs and semiconductor, the scattering mechanism and the near-field enhancement are dominant. A stronger scattering can be achieved in the hybrid system if multiple scattering of resonant photons is obtained *via* the optical arrangement. In addition, the detailed arrangement of metal NPs and a semiconductor strongly affects the generation and separation of electron and hole pairs after plasmonic near-field enhanced absorption is achieved. Therefore, a rational study is required for the design of a hybrid metal/semiconductor system that exploits the maximum advantage of these mechanisms.

4.2.2 Photodegradation of organic pollutants. Photodegradation of organic dyes by semiconductor photocatalysts is an important and efficient strategy for environmental management and water purification. The photocatalysis process mainly involves (1) semiconductor excitation *via* the irradiation of incident light, (2) exciton generation, (3) reactive oxidative species formation, and (4) the oxidation of the organic dyes.[80] Compared to traditional metal NP/metal oxide photocatalysts (*i.e.*, Au NPs/TiO_2), the hybrid nanostructures of metal NP/2D semiconductors show several advantages, including (1) high adsorption capability for organic compounds, (2) strong π–π interactions with dye chromophores, (3) efficient photosensitized electron injection, and (4) slow electron recombination.[80] These features make hybrid nanostructures of metal NP/2D materials suitable candidates for photo-assisted degradation of dye pollutants in water.

Here, we will discuss several typical hybrid nanostructures of metal NP/2D materials and their applications in the photodegradation of organic dyes.

A simple hybrid nanostructure produced by directly adding Au NPs onto GO materials has shown excellent performance in the photocatalytic degradation of RhB dyes under visible light.[80] The RhB degradation rate was markedly increased under visible light irradiation after the introduction of metal NPs into GO. The authors attributed the deterioration of the dye pollutants to the reactive oxidative species produced by the Au NP/GO hybrid system under visible light irradiation. However, the roles of Au NPs in plasmon-assisted light absorption have not been discussed. Considering that the metal NPs are energetically unstable, tend to aggregate during the catalytic reaction, Su *et al.* fabricated Au NPs embedded into a hollow graphene nanoshell to avoid the aggregation of NPs efficiently and show robust catalytic performance.[379]

Relatively complex hybrid nanostructures have also been fabricated for visible-light photodegradation of organic pollutants.[60,380] Jin *et al.* reported a new photocatalyst with graphene-supported CdSe/CdS quantum dot (QDs)/Au NP hybrid nanostructures (QDs/Au–G).[60] Two types of photocatalysts exist including semiconductor GO and semiconductor QDs. As illustrated in Fig. 18(a), electrons are excited from the VBs to the CBs of the QD and GO semiconductors under visible-light irradiation. Meanwhile, the Au NPs can form a localized near-field to enhance light absorption in the visible region and increase the electron–hole pair generation rate at the surface of the semiconductors, and then the electrons are transferred into satellite Au NPs. The optical properties of QDs with or without Au NPs can be demonstrated using UV-vis and PL spectra (Fig. 18(b) and (c)). Before Au NPs are attached to the QDs, optical absorption consists of a broad wavelength range with a clear peak at 620 nm. In addition, a narrow PL peak of approximately 640 nm is clearly observed, as shown in Fig. 18(b). After the formation of a hybrid nanostructure of Au NPs and QDs, the intensity of the optical absorption is significantly increased compared to that of pure QDs with the same concentration (Fig. 18(c)). The absorption range also extends to longer wavelengths. Moreover, the dark field scattering image of the QD/Au system is obviously colored, compared to that of the QD system without Au NPs, which directly reflects the plasmonic enhancement of Au NPs on the QD semiconductor. The efficient electron transfer from QD_S to Au NPs can be demonstrated by a pronounced decrease in PL after Au NPs are introduced into QDs. Furthermore, a visible-light photocatalytic reaction using QD/Au–G has been shown (Fig. 18(d)). Compared to the QD–G composite, the QD/Au–G hybrid nanostructure exhibits a more efficient photocatalytic performance. After 1 h of irradiation with visible light, 65% of the original MB was decomposed when photocatalyzed by QD–G. In contrast, nearly 80% of the original MB can be decomposed using the QD/Au–G hybrid nanostructure, which further confirms that light absorption can be enhanced with Au NPs. If the QDs, Au, and GO nanomaterials are simply blended as a photocatalyst (QDs–Au–G), only 50% of the original MB can be decomposed, which demonstrates that the Au NPs arrangement is also critical for utilizing the plasmonic effect.

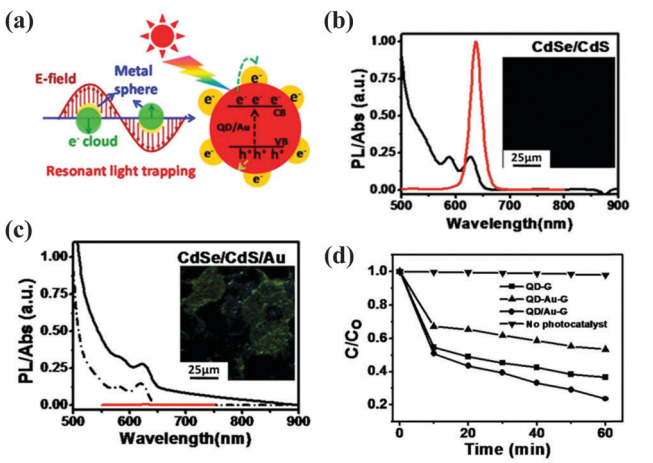

Fig. 18 (a) The charge separation and transfer processes of the graphene-supported CdSe/CdS quantum dots (QDs)/Au NPs system by the localized plasmonic effect. The UV-vis (black), PL (red) spectra, and dark-field scattering images (inset) of the (b) CdSe/CdS QDs, and (c) CdSe/CdS–Au system. In the (c), the black dotted line refers to CdSe/CdS, and the solid black lines refer to CdSe/CdS/Au. (d) Photodegradation of methylene blue (2.7×10^{-5} M, 10 mL) under visible light (>420 nm) over QDs/Au–G, QD–G, and QD–Au–G photocatalysts (3 mg), respectively. Reproduced with permission.[60] Copyright 2014, American Chemical Society.

4.2.3 Photocatalytic hydrogen production. Photocatalytic hydrogen production by splitting water using semiconductors has been demonstrated as a promising strategy for converting solar energy into an environmentally friendly fuel.[273] Recently, 2D semiconductors have attracted attention for use in photocatalytic hydrogen production due to their potential advantages, such as their larger surface areas and higher mobilities compared to conventional semiconductors such as TiO_2 and ZnO.[228,381] The principle of photoelectrochemical catalytic water-splitting is shown in Fig. 19(a).[382–384] Upon illumination, electron/hole pairs are generated and subsequently separated in the semiconductor if the energy of the photons is larger than the bandgap of the semiconductor. Then, the electrons are immediately transferred from the 2D semiconductor working electrode *via* the FTO substrate to the Pt counter electrode, where the H^+ in water is reduced to generate H_2 if the reducing power of the electrons is sufficiently high. Simultaneously, the holes remaining on the 2D semiconductor surface will oxidize OH^- to produce O_2 if the oxidizing strength of the holes is high enough. Recent studies have shown that introduction of plasmonic metal NPs into 2D materials can show both optical and electrical effects. By taking advantage of plasmon-enhanced light absorption, improvements in light absorption in the visible region have been realized. In addition, metal NPs play several roles in the electrical effects, including (1) enhancing the photogenerated electron transfer from MoS_2 to metal NPs for water reduction, (2) facilitating exciton separation in MoS_2 due to the metal/MoS_2 Schottky junction, and (3) providing plasmon-excited "hot electrons" for direct water reduction.[319,383]

The introduction of Au NPs into the GO materials produces better performance in the production of hydrogen *via* the

absorption enhancement of the GO/QD semiconductor and the increase in the electron–hole pair generation rate at the surface of the GO semiconductor.[60] In addition, an Au–MoS_2 composite is another plasmon-enhanced photocatalyst that produces efficient water-splitting in a photoelectrochemical cell (PEC).[383,385] Fig. 19(b) shows the absorption spectra of MoS_2, Au–MoS_2, and annealed Au–MoS_2. Compared to pure MoS_2, Au–MoS_2 shows two absorption peaks near ~620 and 670 nm, which are mainly due to plasmon-enhanced absorption. After applying the annealing treatment at 350 °C for 1 h in Ar, the semiconducting phase of the prepared MoS_2 is enhanced, and the interface resistance between the MoS_2 and Au NPs is reduced. As a result, the absorption intensity of the Au–MoS_2 composite is further improved, as shown in Fig. 19(b). The linear sweep voltammograms are shown in Fig. 19(c). Under visible light irradiation, the photocurrent increases from 100 μA cm^{-2} at 0.8 V for pure MoS_2 nanosheet-based PEC to 370 μA cm^{-2} after 3 wt% Au NPs are loaded on the MoS_2 nanosheet without the annealing process. Furthermore, the photocurrent is further increased to 790 μA cm^{-2} after Au–MoS_2 is annealed. Another method used to confirm that the plasmonic near-field effect plays a significant role in enhancing the light absorption is to tailor the wavelength of incident light.[319] As shown in Fig. 19(d), the measured current density increases from ~75 to ~125 μA cm^{-2} when the irradiated light wavelength is changed from off-resonance excitation at 532 nm to resonance excitation at 690 nm, which strongly reflects the important role of plasmon-enhanced absorption in enhancing the photocatalytic reaction.

In addition, complicated hybrid nanostructures have been proposed to enhance the photocatalytic performance efficiently. A sandwiched CdSe nanoplatelet has been constructed by inserting the ultrathin CdSe nanoplatelet between metal NPs and a metal film, which shows an enhanced water-splitting activity due to the excited plasmonic coupling between the metal NPs and the metal film (Fig. 19(e)).[61] Because the thickness of the CdSe nanoplatelet is only several nanometers, a strong plasmonic coupling throughout the CdSe material results in dramatically higher electromagnetic field enhancements in the complicated Au NPs/CdSe/Au film nanostructures compared to the simple hybrid nanostructure (*i.e.*, Au NPs/CdSe) (Fig. 19(f)). As a result, the Au NPs/CdSe/Au film photocatalytic nanostructure shows a 5-fold increase in the photocurrent, while the hybrid nanostructure of Au NPs/CdSe displays only a two-fold increase compared to the pure CdSe semiconductor. Considering the poor stability of MoS_2 and CdSe,[61,365] other semiconductors with better stability should be considered in future designs for water splitting.

After discussing recent reports of plasmon-enhanced catalytic reactions, a summary is presented. First, metal nanomaterials play a significant role in enhancing optical absorption in the visible region. Metal nanomaterials also produce many positive electrical effects, such as improving photogenerated electron transfer, facilitating exciton separation, and providing plasmonic "hot electrons".[289,373] Two important issues should be considered when developing high-performance plasmon-enhanced photocatalysts. (1) Typical metal NPs have a relatively narrow plasmonic resonance, which enhances light absorption

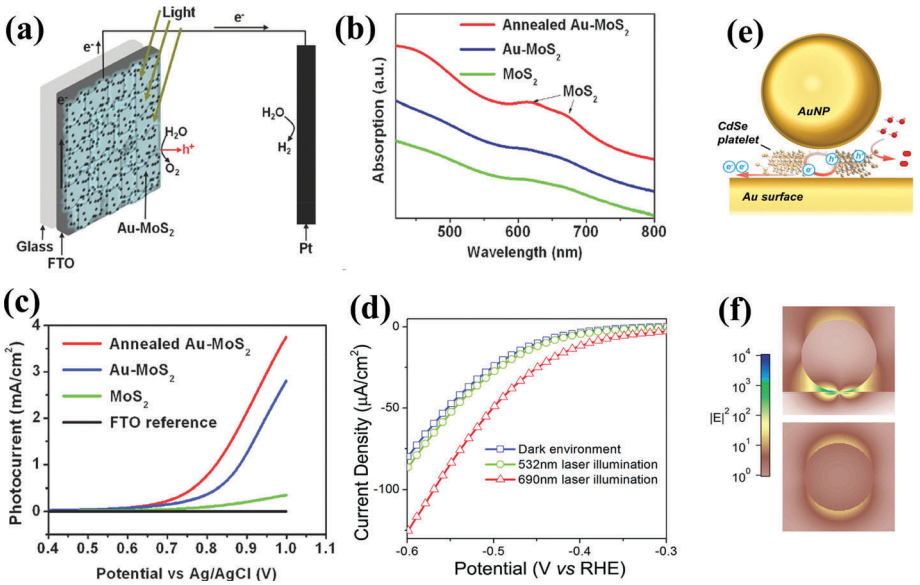

Fig. 19 (a) Schematic representation of PEC with Au/MoS_2 on FTO and commercial Pt wire as a photoanode and a photocathode, respectively. (b) UV spectra of MoS_2, Au/MoS_2, and annealed Au/MoS_2. Arrows point to the absorption peaks of MoS_2, and (c) linear sweep voltammograms for PECs with different working electrodes. Reproduced with permission.[383] Copyright 2014, Wiley-VCH Verlag GmbH & Co. KGaA, Weinheim. (d) The polarization curves of the hydrogen evolution reaction in the dark environment, 532 nm and 690 nm laser illumination. Reproduced with permission.[319] Copyright 2015, Royal Society of Chemistry. (e) Au NPs on Au film with atomically thin CdSe sandwiched between them, and (f) field enhancement at the optical bandgap of the CdSe platelets (λ = 548 nm) in the coupling-nanogap (top) and for an isolated AuNP (bottom) for comparison. Reproduced with permission.[61] Copyright 2015, American Chemical Society.

in a small region. For efficient utilization of sunlight, which is a broadband light source, hybrid nanostructures of metal nanomaterials/2D materials with broadband plasmonic absorption enhancement should be designed. (2) The photogeneration rate should be significantly enhanced, and recombination of charge carriers should be further reduced by fabricating high-quality 2D materials, carefully arranging metal components and 2D materials in the hybrid nanostructures, and modifying the interface between the metal nanomaterials and 2D materials.

4.3 Optoelectronics

Optoelectronics is a cross-discipline of photonics and electronics that revolves around the mutual conversion of light and electronics in semiconductor devices. According to the different functions and evaluation criteria, optoelectronic devices can be divided into photovoltaic cells (PVs), photodetectors (PDs), and light emitting diodes (LEDs), among others. 2D materials have a broad range of applications in optoelectronic devices due to their unique structures and optical properties.[6,9,14,16,17,25,383,386,387] First, a graphene layer can be employed as a highly transparent electrode in photoelectronic devices, including any PV, PD, and LED, due to its high conductivity.[1,15] Second, the energy bandgap tunability of 2D materials, such as GO and MoS_2, enables them to act as work-function tunable interlayers in PVs and LEDs.[184] In addition, graphene, GO, and TMDs display variable levels of photon absorption, allowing them to be utilized as photoactive materials in optoelectronic devices, especially photosensitive PDs, which have been reported recently.[24,35,184,386,388] An apparent reason to integrate metal NPs with 2D materials into hybrid nanostructures is to enhance the light absorption of 2D materials through the plasmonic light-trapping effect.[40] In addition, plasmon-induced hot-electron generation at metal component/2D material interfaces plays a significant role in photovoltaic devices.[62] Moreover, because 2D materials have a flat surface with a large area, they are very promising building blocks for devices. The comprehensive configuration and detailed arrangement of metal components and 2D materials used in hybrid systems have a strong influence on the functions of the devices and their applications.[12,81,389] In this section, we will mainly discuss two typical applications in optoelectronics for hybrid nanostructures of metal/2D materials, PVs and PDs.

4.3.1 Photovoltaic cells. Electricity converted from solar energy by solar cells is a clean and sustainable source of energy. Many types of PVs based on different structures and active materials are available, such as silicon solar cells, dye-sensitive solar cells (DSSCs), organic solar cells (OSCs), quantum dots solar cells, and perovskite solar cells. Hybrid nanostructures of metal/2D materials can be used in different positions of solar cells, depending on their functions.

Hybrid nanostructures of metal nanomaterials and graphene can be used as flexible and transparent electrodes in solar cells.[380] Initially, graphene was used to replace the fragile ITO due to its excellent electrical and mechanical properties.[188,390,391] However, monolayer graphene has low electrical conductivity (sheet resistance $R_s > 1000\ \Omega\ sq^{-1}$) and does not perform well as a working electrode due to defects and disruptions such as wrinkles and folding.[391,392] To solve this problem, metal nanomaterials can be integrated with the graphene to form composite electrodes.[392–398] In addition to the improved electrical conductivity of electrodes, the introduction of metal nanomaterials has other positive effects on the electrodes, including enhanced light absorption of devices and tunable working functions of the electrodes.[399] A typical example of a hybrid electrode consisting of a metal nanomaterial/graphene is made by placing Ag nanowires on top of a graphene monolayer. As a result, the R_s is decreased from 1050 to 64 $\Omega\ sq^{-1}$ after the Ag nanowires are applied, and the transmittance is nearly unchanged (94%).[382] Considering that Cu is relatively cheaper than Au and Ag, Cu nanowires have been used to replace Ag nanowires.[382] In addition, metal nanospheres can also be used to reduce the resistance of the electrode. Chen *et al.* selectively filled Au NPs in the cracks in a graphene film. The crack-filled graphene film (CFG) with Au NPs showed excellent electrical properties as a transparent electrode and produced a 30% enhancement of the power conversion efficiency (PCE) in graphene/Si Schottky solar cells.[400] Wang *et al.* also improved the efficiency of graphene–silicon Schottky solar cells by introducing Au NPs on top of a graphene electrode and attributed the remarkable improvement of device efficiency to the increased work function and improved electrical conductivity.[401] However, the optical effect of Au NPs on the device was unfortunately not addressed in the study. Due to the large dielectric index of silicon, light trapping is possible. Further measurements of the absorption of devices with or without Au NPs should be performed in future studies.

The hybrid nanostructures of metal/2D semiconductors can be used as an interlayer of photovoltaic cells. Solution-processed metal oxides and other semiconductors have been used as interlayers in thin-film solar cells. For instance, solution-processed GOs and MoS_2 have been reported to be alternatives to poly(3,4-ethylenedioxythiophene)–poly(styrenesulfonate) (PEDOT:PSS) in the hole transport layer (HTL).[229,236,244,246,402–407] However, the problem of absorbing sufficient light using thin-film solar cells, especially OSCs, is a current challenge. Among the techniques developed for light trapping, exploiting the plasmonic effect of metal NPs has been shown to be an efficient strategy.[190,408,409] The integration of metal NPs with 2D materials as hybrid nanostructures has been used not only to produce a solution-processed interlayer but also as an effective light-trapping strategy, *via* the plasmonic near-field effect and scattering effect, to enhance the absorption of solar cells.[389,402] In addition, metal NPs can produce positive electronic effects, including enhancement of electrical conductivity, increases in the exciton generation rate, and improvement of carrier collection.

As shown in Fig. 20(a), the HTL of the control device is the PEDOT:PSS. To enhance the device performance, a hybrid Ag NPs/GO layer has been introduced into the PEDOT:PSS as a composite HTL in the OSCs.[402] As a result, the J_{sc} and PCE are improved from 8.47 mA cm^{-2} and 3.23% for the reference to 9.43 mA cm^{-2} and 3.55% for the device with the Au/GO interlayer, respectively (Fig. 20(b)).[402] The increased J_{sc} with the Au/GO interlayer is mainly due to the strong plasmonic

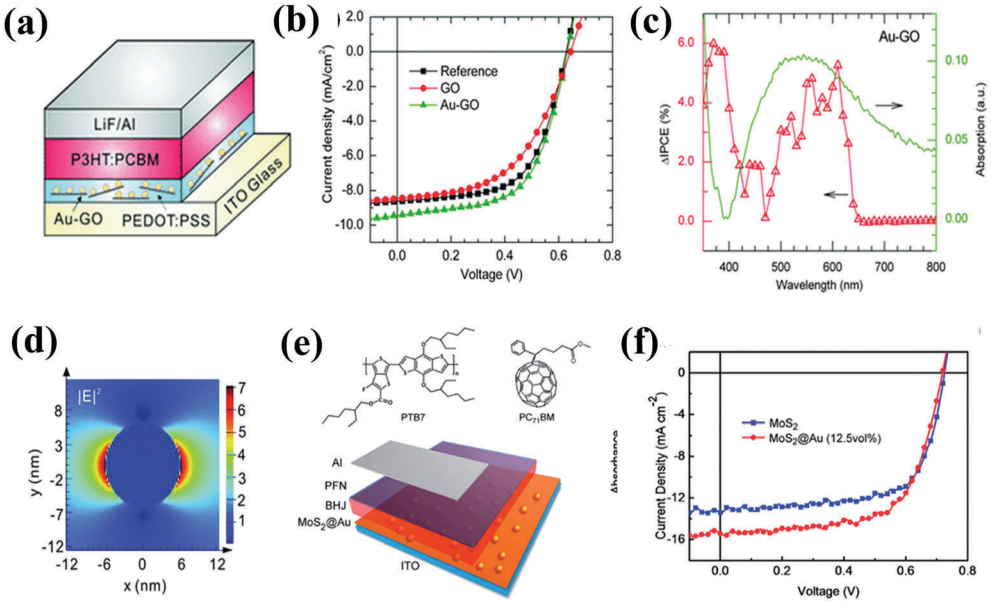

Fig. 20 (a) Schematic of organic solar cells with the structure of ITO/Au–GO or GO/P3HT:PCBM/LiF/Al, (b) J–V characteristics of polymer solar cells with and without GO or Au–GOs in the PEDOT:PSS layer recorded under AM 1.5 G simulated solar illumination at 100 mW cm^{-2}, (c) comparison of the differences in IPCE (ΔIPCE) after incorporating Au–GOs, and the absorption spectra of Au–GO, and (d) simulated light intensity ($|E|^2$) distribution around isolated Au NPs with the diameter of 6 nm in PEDOT:PSS at the plasmonic resonance position of 650 nm. Reproduced with permission.[402] Copyright 2012, Royal Society of Chemistry. (e) Chemical structures of PTB7 and $PC_{71}BM$ and a schematic of the device architecture with the structure of ITO/MoS_2@Au/BHJ/PFN/Al, and (f) the corresponding J–V characteristics. Reproduced with permission.[81] Copyright 2014, Royal Society of Chemistry.

effect of Ag NPs, which improves light absorption. As shown in Fig. 20(c), the trend of absorption enhancement is consistent with the pattern of monochromatic incident photon-to-electron conversion efficiency (IPCE) improvement, which implies that the J_{sc} increment is due to improved absorption.[402] The strong light-trapping effect of the Au NPs can also be illustrated by the theoretical near-field curve (Fig. 20(d)).[402] Under illumination with the incident light near the LSPR of Au NPs, a high electric field distributed near the Au NPs is observed. In addition, after the Au/GO hybrid is applied to the interlayer, the exciton generation rates of the devices are also significantly improved, which has been demonstrated using the steady state and dynamic photoluminescence measurements. Moreover, hybrid nanostructures consisting of metal NPs/MoS_2 have also been demonstrated as efficient HTLs.[81] Fig. 20(e) describes solar cells with an ITO/MoS_2 or MoS_2/Au HTL/active layer/electron transport layer/Al structure. The device parameters, including J_{sc}, FF, and PCE, are significantly enhanced from 13.36 mA cm^{-2}, 0.634, and 6.18% for the control device with only MoS_2 as an interlayer to 15.44 mA cm^{-2}, 0.652, and 7.25% for the device with the Au (12.5 wt%)/MoS_2 hybrid used as the interlayer (Fig. 20(f)). It is important to state that the device performance of solar cells is very sensitive to the Au concentration incorporated in the HTL. A high concentration (*e.g.*, 20 wt%) may lead to a device short, and a low level (*e.g.*, 2.5 wt%) produces negligible optical and electrical effects on the device. Using the optimized Au NPs/MoS_2 hybrid, the light absorption, photogeneration rate, and carrier collection were all well enhanced. Because h-BN as an insulator cannot be used in solar cells, few studies have reported the use of a hybrid of metal NPs/h-BN materials in solar cells to date.

2D materials can also be used as active layers. GO synthesized using chemical methods can be used to replace [6,6]-phenyl C_{61} butyric acid methyl ester (PCBM) in organic solar cells.[272] By blending the GO with poly(3-hexyl)thiophene (P3HT) and using it as an active layer, the OSC produces distinct photogenerated current. Other 2D materials have also been used as active layers of solar cells, such as MoS_2,[410] and WS_2.[411–413]

4.3.2 PDs. A PD is a photoelectronic device used for the detection of light. Graphene and other 2D materials have rapidly been developed as competitive building blocks for photodetection platforms.[415,416] The application of these 2D materials can be extended to include ultrasensitive and ultrafast detection of light in the terahertz frequency, infrared, visible, and ultraviolet ranges. Due to the low light absorption of 2D materials, the integration of metal components into these structures has become inevitable.[181] Two methods exist for enhancing the photocurrent in plasmon-enhanced phototransistors, including plasmonic near-field enhanced light absorption of 2D materials and plasmonic "hot electrons" directly produced by resonance excitation.

Graphene is the first channel material utilized in back-gate type PDs. However, as discussed in Section 3.2, the intrinsically weak light absorption (~2.3% for pristine graphene) and its short photocarrier lifetime lead to poor photoresponsivity (5×10^{-4} AW^{-1}) and internal quantum efficiency (6–16%). An efficient method to enhance light absorption is to utilize the near-field enhancement from the excitation of the plasmonic effect induced by the metal nanostructures. By placing the plasmonic nanostructures close to the graphene, the photoresponse of graphene-based PDs can be efficiently improved.[161–163]

Fig. 21(a) shows the layout of a graphene-based PD.[163] The graphene monolayer is transferred onto a silicon substrate covered with a 250 nm silica film, followed by placing the metal nanomaterials on top of the graphene monolayer. Then, Ti/Au electrodes are fabricated on graphene using EBL and act as source and drain electrodes, and the silicon substrate is the gate electrode. After the metal nanostructures are introduced, the photocurrent and external quantum efficiency of the hybrid device show a 15-fold enhancement compared to the graphene-based PD (Fig. 21(b)).[163] The photocurrent is attributed to plasmon-enhanced primary carrier excitation of graphene electrons and plasmon-induced hot electron transfer from the metal nanostructures into the graphene nanosheet (Fig. 21(d)). In addition, plasmonic nanostructures with a variable resonance can be used to amplify the photoresponse of graphene selectively to light at the desired wavelength, enabling highly accurate photodetection.[178] Besides the plasmonic effect, which affects the photocurrent of PDs, applied gate voltage also changes the photocurrent. Recently, a sandwiched plasmonic nanoantenna between two single graphene layers was designed as a graphene-based light-concentrating PD.[178] As shown in Fig. 21(c), the photocurrent near the scanning position (*e.g.*, −4 μm) can be efficiently enhanced to 80, 100, and 125 nA after the gate voltage is increased from 0, −20, or −40 V.

A new multifunctional graphene optoelectronic device can be designed by introducing additional semiconductors into the graphene-based PDs.[64] As shown in Fig. 21(e), the organic semiconductor pentacene, Au NPs, and graphene can be combined to fabricate a photodetecting device with a nonvolatile memory function for storing photonic signals. Pentacene acts as a light absorption layer in the device and provides a high photocurrent to the graphene channel. Au NPs, positioned between the tunneling and blocking dielectric layers, act as both a charge trap layer and a plasmonic light scatterer, which enable the storage of the incident light information. The proposed pentacene–graphene–AuNP hybrid photodetector not only performs well as a PD in the visible light range but also stores the photonic signal in the form of persistent current. The good photodetection performance of the device results from the plasmonic enhancement of the optical absorption and the photogating mechanisms in pentacene. The photodetector provides a photoresponse that depends on the wavelength of incident light; therefore, the signal information (both the wavelength and intensity) of the incident light is effectively committed to memory. The simple process of applying a negative pulse gate voltage can erase the programmed information.

In addition to the back-gate type PDs, hybrid nanostructures of metal nanomaterials/graphene applied to ionic liquid gated graphene FETs reveal a double-layer capacitance, which is 9.2–21 μF cm^{-2}, approximately 2–3 orders of magnitude higher than the back-gate capacitance using a layer of 90 nm SiO_2 (approximately 38 nF cm^{-2}).[417] Wu *et al.* have proposed a high-performance PD based on an ionic liquid gated plasmonic Ag NP/graphene nanohybrid FET, which takes full advantage of plasmon-enhanced light trapping by the metal nanostructures in addition to the high gating efficiency of the ionic liquid on graphene FET channel conductivity (Fig. 21(f)).[414]

Other 2D materials such as MoS_2 materials can also be used as channel materials.[418] Compared to the advantages of graphene, such as offering broadband detection and ultrafast sensitivity, the MoS_2 monolayer has attracted much interest due to its potential for achieving a very high responsivity of 7.5×10^{-3} AW^{-1} *via* the application of a back-gate voltage (V_g) of 50 V.[254] Moreover, by adjusting the number of layers in TMDC crystals, intriguing optical properties, such as an indirect to direct band gap transition, an increase in band gap energy (E_g), Van Hove singularities in the electronic density of states, and valley polarization, have been discovered in TMDCs (MoS_2, $MoSe_2$, WS_2, and WSe_2), which are essential for realization of highly efficient and advanced optoelectronic devices.[4] Similarly, the amount of light absorbed by such thin MoS_2 nanomaterials cannot satisfy practical requirements. To address the issue, metal nanostructures have been introduced into TMD based PDs. The active plasmonic effect in

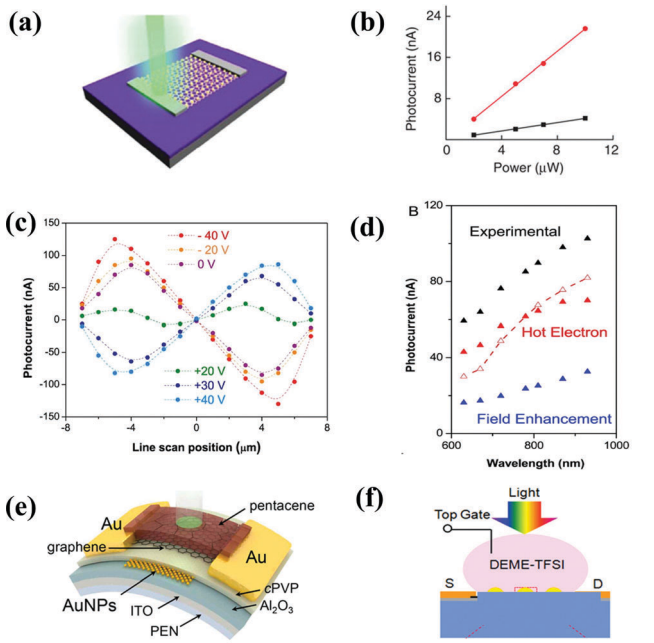

Fig. 21 (a) Schematic of a nonamer antenna on single-layered graphene with back-gated voltage and source and drain contacts, and (b) photocurrent generated as a function of laser power. Reproduced with permission.[163] Copyright 2011, Nature Publishing Group. The red and black lines indicate the response of a typical device with and without Au nanoparticles, respectively. The laser wavelength is 514 nm. (c) Measured photocurrent for gate bias voltage between −40 to +40 V for the plasmonic antenna-patterned device with the incident laser power of 10 μW, and (d) measured photocurrent and calculated photocurrent. Reproduced with permission.[178] Copyright 2012, American Chemical Society. (e) Schematic diagram of the device structure comprising a graphene photodetector with a pentacene light absorption layer and an AuNP charge trapping layer. Reproduced with permission.[64] Copyright 2015, American Chemical Society. In the device, the ITO acts as a gate electrode and Au as a source/drain electrode. (f) Schematic of the Ag NP/graphene hybrid FET photodetector with possible cation distribution changes around an Ag NP through LSPR generated Ohmic heating and/or direct energy transfer. Reproduced with permission.[414] Copyright 2014, Wiley-VCH Verlag GmbH & Co. KGaA, Weinheim.

metal nanostructures primarily improves the light absorption in the cross section of the underlying MoS_2 layer and naturally increase the photocurrent of PDs.[419,420] Regarding other materials in the 2D material family, optoelectronic applications are still in their early stages of exploration, and new findings in PD performance, as well as the diversity of the spectral range, can be anticipated.[253,421–424] Regardless of the 2D nanomaterial applied, the monolayer will inevitably encounter insufficient light absorption. It is worthwhile to study further the incorporation of metal nanostructures into these 2D material-based PDs in the future.

4.4 Other applications

After discussion of the typical use of hybrid nanostructures of metal/2D materials, the roles of plasmonic metal nanomaterials in the hybrid nanostructures are summarized. As shown in Table 2, both the optical and electrical effects play important roles in enhancing device performance. The optical effect includes near-field enhancement and scattering, and the electrical effect involves improving conductivity, carrier collection, and photogeneration rate; reducing carrier recombination, and producing plasmon-induced "hot electrons". Although the optical effect is currently the subject of extensive study, the electrical effect is still gradually developing. A multiphysics study of both the optical and electrical effects should be conducted in the future.

In addition to these typical applications, other plasmon-enhanced optical devices have been developed recently. The first typical example is a colorimetric detection device based on metal NP/2D material hybrids.[425] As discussed in Section 3.1, the LSPR wavelength of metal NPs highly depends on the size, shape, and refractive index of the medium in which they are dispersed. If metal NP aggregation occurs, for example, the color of the hybrid system is also changed; thus, a plasmon-enhanced optical sensor can be constructed.[185] In general, this colorimetric method is low-cost, stable, sensitive, and simple. More importantly, its ability to be used with the naked eye without the aid of any complicated instruments holds promising potential for applications in biotechnology and medicine detection.[425,426]

The second example is a plasmon-enhanced photothermal effect created by the hybrid nanostructures of metal/2D materials.[427–429] Under light irradiation, especially near-infrared light, metal nanomaterials can produce thermal energy *via* nonradiative decay.[430] In addition, 2D materials such as RGO can also absorb light in the broadband region ranging from UV to near-infrared wavelengths. Based on its nonradiative decay, GO can also serve as a photothermal source. By combining metal NPs and GO, the metal NPs enhance the light absorption of GO *via* the plasmonic near-field effect, and simultaneously, improved infrared absorption and photothermal effects are produced by the hybrid system. As reported by Lim *et al.*, a strong photothermal effect has been achieved in a GO coated Au nanorod hybrid system, which shows promise for biomedical applications, such as killing cells.[427]

Furthermore, the hybrid system of metal NP/graphene also shows an amplified photoacoustic effect, suggesting its implementation as an imaging probe.[431] Based on the enhanced near-infrared absorption and enhanced photothermal stability in the Au nanorod/RGO composite, an extraordinarily high photoacoustic effect in the 4–11 MHz operating frequency of an ultrasound transducer has been demonstrated in *in vitro* and *in vivo* systems.

A plasmon-enhanced laser is also an important research direction. By transferring graphene to the top of an Au film absorber mirror, stable mode-locking bulk lasers with wavelengths of 1, 2, and 2.4 μm have been fabricated.[432] Plasmon-enhanced near-infrared absorption in graphene with metal gratings has also been reported recently.[168,433] In addition, the hybrid Ag nanowire/graphene nanostructure can be used as a highly transparent and stretchable FET sensor for detecting some biomolecules.[434] In other words, more and more novel applications have been gradually reported based on the hybrid metal/2D nanostructures.

5. Conclusions and outlook

In summary, we have reviewed the recent advancements in various hybrid nanostructures of metal/2D materials, including their preparation, optical properties, and optically related applications. Although the development of metal nanomaterials and 2D materials has achieved significant progress, and broad interest has been stimulated, research on the hybrid nanostructures

Table 2 Summary of plasmon-enhanced applications

Application		Structures	Roles of plasmonic metal nanomaterials
Optical signals	PL SERS	Metal nanomaterials/ 2D materials	Optical effects: near-field enhancement and scattering
	SPR sensor	Metal film/2D materials	Optical effects: surface plasmon resonance
Photocatalytic reaction	Photodegradation Hydrogen production	Metal NPs/2D materials	Optical effects: near-field enhancement and scattering; Electrical effects: improving the photogeneration rate, reducing carrier recombination and plasmon-induced "hot electrons."
Photoelectronics	Photovoltaic cells	Metal nanomaterials/ 2D materials	Optical effects: scattering (for electrode and interlayer) Electrical effects: enhancing conductivity (for electrode), enhancing carrier collection and the photogeneration rate (for interlayer)
	Photodetectors	Metal nanostructures/ 2D materials	Optical effects: near-field enhancement and scattering Electrical effects: improving the photogeneration rate, reducing carrier recombination and plasmon-induced "hot electrons."

of metal/2D materials for optically related applications is still in its early stage. Here, we proposed several research directions for the hybrid nanostructures of metal/2D materials, which are worth being conducted or hold potential applications in the future.

The first interesting but challenging topic is to fabricate hybrid nanostructures of metal/2D materials with a precise control of the configuration of the overall nanostructures along with rational design and logical arrangement of each component in the hybrid nanostructures. As we discussed in Section 2, the preparation of hybrid metal/2D material systems is the foundation for studying the optical properties and various applications of these materials. However, due to the intrinsic difference in the crystalline structures and bonding nature between the metal components and 2D materials, the overall configuration and mutual contacts between these two types of materials are not well controlled. For example, when metal nanostructures are integrated with 2D materials, the interfacial contacts between the two components become challenging issues, which will dramatically degrade physical and chemical behaviors, such as light–matter interaction, exciton–plasmon coupling, and charge transfer between the metal materials and 2D materials. To resolve these problems, several aspects should be considered: the crystalline structures of 2D materials and metal nanomaterials should be further understood through experimental investigation and theoretical modeling; the material surface properties, such as surface wettability, surface energy, and surface charge, should be explored; and a third component, which would be compatible with both the metal component and 2D materials, could be inserted between the metal and 2D materials for effective relief of the mismatching effect. Another prevalent issue is that the configuration, size, positions, and crystal structures of metal nanostructures are not easy to control, and at the same time, the surface and structure of 2D materials are always jeopardized during the process of integration with metal nanostructures. In this situation, the existing preparation techniques should be improved, and new fabrication methods are expected to be developed.

Second, the roles of the interface between the metal components and 2D materials should be systematically studied and fully understood in the hybrid nanostructures. As discussed in Section 3 regarding the plasmonic resonance of metal nanomaterials and Section 4 regarding the plasmon-enhanced optical signals and plasmonic enhanced-photocatalytic reactions, the interface plays a crucial role in charge transfer between the metal components and 2D materials. However, a method to appropriately design and achieve the desired interface and understanding the exact role of the interface in charge transfer involved in the applications above are still open issues. A Schottky junction forms at the interface when a metal nanomaterial contacts a 2D nanomaterial. To achieve efficient charge transfer, the potential barrier at the interface, which is determined by the potential difference between the CB of the 2D semiconductor and the Fermi level of the metal nanomaterial, should be well elaborated. In addition, the bonding nature of the interface also influences the barrier. Under light irradiation, the plasmon-induced hot electrons can transfer from the metal to the CB of 2D materials after overcoming the potential obstacle. On the other side, the photogenerated electrons from the CB of the 2D semiconductor can directly transfer to the metal. Understanding and control of the charge transfer at the interface are paramount for studying the plasmon-enhanced behavior. Because the physical phenomena, including exciton generation, dissociation, and carrier transfer, last for a very short period, transient spectroscopy techniques, such as femtosecond transient absorption spectroscopy, could be used to study these physical processes across the interface.[435] Recently, the near-field interaction of graphene and plasmonic nanodisk resonators was investigated by femtosecond pump–probe measurements. The plasmon-induced hot carrier generation in graphene was dominated by direct photoexcitation in the near field. The interaction of plasmon-induced hot carriers in graphene with nanodisk polarizability gives rise to long-lived extrinsic optical anisotropy.[183]

Third, we discussed the plasmon-enhanced photodegradation of organic pollutants and water splitting for H_2 and O_2 production in Section 4.2, including the fundamental interest, device design principles, and technological importance. In fact, other plasmon-enhanced catalytic applications have already been reported for metal/metal oxide or other inorganic semiconductor hybrid nanostructures, such as the plasmon-enhanced photochemical synthesis.[70] In contrast to the photodegradation of organic pollutants, which involves a profound degradation reaction with products consisting of CO_2, H_2O, and other small molecules, plasmon-enhanced photochemical synthesis is a selective photosynthesis of fine chemicals, where partially oxidized products are often preferred.[436–438] With the assistance of excited resonance of plasmonic near-field effects and plasmonic ''hot electrons'', unique chemical structures have been synthesized by controlling the incident light wavelength or tailoring the interfaces between the metal components and semiconductors.[376,377,437,439] In addition, the plasmon-enhanced photocatalytic CO_2 reduction is also an interesting and important energy topic, which may give birth to another method for converting solar energy into chemical energy, such as CH_3OH and CH_4.[440] Compared to photocatalytic water splitting for H_2 and O_2 production, there is need for a reducing agent in photocatalytic CO_2 reduction that acts as a hydrogen source, such as H_2O, H_2 gas or NH_3.[438,441] These types of plasmon-enhanced applications have been reported using metal/inorganic semiconductor hybrid nanostructures;[442–444] however, scientific and technical challenges still exist. For example, the design of an inorganic semiconductor with selectively photocatalytic active sites is difficult, which constrains the development of efficient photochemical synthesis.[376,377,435–437,439] Moreover, the conversion efficiency for CO_2 to $CHOH_3$ and CH_3 fuels is still low and far from the demand for practical applications.[438,441–443,445,446] Metal/2D hybrid nanostructures are a promising approach. A preferred structure or optical property would enable the metal/2D nanostructures to be widely used in these application fields.

The fourth interesting topic is the non-metal plasmonic effect, which has been observed recently.[59] Non-metal materials

such as WO_{3-x}, $Cu_{2-x}S$, $Cu_{2-x}Se$, and ITO NPs have plasmonic peaks in the near-infrared region while the conventional metal NPs have the LSPRs typically in the visible region. In addition, the plasmonic effect of the non-metal nanomaterials arises from the collective oscillations of holes produced by introducing a high vacancy concentration, while the plasmonic effect in the metal nanomaterials results from the collective oscillations of electrons. Moreover, in addition to the size, shape, and environment of non-metal nanomaterials, the hole concentration can also affect the plasmonic effect in non-metal nanomaterials and can be tuned. In contrast, the electron concentration is hard to modify for metal nanomaterials. To date, few studies on the hybrid nanostructures of non-metal NPs/2D materials have been published. Integrating non-metal nanomaterials with 2D materials has several advantages. Plasmonic coupling is likely because the active plasmonic region of non-metal nanomaterials at infrared wavelengths is closer to the plasmonic region of graphene. By varying the stoichiometry of non-metal nanomaterials, the optical effects in the hybrid nanostructures of non-metal/2D materials can be efficiently tailored, thus satisfying the requirements of practical applications. Furthermore, if plasmonic metal nanomaterials, plasmonic non-metal nanomaterials, and 2D materials are combined, interesting optical coupling effects, new physical phenomena, and high-performance applications can be produced in the future.

Finally, other new 2D materials, such as phosphorene, g-C_3N_4, silicene, and germanene, could also be integrated with plasmonic nanomaterials.[28,30,323] In this review, the 2D materials discussed in the hybrid systems mainly include graphene, MoS_2, and h-BN, for which significant research progress has been achieved. With the development of new 2D nanomaterials such as phosphorene, silicene, and germanene, which have distinct properties from those of graphene, it would be interesting to exploit the integration of these materials with plasmonic nanomaterials as hybrid systems for optical-related applications.

Abbreviations

2D	Two-dimensional
3D	Three-dimensional
AA	Ascorbic acid
Ab	Antibody
aG	Antigen
anti-CT	Anti-cholera toxin
APTES	3-Aminopropyltriethoxysilane
b-CT	Biotinylated cholera toxin
BHJ	Bulk heterojunction
BN	Boron nitride
BSA	Bovine serum albumin
CB	Conduction band
CFG	Crack-fill graphene
CFP-10	Culture filtrate protein 10
CNP	Charge neutral point
CTAB	Cetyltrimethyl ammonium bromide
CTP	Charge-transfer plasmon
CV	Crystal violet
CVD	Chemical vapor deposition
DNA	Deoxyribonucleic acid
$\|E\|^2$	Square modulus of electric field
EBL	Electron beam lithography
EF	Enhancement factor
FET	Field effect transistor
FIB	Focused ion beam
FTO	Fluorine doped tin oxide
G	Graphene
GO	Graphene oxide
h-BN	Hexagonal boron nitride
HDA	1-Hexadecylamine
HTL	Hole transport layer
IPA	Isopropanol
IPCE	Incident photon-to-electron conversion efficiency
ITO	Indium tin oxide
J–V	Photocurrent–voltage
LED	Light emitting diodes
LG	Layer graphene
LOD	Limit of detection
LSP	Localized surface plasmons
LSPR	Localized surface plasmon resonance
MoS_2	Molybdenum sulfide
N	Number of layers
NMP	*n*-Methyl-2-pyrrolidone
NPs	Nanoparticles
NSL	Nanosphere lithography
NTA	Nitrilotriacetic acid
ODA	Octadecylamine
OLA	Oleylamine
OSCs	Organic solar cells
P	Polarizability
P3HT	Poly(3-hexylthiophene)
$PC_{71}BM$	[6,6]-Phenyl-C_{71} butyric acid methyl ester
$PC_{61}BM$	[6,6]-phenyl-C_{61} butyric acid methyl ester
PCE	Power conversion efficiency
PDA	Polydopamine
PDDA	Poly(diallyldimethylammonium)
PDs	Photodetectors
PEC	Photoelectrochemical cell
PEDOT:PSS	Poly(3,4-ethylenedioxythiophene): poly(styrenesulfonate)
PL	Photoluminescence
PMMA	Poly(methylmethacrylate)
PTB7	Poly[[4,8-bis[(2-ethylhexyl)oxy]benzo[1,2-*b*:4,5-*b*′]-dithiophene-2,6-diyl][3-fluoro-2-[(2-ethylheyl)-carbonyl]-thieno[3,4-*b*]thiophenediyl]]
PVP	Polyvinyl pyrrolidone
PVs	Photovoltaic cells
QDs	Quantum dots
RGO	Reduced graphene oxide
RhB	Rhodamine B
SERS	Surface-enhanced Raman scattering
SLG	Single layer graphene

SNOM	Scanning near-field optical microscope
SPP	Surface plasmon polaritons
TB	Tuberculosis
TCNQ	7,7,8,8-Tetracyanoquinodimethane
THz	Terahertz
TMDs	Transition metal dichalcogenides
UV	Ultraviolet
VB	Valence band

Acknowledgements

This research is supported by the National Natural Science Foundation of China (51221001, 51472204, 51571166, 51221061, and 61505167) and the Program of Introducing Talents of Discipline to Universities (B08040). We also thank the support of Key Scientific and Technological Team from Shaanxi Province (No. 2015KCT-12).

References

1 D. Li and R. B. Kaner, *Science*, 2008, **320**, 1170–1171.
2 F. Bonaccorso, Z. Sun, T. Hasan and A. C. Ferrari, *Nat. Photonics*, 2010, **4**, 611–622.
3 A. N. Grigorenko, M. Polini and K. S. Novoselov, *Nat. Photonics*, 2012, **6**, 749–758.
4 Q. H. Wang, K. Kalantar-Zadeh, A. Kis, J. N. Coleman and M. S. Strano, *Nat. Nanotechnol.*, 2012, **7**, 699–712.
5 O. V. Yazyev and Y. P. Chen, *Nat. Nanotechnol.*, 2014, **9**, 755–767.
6 G. Fiori, F. Bonaccorso, G. Iannaccone, T. Palacios, D. Neumaier, A. Seabaugh, S. K. Banerjee and L. Colombo, *Nat. Nanotechnol.*, 2014, **9**, 768–779.
7 F. Schwierz, *Proc. IEEE*, 2013, **101**, 1567–1584.
8 J. M. Yoo, J. H. Kang and B. H. Hong, *Chem. Soc. Rev.*, 2015, **44**, 4835–4852.
9 H. Y. Mao, S. Laurent, W. Chen, O. Akhavan, M. Imani, A. A. Ashkarran and M. Mahmoudi, *Chem. Rev.*, 2013, **113**, 3407–3424.
10 Y. Zhu, S. Murali, W. Cai, X. Li, J. W. Suk, J. R. Potts and R. S. Ruoff, *Adv. Mater.*, 2010, **22**, 3906–3924.
11 H. P. Cong, J. F. Chen and S. H. Yu, *Chem. Soc. Rev.*, 2014, **43**, 7295–7325.
12 J. H. Li, L. Y. Niu, Z. J. Zheng and F. Yan, *Adv. Mater.*, 2014, **26**, 5239–5273.
13 Y. X. Liu, X. C. Dong and P. Chen, *Chem. Soc. Rev.*, 2012, **41**, 2283–2307.
14 M. M. Liu, R. Z. Zhang and W. Chen, *Chem. Rev.*, 2014, **114**, 5117–5160.
15 X. Huang, Z. Y. Zeng, Z. X. Fan, J. Q. Liu and H. Zhang, *Adv. Mater.*, 2012, **24**, 5979–6004.
16 S. J. Guo and S. J. Dong, *Chem. Soc. Rev.*, 2011, **40**, 2644–2672.
17 M. S. Xu, T. Liang, M. M. Shi and H. Z. Chen, *Chem. Rev.*, 2013, **113**, 3766–3798.
18 Q. Ji, Y. Zhang, Y. Zhang and Z. Liu, *Chem. Soc. Rev.*, 2015, **44**, 2587–2602.
19 H. Wang, H. Yuan, S. Sae Hong, Y. Li and Y. Cui, *Chem. Soc. Rev.*, 2015, **44**, 2664–2680.
20 G. B. Liu, D. Xiao, Y. Yao, X. Xu and W. Yao, *Chem. Soc. Rev.*, 2015, **44**, 2643–2663.
21 Y. Sun, S. Gao, F. Lei and Y. Xie, *Chem. Soc. Rev.*, 2015, **44**, 623–636.
22 Y. Shi, H. Li and L. J. Li, *Chem. Soc. Rev.*, 2015, **44**, 2744–2756.
23 H. Zeng and X. Cui, *Chem. Soc. Rev.*, 2015, **44**, 2629–2642.
24 X. Zhang, X. F. Qiao, W. Shi, J. B. Wu, D. S. Jiang and P. H. Tan, *Chem. Soc. Rev.*, 2015, **44**, 2757–2785.
25 X. Huang, Z. Zeng and H. Zhang, *Chem. Soc. Rev.*, 2013, **42**, 1934–1946.
26 Y. Chen, C. Tan, H. Zhang and L. Wang, *Chem. Soc. Rev.*, 2015, **44**, 2681–2701.
27 M. M. Benameur, B. Radisavljevic, J. S. Héron, S. Sahoo, H. Berger and A. Kis, *Nanotechnology*, 2011, **22**, 125706.
28 D. Jose and A. Datta, *Acc. Chem. Res.*, 2014, **47**, 593–602.
29 H. Liu, Y. Du, Y. Deng and P. D. Ye, *Chem. Soc. Rev.*, 2015, **44**, 2732–2743.
30 A. O'Hare, F. V. Kusmartsev and K. I. Kugel, *Nano Lett.*, 2012, **12**, 1045–1052.
31 L. Dou, A. B. Wong, Y. Yu, M. Lai, N. Kornienko, S. W. Eaton, A. Fu, C. G. Bischak, J. Ma, T. Ding, N. S. Ginsberg, L. W. Wang, A. P. Alivisatos and P. D. Yang, *Science*, 2015, **349**, 1518–1521.
32 A. Favron, E. Gaufres, F. Fossard, A. L. Phaneuf-L'Heureux, N. Y. Tang, P. L. Levesque, A. Loiseau, R. Leonelli, S. Francoeur and R. Martel, *Nat. Mater.*, 2015, **14**, 826–832.
33 A. J. Mannix, X. F. Zhou, B. Kiraly, J. D. Wood, D. Alducin, B. D. Myers, X. Liu, B. L. Fisher, U. Santiago, J. R. Guest, M. J. Yacaman, A. Ponce, A. R. Oganov, M. C. Hersam and N. P. Guisinger, *Science*, 2015, **350**, 1513–1516.
34 S. Z. Butler, S. M. Hollen, L. Cao, Y. Cui, J. A. Gupta, H. R. Gutiérrez, T. F. Heinz, S. S. Hong, J. Huang, A. F. Ismach, E. J. Halperin, M. Kuno, V. V. Plashnitsa, R. D. Robinson, R. S. Ruoff, S. Salahuddin, J. Shan, L. Shi, M. G. Spencer, M. Terrones, W. Windl and J. E. Goldberger, *ACS Nano*, 2013, **7**, 2898–2926.
35 R. F. Service, *Science*, 2015, **348**, 490–492.
36 K. T. Nguyena and Y. Zhao, *Nanoscale*, 2014, **6**, 6245–6266.
37 G. Modugno, C. M. Moyon, M. Prato and A. Bianco, *Br. J. Pharmacol.*, 2015, **172**, 975–991.
38 P. T. Yin, S. Shah, M. Chhowalla and K. B. Lee, *Chem. Rev.*, 2015, **115**, 2483–2531.
39 X. Huang, C. Tan, Z. Yin and H. Zhang, *Adv. Mater.*, 2014, **26**, 2185–2204.
40 F. Koppens, T. Mueller, P. Avouris, A. Ferrari, M. Vitiello and M. Polini, *Nat. Nanotechnol.*, 2014, **9**, 780–783.
41 D. Zhang, L. Gan, Y. Cao, Q. Wang, L. Qi and X. Guo, *Adv. Mater.*, 2012, **24**, 2715–2720.
42 C. O. Kim, S. Kim, D. H. Shin, S. S. Kang, J. M. Kim, C. W. Jang, S. S. Joo, J. S. Lee, J. H. Kim, S. H. Choi and E. Hwang, *Nat. Commun.*, 2014, **5**, 3249–3255.

43 C. Wang and D. Astruc, *Chem. Soc. Rev.*, 2014, **43**, 7188–7216.
44 L. Vigderman, B. P. Khanal and E. R. Zubarev, *Adv. Mater.*, 2012, **24**, 4811–4841.
45 M. Rycenga, C. M. Cobley, J. Zeng, W. Li, C. H. Moran, Q. Zhang, D. Qin and Y. Xia, *Chem. Rev.*, 2011, **111**, 3669–3712.
46 N. Li, P. Zhao and D. Astruc, *Angew. Chem., Int. Ed.*, 2014, **53**, 1756–1789.
47 J. Li, C. Yang, J. Li, Z. Li, S. Zu, S. Song, H. Zhao, F. Lin and X. Zhu, *Plasmonics*, 2014, **9**, 879–886.
48 A. Klinkova, R. M. Choueiri and E. Kumacheva, *Chem. Soc. Rev.*, 2014, **43**, 3976–3991.
49 X. Huang, S. Neretina and M. A. El-Sayed, *Adv. Mater.*, 2009, **21**, 4880–4910.
50 L. Guerrini and D. Graham, *Chem. Soc. Rev.*, 2012, **41**, 7085–7107.
51 M. Grzelczak and L. M. Liz-Marzan, *Chem. Soc. Rev.*, 2014, **43**, 2089–2097.
52 Z. Fang and X. Zhu, *Adv. Mater.*, 2013, **25**, 3840–3856.
53 D. J. D. Aberasturi, A. B. Serrano-Montes and L. M. Liz-Marzán, *Adv. Opt. Mater.*, 2015, **3**, 602–617.
54 H. Chen, L. Shao, Q. Li and J. Wang, *Chem. Soc. Rev.*, 2013, **42**, 2679–2724.
55 M. L. Brongersma, *Faraday Discuss.*, 2015, **178**, 9–36.
56 A. Bonakdar and H. Mohseni, *Nanoscale*, 2014, **6**, 10961–10974.
57 P. Berini, *Laser Photonics Rev.*, 2014, **8**, 197–220.
58 G. Baffou and R. Quidant, *Chem. Soc. Rev.*, 2014, **43**, 3898–3907.
59 A. Comin and L. Manna, *Chem. Soc. Rev.*, 2014, **43**, 3957–3975.
60 J. Zhang, P. Wang, J. Sun and Y. Jin, *ACS Appl. Mater. Interfaces*, 2014, **6**, 19905–19913.
61 D. O. Sigle, L. Zhang, S. Ithurria, B. Dubertret and J. J. Baumberg, *J. Phys. Chem. Lett.*, 2015, **6**, 1099–1103.
62 C. Clavero, *Nat. Photonics*, 2014, **8**, 95–103.
63 X. Li, W. C. H. Choy, X. Ren, D. Zhang and H. Lu, *Adv. Funct. Mater.*, 2014, **24**, 3114–3122.
64 S. Jang, E. Hwang, Y. Lee, S. Lee and J. H. Cho, *Nano Lett.*, 2015, **15**, 2542–2547.
65 P. T. Yin, T. H. Kim, J. W. Choi and K. B. Lee, *Phys. Chem. Chem. Phys.*, 2013, **15**, 12785–12799.
66 C. Tan, X. Huang and H. Zhang, *Mater. Today*, 2013, **16**, 29–36.
67 X. Li, J. Li, X. Zhou, Y. Ma, Z. Zheng, X. Duan and Y. Qu, *Carbon*, 2014, **66**, 713–719.
68 J. Huang, L. Zhang, B. Chen, N. Ji, F. Chen, Y. Zhang and Z. Zhang, *Nanoscale*, 2010, **2**, 2733–2738.
69 Q. Chen, L. Zhang and G. Chen, *Anal. Chem.*, 2012, **84**, 171–178.
70 R. Jiang, B. Li, C. Fang and J. Wang, *Adv. Mater.*, 2014, **26**, 5274–5309.
71 A. Sobhani, A. Lauchner, S. Najmaei, C. Ayala-Orozco, F. Wen, J. Lou and N. J. Halas, *Appl. Phys. Lett.*, 2014, **104**, 031112.
72 S. W. Zeng, D. Baillargeat, H. P. Ho and K. T. Yong, *Chem. Soc. Rev.*, 2014, **43**, 3426–3452.
73 A. Pakdel, Y. Bando and D. Golberg, *Chem. Soc. Rev.*, 2014, **43**, 934–959.
74 W. Ren, Y. Fang and E. Wang, *ACS Nano*, 2011, **5**, 6425–6433.
75 G. Lu, H. Li, C. Liusman, Z. Yin, S. Wu and H. Zhang, *Chem. Sci.*, 2011, **2**, 1817–1821.
76 M. Iliut, C. Leordean, V. Canpean, C. Teodorescub and S. Astilean, *J. Mater. Chem. C*, 2013, **1**, 4094–4104.
77 Y. Zhao, X. Li, Y. Du, G. Chen, Y. Qu, J. Jiang and Y. Zhu, *Nanoscale*, 2014, **6**, 11112–11120.
78 Y. Zhao, G. Chen, Y. Du, J. Xu, S. Wu, Y. Qu and Y. Zhu, *Nanoscale*, 2014, **6**, 13754–13760.
79 T. W. Lin, H. Y. Wu, T. T. Tasi, Y. H. Lai and H. H. Shen, *Phys. Chem. Chem. Phys.*, 2015, **17**, 18443–18448.
80 Z. Xiong, L. L. Zhang, J. Ma and X. S. Zhao, *Chem. Commun.*, 2010, **46**, 6099–6101.
81 X. Yang, W. Liu, M. Xiong, Y. Zhang, T. Liang, J. Yang, M. Xu, J. Ye and H. Chen, *J. Mater. Chem. A*, 2014, **2**, 14798–14806.
82 S. U. Yu, B. Park, Y. Cho, S. Hyun, J. K. Kim and K. S. Kim, *ACS Nano*, 2014, **8**, 8662–8668.
83 Z. Luo, L. A. Somers, Y. Dan, T. Ly, N. J. Kybert, E. J. Mele and A. T. Johnson, *Nano Lett.*, 2010, **10**, 777–781.
84 H. Q. Zhou, C. Y. Qiu, Z. Liu, H. C. Yang, L. L. Hu, J. Liu, H. F. Yang, C. Z. Gu and L. F. Sun, *J. Am. Chem. Soc.*, 2010, **132**, 944–946.
85 H. Zhou, C. Qiu, F. Yu, H. Yang, M. Chen, L. Hu and L. Sun, *J. Phys. Chem. C*, 2011, **115**, 11348–11354.
86 R. Zan, U. Bangert, Q. Ramasse and K. S. Novoselov, *Small*, 2011, **7**, 2868–2872.
87 P. A. Pandey, G. R. Bell, J. P. Rourke, B. J. Hickey and N. R. Wilson, *Small*, 2011, **7**, 3202–3210.
88 Y. Zhang, G. Wang, X. Hu and R. Xing, *J. Solid State Chem.*, 2005, **178**, 1609–1613.
89 X. Li, X. Ren, Y. Zhang, W. C. Choy and B. Wei, *Nanoscale*, 2015, **7**, 11291–11299.
90 C. Gong, C. Huang, J. Mille, R. S. Ruoff, R. M. Wallace, X. Xu and Y. J. Chabal, *ACS Nano*, 2013, **7**, 11350–11357.
91 L. Yang, D. Zhong, J. Zhang, Z. Yan, S. Ge, P. Du, J. Jiang, D. Sun, X. Wu, Z. Fan, S. Dayeh and B. Xiang, *ACS Nano*, 2014, **8**, 6979–6985.
92 X. Z. Tang, Z. Cao, H. B. Zhang, J. Liu and Z. Z. Yu, *Chem. Commun.*, 2011, **47**, 3084–3086.
93 P. Xu, H. Yu and X. Li, *Chem. Commun.*, 2012, **48**, 10784–10786.
94 C. Xu, X. Wang and J. Zhu, *J. Phys. Chem. C*, 2008, **112**, 19841–19845.
95 Z. Cheng, B. He and L. Zhou, *J. Mater. Chem. A*, 2014, **3**, 1042–1048.
96 Y. Chen, Y. Li, D. Sun, D. Tian, J. Zhang and J. J. Zhu, *J. Mater. Chem.*, 2011, **21**, 7604–7611.
97 Y. Zhou, J. Yang, T. He, H. Shi, X. Cheng and Y. Lu, *Small*, 2013, **9**, 3445–3454.
98 T. T. Baby and S. Ramaprabhu, *J. Mater. Chem.*, 2011, **21**, 9702–9709.

99 P. Liu, Y. Huang and L. Wang, *Synth. Met.*, 2013, **167**, 25–30.
100 S. H. Kim, G. H. Jeong, D. Choi, S. Yoon, H. B. Jeon, S. M. Lee and S. W. Kim, *J. Colloid Interface Sci.*, 2013, **389**, 85–90.
101 Y. K. Kim, H. K. Na, Y. W. Lee, H. Jang, S. W. Han and D. H. Min, *Chem. Commun.*, 2010, **46**, 3185–3187.
102 C. Xue, M. Gao, Y. Xue, L. Zhu, L. Dai, A. Urbas and Q. Li, *J. Phys. Chem. C*, 2014, **118**, 15332–15338.
103 R. Muszynski, B. Seger and P. V. Kamat, *J. Phys. Chem. C*, 2008, **112**, 5263–5266.
104 E. S. Orth, J. E. S. Fonsaca, S. H. Domingues, H. Mehl, M. M. Oliveira and A. J. G. Zarbin, *Carbon*, 2013, **61**, 543–550.
105 B. Lebeau and P. Innocenzi, *Chem. Soc. Rev.*, 2011, **40**, 886–906.
106 Z. Zhang, J. Zhang, B. Zhang and J. Tang, *Nanoscale*, 2013, **5**, 118–123.
107 F. A. He, J. T. Fan, F. Song, L. M. Zhang and H. L. W. Chan, *Nanoscale*, 2011, **3**, 1182–1188.
108 J. Liu, Y. Li, Y. Li, J. Li and Z. Deng, *J. Mater. Chem.*, 2010, **20**, 900–906.
109 E. K. Jeon, E. Seo, E. Lee, W. Lee, M. K. Um and B. S. Kim, *Chem. Commun.*, 2013, **49**, 3392–3394.
110 C. Song, D. Wu, F. Zhang, P. Liu, Q. Lu and X. Feng, *Chem. Commun.*, 2012, **48**, 2119–2121.
111 S. Vijay Kumar, N. M. Huang, H. N. Lim, A. R. Marlinda, I. Harrison and C. H. Chia, *Chem. Eng. J.*, 2013, **219**, 217–224.
112 J. Park, H. S. Jayawardena, X. Chen, K. W. Jayawardana, M. Sundhoro, E. Ada and M. Yan, *Chem. Commun.*, 2015, **51**, 2882–2885.
113 J. Liu, S. Fu, B. Yuan, Y. Li and Z. Deng, *J. Am. Chem. Soc.*, 2010, **132**, 7279–7281.
114 P. S. Toth, M. Velický, Q. M. Ramasse, D. M. Kepaptsoglou and R. A. W. Dryfe, *Adv. Funct. Mater.*, 2015, **25**, 2899–2909.
115 W. Wang, J. Gu, W. Hua, X. Jia and K. Xi, *Chem. Commun.*, 2014, **50**, 8889–8891.
116 H. Pan, S. Low, N. Weerasuriya and Y. Shon, *ACS Appl. Mater. Interfaces*, 2015, **7**, 3406–3413.
117 Y. H. Lee, L. Polavarapu, N. Gao, P. Yuan and Q. H. Xu, *Langmuir*, 2012, **28**, 321–326.
118 K. Jasuja and V. Berry, *ACS Nano*, 2009, **3**, 2358–2366.
119 X. Huang, S. Li, S. Wu, Y. Huang, F. Boey, C. L. Gan and H. Zhang, *Adv. Mater.*, 2012, **24**, 979–983.
120 D. Kiriya, Y. Zhou, C. Nelson, M. Hettick, S. R. Madhvapathy, K. Chen, P. Zhao, M. Tosun, A. M. Minor, D. C. Chrzan and A. Javey, *Adv. Funct. Mater.*, 2015, **25**, 6257–6264.
121 J. Lu, J. H. Lu, H. Liu, B. Liu, L. Gong, E. S. Tok, K. P. Loh and C. H. Sow, *Small*, 2015, **11**, 1792–1800.
122 J. F. Blandez, A. Primo, A. M. Asiri, M. Alvaro and H. Garcia, *Angew. Chem., Int. Ed.*, 2014, **53**, 12581–12586.
123 Y. Gao, X. Chen, J. Zhang, H. Asakura, T. Tanaka, K. Teramura, D. Ma and N. Yan, *Adv. Mater.*, 2015, **27**, 4688–4694.
124 T. S. Sreeprasad, P. Nguyen, N. Kim and V. Berry, *Nano Lett.*, 2013, **13**, 4434–4441.
125 X. Huang, Z. Zeng, S. Bao, M. Wang, X. Qi, Z. Fan and H. Zhang, *Nat. Commun.*, 2013, **4**, 1444–1451.
126 Y. Lin, C. E. Bunker, K. A. S. Fernando and J. W. Connell, *ACS Appl. Mater. Interfaces*, 2012, **4**, 1110–1117.
127 W. Wang, J. Cui, W. Fan, Z. Feng, X. Ma and W. Jiang, *Mater. Lett.*, 2012, **84**, 120–123.
128 L. Guardia, S. Villar-Rodil, J. I. Paredes, R. Rozada, A. Martínez-Alonso and J. M. D. Tascón, *Carbon*, 2012, **50**, 1014–1024.
129 S. Moussa, G. Atkinson, M. SamyEl-Shall, A. Shehata, K. M. AbouZeid and M. B. Mohamed, *J. Mater. Chem.*, 2011, **21**, 9608–9619.
130 S. Su, C. Zhang, L. Yuwen, J. Chao, X. Zuo, X. Liu, C. Song, C. Fan and L. Wang, *ACS Appl. Mater. Interfaces*, 2014, **6**, 18735–18741.
131 Y. Kim and D. Min, *Langmuir*, 2012, **28**, 4453–4458.
132 G. H. Jeong, S. H. Kim, M. Kim, D. Choi, J. H. Lee, J. H. Kim and S. W. Kim, *Chem. Commun.*, 2011, **47**, 12236–12238.
133 Y. Kim, W. Song, S. i. Lee, S. Youb Lee, M.-J. Cha, D. Sung Jung and C. Y. Park, *Appl. Phys. Lett.*, 2013, **102**, 223116.
134 J. G. Radich and P. V. Kamat, *ACS Nano*, 2013, **7**, 5546–5557.
135 S. A. You, O. S. Kwon and J. Jang, *J. Mater. Chem.*, 2012, **22**, 17805–17812.
136 S. S. J. Aravind, V. Eswaraiah and S. Ramaprabhu, *J. Mater. Chem.*, 2011, **21**, 17094–17097.
137 I. V. Lightcap, S. Murphy, T. Schumer and P. V. Kamat, *J. Phys. Chem. Lett.*, 2012, **3**, 1453–1458.
138 T. Daeneke, B. J. Carey, A. F. Chrimes, J. Z. Ou, D. W. M. Lau, B. C. Gibson, M. Bhaskaran and K. Kalantar-Zadeh, *J. Mater. Chem. C*, 2015, **3**, 4771–4778.
139 H. Zhao, J. Song, X. Song, Z. Yan and H. Zeng, *J. Mater. Chem. A*, 2015, **3**, 6679–6684.
140 G. Xie, M. Forslund and J. Pan, *ACS Appl. Mater. Interfaces*, 2014, **6**, 7444–7455.
141 C. Liu, K. Wang, S. Luo, Y. Tang and L. Chen, *Small*, 2011, **7**, 1203–1206.
142 E. Nossol, A. B. S. Nossol, S. X. Guo, J. Zhang, X. Y. Fang, A. J. G. Zarbin and A. M. Bond, *J. Mater. Chem. C*, 2014, **2**, 870–878.
143 C. L. Pavithra, B. V. Sarada, K. V. Rajulapati, T. N. Rao and G. Sundararajan, *Sci. Rep.*, 2014, **4**, 4049–4055.
144 S. Su, H. Sun, F. Xu, L. Yuwen, C. Fan and L. Wang, *Microchim. Acta*, 2014, **181**, 1497–1503.
145 J. Yang, C. Zang, L. Sun, N. Zhao and X. Cheng, *Mater. Chem. Phys.*, 2011, **129**, 270–274.
146 Y. Qin, J. Li, Y. Kong, X. Li, Y. Tao, S. Li and Y. Wang, *Nanoscale*, 2014, **6**, 1281–1285.
147 J. Huang, Z. Dong, Y. Li, J. Li, W. Tang, H. Yang, J. Wang, Y. Bao, J. Jin and R. Li, *Mater. Res. Bull.*, 2013, **48**, 4544–4547.
148 Z. Tang, S. Shen, J. Zhuang and X. Wang, *Angew. Chem., Int. Ed.*, 2010, **49**, 4603–4607.
149 B. Govinda Rao, H. S. S. R. Matte and C. N. R. Rao, *J. Cluster Sci.*, 2012, **23**, 929–937.
150 S. Liu, J. Tian, L. Wang and X. Sun, *J. Nanopart. Res.*, 2011, **13**, 4539–4548.

151 G. Gao, A. Mathkar, E. P. Martins, D. S. Galvão, D. Gao, P. A. D. S. Autreto, C. Sun, L. Cai and P. M. Ajayan, *J. Mater. Chem. A*, 2014, **2**, 3148–3154.
152 K. Vinodgopal, B. Neppolian, F. Grieser and P. V. Kamat, *J. Phys. Chem. Lett.*, 2010, **1**, 1987–1993.
153 L. Pan, Y. T. Liu, X. M. Xie and X. D. Zhu, *Chem. – Asian J.*, 2014, **9**, 1519–1524.
154 G. H. Yang, J. J. Shi, S. Wang, W. W. Xiong, L. P. Jiang, C. Burda and J. J. Zhu, *Chem. Commun.*, 2013, **49**, 10757–10759.
155 S. K. Singhal, V. Kumar, K. Stalin, A. Choudhary, S. Teotia, G. B. Reddy, R. B. Mathur, S. P. Singh and R. Pasricha, *Part. Part. Syst. Charact.*, 2013, **30**, 445–452.
156 S. Wang, Y. Zhang, H. L. Ma, Q. Zhang, W. Xu, J. Peng, J. Li, Z. Z. Yu and M. Zhai, *Carbon*, 2013, **55**, 245–252.
157 I. Shown, H. Hsu, Y. Chang, C. Wu and L. Chen, *Nano Lett.*, 2014, **14**, 6097–6103.
158 X. Wang, G. Meng, C. Zhu, Z. Huang, Y. Qian, K. Sun and X. Zhu, *Adv. Funct. Mater.*, 2013, **23**, 5771–5777.
159 W. Xu, J. Xiao, Y. Chen, Y. Chen, X. Ling and J. Zhang, *Adv. Mater.*, 2013, **25**, 928–933.
160 B. Lee, J. Park, G. H. Han, H. S. Ee, C. H. Naylor, W. Liu, A. T. Johnson and R. Agarwal, *Nano Lett.*, 2015, **15**, 3646–3653.
161 T. J. Echtermeyer, L. Britnell, P. K. Jasnos, A. Lombardo, R. V. Gorbachev, A. N. Grigorenko, A. K. Geim, A. C. Ferrari and K. S. Novoselov, *Nat. Commun.*, 2011, **2**, 458–462.
162 Z. Fang, Y. Wang, P. M. Ajayan and N. J. Halas, *ACS Nano*, 2012, **6**, 10222–10228.
163 Y. Liu, R. Cheng, L. Liao, H. Zhou, J. Bai, G. Liu, L. Liu, Y. Huang and X. Duan, *Nat. Commun.*, 2011, **2**, 579–585.
164 S. H. Mousavi, I. Kholmanov, K. B. Alici, D. Purtseladze, N. Arju, K. Tatar, D. Y. Fozdar, J. W. Suk, Y. Hao, A. B. Khanikaev, R. S. Ruoff and G. Shvets, *Nano Lett.*, 2013, **13**, 1111–1117.
165 H. R. Park, S. Namgung, X. Chen, N. C. Lindquist, V. Giannini, Y. Francescato, S. A. Maier and S. H. Oh, *Adv. Opt. Mater.*, 2015, **3**, 667–673.
166 S. Heeg, R. Fernandez-Garcia, A. Oikonomou, F. Schedin, R. Narula, S. A. Maier, A. Vijayaraghavan and S. Reich, *Nano Lett.*, 2013, **13**, 301–308.
167 X. Zhu, L. Shi, M. Schmidt, A. Bosisen, O. Hansen, J. Zi, S. Xiao and N. Mortensen, *Nano Lett.*, 2013, **13**, 4690–4696.
168 B. Zhao, J. M. Zhao and Z. M. Zhang, *Appl. Phys. Lett.*, 2014, **105**, 031905.
169 N. K. Emani, T. F. Chung, X. Ni, A. V. Kildishev, Y. P. Chen and A. Boltasseva, *Nano Lett.*, 2012, **12**, 5202–5206.
170 Y. Yao, R. Shankar, P. Rauter, Y. Song, J. Kong, M. Loncar and F. Capasso, *Nano Lett.*, 2014, **14**, 3749–3754.
171 U. J. Kim, S. Yoo, Y. Park, M. Shin, J. Kim, H. Jeong, C. W. Baik, Y. G. Roh, J. Lee, K. Im, H. Son, S. Hwang, C. W. Lee and S. Park, *ACS Photonics*, 2015, **2**, 506–514.
172 F. Valmorra, G. Scalari, C. Maissen, W. Fu, C. Schonenberger, J. W. Choi, H. G. Park, M. Beck and J. Faist, *Nano Lett.*, 2013, **13**, 3193–3198.
173 Y. Yao, R. Shankar, M. A. Kats, Y. Song, J. Kong, M. Loncar and F. Capasso, *Nano Lett.*, 2014, **14**, 6526–6532.
174 N. K. Emani, T. F. Chung, A. V. Kildishev, V. M. Shalaev, Y. P. Chen and A. Boltasseva, *Nano Lett.*, 2014, **14**, 78–82.
175 S. Najmaei, A. Mlayah, A. Arbouet, C. Girard, J. Leotin and J. Jou, *ACS Nano*, 2014, **8**, 12682–12689.
176 Y. Yao, M. A. Kats, P. Genevet, N. Yu, Y. Song, J. Kong and F. Capasso, *Nano Lett.*, 2013, **13**, 1257–1264.
177 S. Butun, S. Tongay and K. Aydin, *Nano Lett.*, 2015, **15**, 2700–2704.
178 Z. Fang, Z. Liu, Y. Wang, P. M. Ajayan, P. Nordlander and N. J. Halas, *Nano Lett.*, 2012, **12**, 3808–3813.
179 S. Zeng, S. Hu, J. Xia, T. Anderson, X. Q. Dinh, X. M. Meng, P. Coquet and K. T. Yong, *Sens. Actuators, B*, 2015, **207**, 801–810.
180 Y. Cai, J. Zhu and Q. H. Liu, *Appl. Phys. Lett.*, 2015, **106**, 043105.
181 T. Echtermeyer, P. Nene, M. Trushin, R. Gorbachev, A. Eiden, S. Milana, Z. Sun, J. Schliemann, E. Lidorikis, K. Novoselov and A. Ferrari, *Nano Lett.*, 2014, **14**, 3733–3742.
182 D. Paria, K. Roy, H. J. Singh, S. Kumar, S. Raghavan, A. Ghosh and A. Ghosh, *Adv. Mater.*, 2015, **27**, 1751–1758.
183 A. M. Gilbertson, Y. Francescato, T. Roschuk, V. Shautsova, Y. Chen, T. P. Sidiropoulos, M. Hong, V. Giannini, S. A. Maier, L. F. Cohen and R. F. Oulton, *Nano Lett.*, 2015, **15**, 3458–3464.
184 H. Wang, H. Feng and J. Li, *Small*, 2014, **10**, 2165–2181.
185 T. K. Sau, A. L. Rogach, F. Jackel, T. A. Klar and J. Feldmann, *Adv. Mater.*, 2010, **22**, 1805–1825.
186 V. Giannini, A. I. Fernandez-Dominguez, S. C. Heck and S. A. Maier, *Chem. Rev.*, 2011, **111**, 3888–3912.
187 D. Chen, H. Zhang, Y. Liu and J. Li, *Energy Environ. Sci.*, 2013, **6**, 1362–1387.
188 Z. Yin, J. Zhu, Q. He, X. Cao, C. Tan, H. Chen, Q. Yan and H. Zhang, *Adv. Energy Mater.*, 2014, **4**, 1300574.
189 H. A. Atwater and A. Polman, *Nat. Mater.*, 2010, **9**, 205–213.
190 X. Li, W. C. H. Choy, L. Huo, F. Xie, W. E. I. Sha, B. Ding, X. Guo, Y. Li, J. Hou, J. You and Y. Yang, *Adv. Mater.*, 2012, **24**, 3046–3052.
191 S. Wang, Y. Zhang, R. Zhang, H. Yu, H. Zhang and Q. Xiong, *Adv. Opt. Mater.*, 2015, **3**, 1342–1348.
192 A. Boltasseva and H. A. Atwater, *Science*, 2011, **331**, 290–291.
193 C. H. Chou and F. C. Chen, *Nanoscale*, 2014, **6**, 8444–8458.
194 C. F. Bohren and D. R. Human, *Absorption and Scattering of Light by Small Particles*, John Wiley & Sons, New York, 1983.
195 H. Liu, T. Liu, L. Zhang, L. Han, C. Gao and Y. Yin, *Adv. Funct. Mater.*, 2015, **25**, 5435–5443.
196 D. Liu, F. Zhou, C. Li, T. Zhang, H. Zhang, W. Cai and Y. Li, *Angew. Chem., Int. Ed.*, 2015, **54**, 9596–9600.
197 S. G. Park, C. Mun, M. Lee, T. Y. Jeon, H. S. Shim, Y. J. Lee, J. D. Kwon, C. S. Kim and D. H. Kim, *Adv. Mater.*, 2015, **27**, 4290–4295.
198 W. L. Barnes, A. Dereux and T. W. Ebbesen, *Nature*, 2003, **424**, 824–830.
199 P. Ginzburg, A. V. Krasavin and A. V. Zayats, *New J. Phys.*, 2013, **15**, 013031.

200 H. Raether, *Surface Plasmons on Smooth Surfaces*, Springer, Berlin Heidelberg, 1988.
201 S. A. Maier, *Plasmonics: Fundamentals and Applications*, Springer Science & Business Media, 2007.
202 J. Butet, P. Brevet and O. J. F. Martin, *ACS Nano*, 2015, **9**, 10545–10562.
203 N. Verellen, Y. Sonnefraud, H. Sobhani, F. Hao, V. V. Moshchalkov, P. V. Dorpe, P. Nordlander and S. A. Maier, *Nano Lett.*, 2009, **9**, 1663–1667.
204 L. Duempelmann, D. Casari, A. Luu-Dinh, B. Gallinet and L. Novotny, *ACS Nano*, 2015, **9**, 12383–12391.
205 V. E. Ferry, M. Hentschel and A. P. Alivisatos, *Nano Lett.*, 2015, **15**, 8336–8341.
206 H. Saito and N. Yamamoto, *Nano Lett.*, 2015, **15**, 5764–5769.
207 Z. Yan, Y. Bao, U. Manna, R. A. Shah and N. F. Scherer, *Nano Lett.*, 2014, **14**, 2436–2442.
208 C. E. Petoukhoff and D. M. O'Carroll, *Nat. Commun.*, 2015, **6**, 7899.
209 A. Moreau, C. Ciraci, J. J. Mock, R. T. Hill, Q. Wang, B. J. Wiley, A. Chilkoti and D. R. Smith, *Nature*, 2012, **492**, 86–89.
210 L. Lin, M. Zapata, M. Xiong, Z. Liu, S. Wang, H. Xu, A. G. Borisov, H. Gu, P. Nordlander, J. Aizpurua and J. Ye, *Nano Lett.*, 2015, **15**, 6419–6428.
211 T. Coenen, D. T. Schoen, S. A. Mann, S. R. Rodriguez, B. J. Brenny, A. Polman and M. L. Brongersma, *Nano Lett.*, 2015, **15**, 7666–7670.
212 H. Harutyunyan, A. B. Martinson, D. Rosenmann, L. K. Khorashad, L. V. Besteiro, A. O. Govorov and G. P. Wiederrecht, *Nat. Nanotechnol.*, 2015, **10**, 770–774.
213 Y. Salamin, W. Heni, C. Haffner, Y. Fedoryshyn, C. Hoessbacher, R. Bonjour, M. Zahner, D. Hillerkuss, P. Leuchtmann, D. L. Elder, L. R. Dalton, C. Hafner and J. Leuthold, *Nano Lett.*, 2015, **15**, 8342–8346.
214 J. H. Chen, C. Jang, S. Xiao, M. Ishigami and M. S. Fuhre, *Nat. Nanotechnol.*, 2008, **3**, 206–209.
215 Z. Liu, L. Ma, G. Shi, W. Zhou, Y. Gong, S. Lei, X. Yang, J. Zhang, J. Yu, K. P. Hackenberg, A. Babakhani, J. C. Idrobo, R. Vajtai, J. Lou and P. M. Ajayan, *Nat. Nanotechnol.*, 2013, **8**, 119–124.
216 X. Du, I. Skachko, A. Barker and E. Y. Andrei, *Nat. Nanotechnol.*, 2008, **3**, 491–495.
217 F. N. Xia, H. Yan, P. Avouris, T. Low, W. Zhu, M. Freitag, Y. Q. Wu, X. Li and F. Guinea, *Nat. Photonics*, 2013, **7**, 420.
218 F. Xia, T. Mueller, Y. M. Lin, A. Valdes-Garcia and P. Avouris, *Nat. Nanotechnol.*, 2009, **4**, 839–843.
219 J. Tong, M. Muthee, S. Y. Chen, S. K. Yngvesson and J. Yan, *Nano Lett.*, 2015, **15**, 5295–5301.
220 T. Zhao, S. Gong, M. Hu, R. Zhong, D. Liu, X. Chen, P. Zhang, X. Wang, C. Zhang, P. Wu and S. Liu, *Sci. Rep.*, 2015, **5**, 16059.
221 Z. Fei, M. D. Goldflam, J. S. Wu, S. Dai, M. Wagner, A. S. McLeod, M. K. Liu, K. W. Post, S. Zhu, G. C. Janssen, M. M. Fogler and D. N. Basov, *Nano Lett.*, 2015, **15**, 8271–8276.
222 K. Y. Yeung, J. Chee, H. Yoon, Y. Song, J. Kong and D. Ham, *Nano Lett.*, 2014, **14**, 2479–2484.
223 L. J. Wong, I. Kaminer, O. Ilic, J. D. Joannopoulos and M. Soljačić, *Nat. Photonics*, 2015, **10**, 46–52.
224 H. J. Shin, W. M. Choi, D. Choi, G. H. Han, S. M. Yoon, H. K. Park, S. W. Kim, Y. W. Jin, S. Y. Lee, J. M. Kim, J. Y. Choi and Y. H. Lee, *J. Am. Chem. Soc.*, 2011, **132**, 15603–15609.
225 B. Zhao and Z. M. Zhang, *ACS Photonics*, 2015, **2**, 1611–1618.
226 W. Gao, L. B. Alemany, L. Ci and P. M. Ajayan, *Nat. Chem.*, 2009, **1**, 403–408.
227 R. J. W. E. Lahaye, H. K. Jeong, C. Y. Park and Y. H. Lee, *Phys. Rev. B: Condens. Matter Mater. Phys.*, 2009, **79**, 125435.
228 T. F. Yeh, J. M. Syu, C. Cheng, T. H. Chang and H. Teng, *Adv. Funct. Mater.*, 2010, **20**, 2255–2262.
229 J. Liu, M. Durstock and L. Dai, *Energy Environ. Sci.*, 2014, **7**, 1297–1306.
230 J. H. Jung, D. S. Cheon, F. Liu, K. B. Lee and T. S. Seo, *Angew. Chem., Int. Ed.*, 2010, **49**, 5708–5711.
231 K. Liu, J. J. Zhang, C. Wang and J. J. Zhu, *Biosens. Bioelectron.*, 2011, **26**, 3627–3632.
232 S. Mao, G. Lu, K. Yu, Z. Bo and J. Chen, *Adv. Mater.*, 2010, **22**, 3521–3526.
233 S. Chen, X. Hai, X. W. Chen and J. H. Wang, *Anal. Chem.*, 2014, **86**, 6689–6694.
234 K. Chen, G. Lu, J. Chang, S. Mao, K. Yu, S. Cui and J. Chen, *Anal. Chem.*, 2012, **84**, 4057–4062.
235 D. Yang, L. Zhou, W. Yu, J. Zhang and C. Li, *Adv. Energy Mater.*, 2014, **4**, 1400591.
236 Y. Chen, W. C. Lin, J. Liu and L. Dai, *Nano Lett.*, 2014, **14**, 1467–1471.
237 K. Kang, S. Xie, L. Huang, Y. Han, P. Y. Huang, K. F. Mak, C. J. Kim, D. Muller and J. Park, *Nature*, 2015, **520**, 656–660.
238 G. H. Han, N. J. Kybert, C. H. Naylor, B. S. Lee, J. Ping, J. H. Park, J. Kang, S. Y. Lee, Y. H. Lee, R. Agarwal and A. T. Johnson, *Nat. Commun.*, 2015, **6**, 6128–6133.
239 B. Radisavljevic, A. Radenovic, J. Brivio, V. Giacometti and A. Kis, *Nat. Nanotechnol.*, 2011, **6**, 147–150.
240 A. Splendiani, L. Sun, Y. Zhang, T. Li, J. Kim, C. Y. Chim, G. Galli and F. Wang, *Nano Lett.*, 2010, **10**, 1271–1275.
241 Y. Zhang, B. Zheng, C. Zhu, X. Zhang, C. Tan, H. Li, B. Chen, J. Yang, J. Chen, Y. Huang, L. Wang and H. Zhang, *Adv. Mater.*, 2015, **27**, 935–939.
242 C. Zhu, Z. Zeng, H. Li, F. Li, C. Fan and H. Zhang, *J. Am. Chem. Soc.*, 2013, **135**, 5998–6001.
243 L. Sun, H. Hu, D. Zhan, J. Yan, L. Liu, J. S. Teguh, E. K. Yeow, P. S. Lee and Z. Shen, *Small*, 2014, **10**, 1090–1095.
244 J. M. Yun, Y. J. Noh, J. S. Yeo, Y. J. Go, S. I. Na, H. G. Jeong, J. Kim, S. Lee, S. S. Kim, H. Y. Koo, T. W. Kim and D. Y. Kim, *J. Mater. Chem. C*, 2013, **1**, 3777–3783.
245 Y. Zhang, H. Li, L. Wang, H. Wang, X. Xie, S. L. Zhang, R. Liu and Z. J. Qiu, *Sci. Rep.*, 2015, **5**, 7938–7944.
246 J. M. Yun, Y. J. Noh, C. H. Lee, S. I. Na, S. Lee, S. M. Jo, H. I. Joh and D. Y. Kim, *Small*, 2014, **10**, 2319–2324.

247 Y. Zhao, L. Kuai, Y. Liu, P. Wang, H. Arandiyan, S. Cao, J. Zhang, F. Li, Q. Wang, B. Geng and H. Sun, *Sci. Rep.*, 2015, **5**, 8722–8731.
248 H. Li, C. Tsai, A. L. Koh, L. Cai, A. W. Contryman, A. H. Fragapane, J. Zhao, H. S. Han, H. C. Manoharan, F. Abild-Pedersen, J. K. Norskov and X. Zheng, *Nat. Mater.*, 2016, **16**, 48–53.
249 Y. Guo, X. Wei, J. Shu, B. Liu, J. Yin, C. Guan, Y. Han, S. Gao and Q. Chen, *Appl. Phys. Lett.*, 2015, **106**, 103109.
250 S. H. Yu, Y. Lee, S. K. Jang, J. Y. Lee, H. Kim, S. Lee and J. H. Cho, *ACS Nano*, 2014, **8**, 8285–8291.
251 L. Britnell, R. M. Ribeiro, A. Eckmann, R. Jalil, B. D. Belle, A. Mishchenko, Y. J. Kim, R. V. Gorbachev, T. Georgiou, S. V. Morozov, A. N. Grigorenko, A. K. Geim, C. Casiraghi, A. H. Castro Neto and K. S. Novoselov, *Science*, 2013, **340**, 1311–1314.
252 O. Lopez-Sanchez, D. Lembke, M. Kayci, A. Radenovic and A. Kis, *Nat. Nanotechnol.*, 2013, **8**, 497–501.
253 N. Perea-López, A. L. Elías, A. Berkdemir, A. Castro-Beltran, H. R. Gutiérrez, S. Feng, R. Lv, T. Hayashi, F. López-Urías, S. Ghosh, B. Muchharla, S. Talapatra, H. Terrones and M. Terrones, *Adv. Funct. Mater.*, 2013, **23**, 5511–5517.
254 Z. Yin, H. Li, H. Li, L. Jiang, X. Chen and H. Zhang, *ACS Nano*, 2012, **6**, 74–80.
255 M. M. Furchi, D. K. Polyushkin, A. Pospischil and T. Mueller, *Nano Lett.*, 2014, **14**, 6165–6170.
256 J. Schornbaum, B. Winter, S. P. Schießl, F. Gannott, G. Katsukis, D. M. Guldi, E. Spiecker and J. Zaumseil, *Adv. Funct. Mater.*, 2014, **24**, 5798–5806.
257 M. Choi, D. Qu, D. Lee, X. Liu, K. Watanabe, T. Taniguchi and W. J. Yoo, *ACS Nano*, 2014, **8**, 9332–9340.
258 P. Kumbhakar, A. K. Kole, C. S. Tiwary, S. Biswas, S. Vinod, J. Taha-Tijerina, U. Chatterjee and P. M. Ajayan, *Adv. Opt. Mater.*, 2015, **3**, 828–835.
259 A. Woessner, M. B. Lundeberg, Y. Gao, A. Principi, P. Alonso-Gonzalez, M. Carrega, K. Watanabe, T. Taniguchi, G. Vignale, M. Polini, J. Hone, R. Hillenbrand and F. H. Koppens, *Nat. Mater.*, 2015, **14**, 421–425.
260 S. Dai, Z. Fei, Q. Ma, A. S. Rodin, M. Wagner, A. S. Mcleod, M. K. Liu, W. Gannett, W. Regan, K. Watanabe, T. Tanijuchi, M. Thiemens, G. Dominguez, A. H. Castro Neto, A. Zettl, F. Keilmann, P. Jarillo-Herrero, M. M. Fogler and D. N. Basov, *Science*, 2014, **343**, 1125–1129.
261 A. Kumar, T. Low, K. H. Fung, P. Avouris and N. X. Fang, *Nano Lett.*, 2015, **15**, 3172–3180.
262 J. D. Caldwell, A. V. Kretinin, Y. Chen, V. Giannini, M. M. Fogler, Y. Francescato, C. T. Ellis, J. G. Tischler, C. R. Woods, A. J. Giles, M. Hong, K. Watanabe, T. Taniguchi, S. A. Maier and K. S. Novoselov, *Nat. Commun.*, 2014, **5**, 5221–5229.
263 X. Ling, W. Fang, Y. H. Lee, P. T. Araujo, X. Zhang, J. F. Rodriguez-Nieva, Y. Lin, J. Zhang, J. Kong and M. S. Dresselhaus, *Nano Lett.*, 2014, **14**, 3033–3040.
264 P. Alonso-González, A. Y. Nikitin, F. Golmar, A. Centeno, A. Pesquera, S. Vélez, J. Chen, G. Navickaite, F. Koppens, A. Zurutuza, F. Casanova, L. E. Hueso and R. Hillenbrand, *Science*, 2014, **344**, 1369–1373.
265 Z. Fei, A. S. Rodin, W. Gannett, S. Dai, W. Regan, M. Wagner, M. K. Liu, A. S. McLeod, G. Dominguez, M. Thiemens, A. H. Castro Neto, F. Keilmann, A. Zettl, R. Hillenbrand, M. M. Fogler and D. N. Basov, *Nat. Nanotechnol.*, 2013, **8**, 821–825.
266 J. A. Gerber, S. Berweger, B. T. O'Callahan and M. B. Raschke, *Phys. Rev. Lett.*, 2014, **113**, 055502.
267 J. Chen, M. L. Nesterov, A. Y. Nikitin, S. Thongrattanasiri, P. Alonso-Gonzalez, T. M. Slipchenko, F. Speck, M. Ostler, T. Seyller, I. Crassee, F. H. Koppens, L. Martin-Moreno, F. J. Garcia de Abajo, A. B. Kuzmenko and R. Hillenbrand, *Nano Lett.*, 2013, **13**, 6210–6215.
268 M. Schnell, P. S. Carney and R. Hillenbrand, *Nat. Commun.*, 2014, **5**, 3499.
269 M. Polini and F. H. Koppens, *Nat. Mater.*, 2015, **14**, 1187–1188.
270 G. X. Ni, H. Wang, J. S. Wu, Z. Fei, M. D. Goldflam, F. Keilmann, B. Ozyilmaz, A. H. Castro Neto, X. M. Xie, M. M. Fogler and D. N. Basov, *Nat. Mater.*, 2015, **14**, 1217–1222.
271 P. Miro, M. Audiffred and T. Heine, *Chem. Soc. Rev.*, 2014, **43**, 6537–6554.
272 Z. Liu, S. P. Lau and F. Yan, *Chem. Soc. Rev.*, 2015, **44**, 5638–5679.
273 H. Zhang, C. J. Tong, Y. Zhang, Y. N. Zhang and L. M. Liu, *J. Mater. Chem. A*, 2015, **3**, 9632–9637.
274 J. Niu, Y. Jun Shin, Y. Lee, J.-H. Ahn and H. Yang, *Appl. Phys. Lett.*, 2012, **100**, 061116.
275 S. Lee, M. Lee, H. J. Shin and D. Choi, *Nanotechnology*, 2013, **24**, 275702.
276 B. Thackray, V. G. Kravets, F. Schedin, R. Jalil and A. N. Grigorenko, *J. Opt.*, 2013, **15**, 114002.
277 S. G. Zhang, X. W. Zhang, X. Liu, Z. G. Yin, H. L. Wang, H. L. Gao and Y. J. Zhao, *Appl. Phys. Lett.*, 2014, **104**, 121109.
278 G. Xu, J. Liu, Q. Wang, R. Hui, Z. Chen, V. A. Maroni and J. Wu, *Adv. Mater.*, 2012, **24**, OP71–OP76.
279 V. G. Kravets, F. Schedin, R. Jalil, L. Britnell, K. S. Novoselov and A. N. Grigorenko, *J. Phys. Chem. C*, 2012, **116**, 3882–3887.
280 P. Wang, H. He and Y. Jin, *Small*, 2012, **8**, 3438–3442.
281 A. Hoggard, L. Wang, L. Ma, Y. Fang, G. You, J. Olson, Z. Liu, W. Chang, P. M. Ajayan and S. Link, *ACS Nano*, 2013, **7**, 11209–11217.
282 X. Yu, J. Tao, Y. Shen, G. Liang, T. Liu, Y. Zhang and Q. J. Wang, *Nanoscale*, 2014, **6**, 9925–9929.
283 A. Matković, M. Chhikara, M. Milićević, U. Ralević, B. Vasić, D. Jovanović, M. R. Belić, G. Bratina and R. Gajić, *J. Appl. Phys.*, 2015, **117**, 015305.
284 J. Mertens, A. L. Eiden, D. O. Sigle, F. Huang, A. Lombardo, Z. Sun, R. S. Sundaram, A. Colli, C. Tserkezis, J. Aizpurua, S. Milana, A. C. Ferrari and J. J. Baumberg, *Nano Lett.*, 2013, **13**, 5033–5038.
285 T. Atay, J. Song and A. V. Nurmikko, *Nano Lett.*, 2004, **4**, 1627–1631.
286 J. A. Scholl, A. Garcia-Etxarri, A. L. Koh and J. A. Dionne, *Nano Lett.*, 2013, **13**, 564–569.

287 I. Romero, J. Aizpurua, G. W. Bryant and F. J. G. d. Abajo, *Opt. Express*, 2006, **14**, 9988–9999.
288 R. Esteban, A. G. Borisov, P. Nordlander and J. Aizpurua, *Nat. Commun.*, 2012, **3**, 825–833.
289 F. Benz, C. Tserkezis, L. O. Herrmann, B. de Nijs, A. Sanders, D. O. Sigle, L. Pukenas, S. D. Evans, J. Aizpurua and J. J. Baumberg, *Nano Lett.*, 2015, **15**, 669–674.
290 P. T. Bowen and D. R. Smith, *Phys. Rev. B: Condens. Matter Mater. Phys.*, 2014, **90**, 195402.
291 P. Nordlander, *Science*, 2014, **343**, 1444–1445.
292 S. F. Tan, L. Wu, J. K. W. Yang, P. Bai, M. Bosman and C. A. Nijhuis, *Science*, 2014, **343**, 1496–1499.
293 T. Ding, D. Sigle, L. Zhang, J. Mertens, B. de Nijs and J. Baumberg, *ACS Nano*, 2015, **9**, 6110–6118.
294 M. Miyata, A. Holsteen, Y. Nagasaki, M. L. Brongersma and J. Takahara, *Nano Lett.*, 2015, **15**, 5609–5616.
295 A. Sobhani, A. Manjavacas, Y. Cao, M. J. McClain, F. Javier Garcia de Abajo, P. Nordlander and N. J. Halas, *Nano Lett.*, 2015, **15**, 6946–6951.
296 Q. Y. Lin, Z. Li, K. A. Brown, M. N. O'Brien, M. B. Ross, Y. Zhou, S. Butun, P. C. Chen, G. C. Schatz, V. P. Dravid, K. Aydin and C. A. Mirkin, *Nano Lett.*, 2015, **15**, 4699–4703.
297 L. Shao, X. Wang, H. Xu, J. Wang, J. B. Xu, L. M. Peng and H. Q. Lin, *Adv. Opt. Mater.*, 2014, **2**, 162–170.
298 H. Duan, A. I. Fernandez-Dominguez, M. Bosman, S. A. Maier and J. K. Yang, *Nano Lett.*, 2012, **12**, 1683–1689.
299 N. Yamamoto, S. Ohtani and F. J. Garcia de Abajo, *Nano Lett.*, 2011, **11**, 91–95.
300 J. Geldmeier, T. König, M. A. Mahmoud, M. A. El-Sayed and V. V. Tsukruk, *Adv. Funct. Mater.*, 2015, **24**, 6797–6805.
301 J. B. Lassiter, F. McGuire, J. J. Mock, C. Ciracì, R. T. Hill, B. J. Wiley, A. Chilkoti and D. R. Smith, *Nano Lett.*, 2013, **13**, 5866–5872.
302 N. Liu, M. Mesch, T. Weiss, M. Hentschel and H. Giessen, *Nano Lett.*, 2010, **10**, 2342–2348.
303 C. Du, Z. Y. Yao, Y. Q. Chen, H. Bai and L. Li, *RSC Adv.*, 2014, **4**, 9133–9138.
304 S. Mubeen, S. Zhang, N. Kim, S. Lee, S. Kramer, H. Xu and M. Moskovits, *Nano Lett.*, 2012, **12**, 2088–2094.
305 Y. Kang, S. Najmaei, Z. Liu, Y. Bao, Y. Wang, X. Zhu, N. J. Halas, P. Nordlander, P. M. Ajayan, J. Lou and Z. Fang, *Adv. Mater.*, 2014, **26**, 6467–6471.
306 Y. Bao, S. Zu, Y. Zhang and Z. Fang, *ACS Photonics*, 2015, **2**, 1135–1140.
307 J. Kim, H. Son, D. J. Cho, B. Geng, W. Regan, S. Shi, K. Kim, A. Zettl, Y. R. Shen and F. Wang, *Nano Lett.*, 2012, **12**, 5598–5602.
308 H. Qian, Y. Ma, B. Chen, J. Ruan, L. Tong and Z. L. Wang, *ACS Nano*, 2014, **7**, 2584–2589.
309 J. D. Caldwell, I. Vurgaftman, J. G. Tischler, O. J. Glembocki, J. C. Owrutsky and T. L. Reinecke, *Nat. Nanotechnol.*, 2016, **11**, 9–15.
310 M. M. Jadidi, A. B. Sushkov, R. L. Myers-Ward, A. K. Boyd, K. M. Daniels, D. K. Gaskill, M. S. Fuhrer, H. D. Drew and T. E. Murphy, *Nano Lett.*, 2015, **15**, 7099–7104.
311 J. Zhang, L. Zhang and W. Xu, *J. Phys. D: Appl. Phys.*, 2012, **45**, 113001.
312 K. Turcheniuk, R. Boukherroub and S. Szunerits, *J. Mater. Chem. B*, 2015, **3**, 4301–4324.
313 Y. Zhao and Y. Zhu, *Nanoscale*, 2015, **7**, 14561–14576.
314 X. Shi, W. Gu, W. Peng, B. Li, N. Chen, K. Zhao and Y. Xian, *ACS Appl. Mater. Interfaces*, 2014, **6**, 2568–2575.
315 G. Mohanty, B. K. Sahoo and J. Akhtar, *Opt. Quantum Electron.*, 2014, **47**, 1911–1918.
316 L. Wu, H. S. Chu, W. S. Koh and E. P. Li, *Opt. Express*, 2010, **18**, 14395–14400.
317 S. Szunerits, N. Maalouli, E. Wijaya, J. P. Vilcot and R. Boukherroub, *Anal. Bioanal. Chem.*, 2013, **405**, 1435–1443.
318 W. Gao, Y. H. Lee, R. Jiang, J. Wang, T. Liu and X. Y. Ling, *Adv. Mater.*, 2016, **28**, 701–706.
319 Y. Kang, Y. Gong, Z. Hu, Z. Li, Z. Qiu, X. Zhu, P. M. Ajayan and Z. Fang, *Nanoscale*, 2015, **7**, 4482–4488.
320 K. C. Lee, Y. H. Chen, H. Y. Lin, C. C. Cheng, P. Y. Chen, T. Y. Wu, M. H. Shih, K. H. Wei, L. J. Li and C. W. Chang, *Sci. Rep.*, 2015, **5**, 16374.
321 Z. Li, Y. Xiao, Y. Gong, Z. Wang, Y. Kang, S. Zu, P. M. Ajayan, P. Nordlander and Z. Fang, *ACS Nano*, 2015, **9**, 10158–10164.
322 G. M. Akselrod, T. Ming, C. Argyropoulos, T. B. Hoang, Y. Lin, X. Ling, D. R. Smith, J. Kong and M. H. Mikkelsen, *Nano Lett.*, 2015, **15**, 3578–3584.
323 M. J. McClain, A. E. Schlather, E. Ringe, N. S. King, L. Liu, A. Manjavacas, M. W. Knight, I. Kumar, K. H. Whitmire, H. O. Everitt, P. Nordlander and N. J. Halas, *Nano Lett.*, 2015, **15**, 2751–2755.
324 P. Mulpur, R. Podila, K. Lingam, S. K. Vemula, V. K. S. S. Ramamurthy and A. M. Rao, *J. Phys. Chem. C*, 2013, **117**, 17205–17210.
325 J. lee, J. Kim, S. R. Ahmed, H. Zhou, J. Kim and J. Lee, *ACS Appl. Mater. Interfaces*, 2014, **6**, 21380–21388.
326 K. P. Loh, Q. Bao, G. Eda and M. Chhowalla, *Nat. Chem.*, 2010, **2**, 1015–1024.
327 X. Liu, F. Wang, R. Aizen, O. Yehezkeli and I. Willner, *J. Am. Chem. Soc.*, 2013, **135**, 11832–11839.
328 D. Kumar, S. Kaur and D. K. Lim, *Chem. Commun.*, 2014, **50**, 13481–13484.
329 Y. Wen, F. Xing, S. He, S. Song, L. Wang, Y. Long, D. Li and C. Fan, *Chem. Commun.*, 2010, **46**, 2596–2598.
330 X. Fu, T. Lou, Z. Chen, M. Lin, W. Feng and L. Chen, *ACS Appl. Mater. Interfaces*, 2012, **4**, 1080–1086.
331 S. Jiang, Y. Zhang, R. Zhang, C. Hu, M. Liao, Y. Luo, J. Yang, Z. Dong and J. G. Hou, *Nat. Nanotechnol.*, 2015, **10**, 865–869.
332 B. L. Darby, B. Auguié, M. Meyer, A. E. Pantoja and E. C. Le Ru, *Nat. Photonics*, 2015, **10**, 40–45.
333 H. Tang, G. Meng, Q. Huang, Z. Zhang, Z. Huang and C. Zhu, *Adv. Funct. Mater.*, 2012, **22**, 218–224.
334 J. F. Li, Y. F. Huang, Y. Ding, Z. L. Yang, S. B. Li, X. S. Zhou, F. R. Fan, W. Zhang, Z. Y. Zhou, D. Y. Wu, B. Ren, Z. L. Wang and Z. Q. Tian, *Nature*, 2010, **464**, 392–395.

335 C. Hamon, S. M. Novikov, L. Scarabelli, D. M. Solís, T. Altantzis, S. Bals, J. M. Taboada, F. Obelleiro and L. M. Liz-Marzán, *ACS Photonics*, 2015, **2**, 1482–1488.
336 W. Niu, Y. A. Chua, W. Zhang, H. Huang and X. Lu, *J. Am. Chem. Soc.*, 2015, **137**, 10460–10463.
337 S. Huang, X. Ling, L. Liang, Y. Song, W. Fang, J. Zhang, J. Kong, V. Meunier and M. S. Dresselhaus, *Nano Lett.*, 2015, **15**, 2892–2901.
338 X. Ling, L. G. Moura, M. A. Pimenta and J. Zhang, *J. Phys. Chem. C*, 2012, **116**, 25112–25118.
339 W. Xu, N. Mao and J. Zhang, *Small*, 2013, **9**, 1206–1224.
340 E. S. Thrall, A. C. Crowther, Z. Yu and L. E. Brus, *Nano Lett.*, 2012, **12**, 1571–1577.
341 A. C. Ferrari and D. M. Basko, *Nat. Nanotechnol.*, 2013, **8**, 235–246.
342 X. Ling, S. Huang, S. Deng, N. Mao, J. Kong, M. S. Dresselhaus and J. Zhang, *Acc. Chem. Res.*, 2015, **48**, 1862–1870.
343 M. Jiang, Z. Qian, X. Zhou, X. Xin, J. Wu, C. Chen, G. Zhang, G. Xu and Y. Cheng, *Phys. Chem. Chem. Phys.*, 2015, **17**, 21158–21163.
344 X. Liang, B. Liang, Z. Pan, X. Lang, Y. Zhang, G. Wang, P. Yin and L. Guo, *Nanoscale*, 2015, **7**, 20188–20196.
345 H. Hou, P. Wang, J. Zhang, C. Li and Y. Jin, *ACS Appl. Mater. Interfaces*, 2015, **7**, 18038–18045.
346 C. Hu, J. Rong, J. Cui, Y. Yang, L. Yang, Y. Wang and Y. Liu, *Carbon*, 2013, **51**, 255–264.
347 T. H. D. Nguyen, Z. Zhang, A. Mustapha, H. Li and M. Lin, *J. Agric. Food Chem.*, 2014, **62**, 10445–10451.
348 K. Long, X. Luo, H. Nan, D. Du, W. Zhao, Z. Ni and T. Qiu, *J. Appl. Phys.*, 2013, **114**, 183520.
349 P. Wang, W. Zhang, O. Liang, M. Pantoja, J. Katzer, T. Schroeder and Y. Xie, *ACS Nano*, 2012, **6**, 6244–6249.
350 P. Wang, M. Xia, O. Liang, K. Sun, A. F. Cipriano, T. Schroeder, H. Liu and Y. H. Xie, *Anal. Chem.*, 2015, **87**, 10255–10261.
351 G. Jalani and M. Cerruti, *Nanoscale*, 2015, **7**, 9990–9997.
352 J. F. Li, J. R. Anema, T. Wandlowski and Z. Q. Tian, *Chem. Soc. Rev.*, 2015, **44**, 8399–8409.
353 Y. Zhao, W. Zeng, Z. Tao, P. Xiong, Y. Qu and Y. Zhu, *Chem. Commun.*, 2015, **51**, 866–869.
354 J. Wu, Y. Xu, P. Xu, Z. Pan, S. Chen, Q. Shen, L. Zhan, Y. Zhang and W. Ni, *Nanoscale*, 2015, **7**, 17529–17537.
355 B. Duan, J. Zhou, Z. Fang, C. Wang, X. Wang, H. F. Hemond, M. B. Chan-Park and H. Duan, *Nanoscale*, 2015, **7**, 12606–12613.
356 X. Zhang, C. Shi, E. Liu, J. Li, N. Zhao and C. He, *Nanoscale*, 2015, **7**, 17079–17087.
357 S. Yang, Z. Zhang, J. Zhao, Z. Yu and H. Jiang, *Mater. Lett.*, 2014, **131**, 78–81.
358 H. Zhou, F. Yu, C. F. Guo, Z. Wang, Y. Lan, G. Wang, Z. Fang, Y. Liu, S. Chen, L. Sun and Z. Ren, *Nanoscale*, 2015, **7**, 9153–9157.
359 Q. Cai, L. H. Li, Y. Yu, Y. Liu, S. Huang, Y. Chen, K. Watanabe and T. Taniguchi, *Phys. Chem. Chem. Phys.*, 2015, **17**, 7761–7766.
360 Y. Sun, K. Liu, X. Hong, M. Chen, J. Kim, S. Shi, J. Wu, A. Zettl and F. Wang, *Nano Lett.*, 2014, **14**, 5329–5334.
361 W. Zhu and K. B. Crozier, *Nat. Commun.*, 2014, **5**, 5228.
362 K. J. Savage, M. M. Hawkeye, R. Esteban, A. G. Borisov, J. Aizpurua and J. J. Baumberg, *Nature*, 2012, **491**, 574–577.
363 C. Ciraci, R. T. Hill, J. J. Mock, Y. Urzhumov, A. I. Fernandez-Dominguez, S. A. Maier, J. B. Pendry, A. Chilkoti and D. R. Smith, *Science*, 2012, **337**, 1072–1074.
364 V. Kravtsov, S. Berweger, J. M. Atkin and M. B. Raschke, *Nano Lett.*, 2014, **14**, 5270–5275.
365 D. D. Sigle, J. Mertens, L. O. Herrmann, R. W. Bowman, S. Ithurria, B. Dubertret, Y. Shi, H. Y. Yang, C. Tserkezis, J. Aizpurua and J. J. Baumberg, *ACS Nano*, 2015, **9**, 825–830.
366 H. Zhang, Y. Sun, S. Gao, J. Zhang, H. Zhang and D. Song, *Small*, 2013, **9**, 2537–2540.
367 N. Chiu, T. Huang, H. Lai and K. Liu, *Nanoscale Res. Lett.*, 2014, **9**, 445–451.
368 Y. Ryu, S. Moon, Y. Oh, Y. Kim, T. Lee, D. H. Kim and D. Kim, *Appl. Opt.*, 2014, **53**, 1419–1426.
369 O. Salihoglu, S. Balci and C. Kocabas, *Appl. Phys. Lett.*, 2012, **100**, 213110.
370 M. Singh, M. Holzinger, M. Tabrizian, S. Winters, N. C. Berner, S. Cosnier and G. S. Duesberg, *J. Am. Chem. Soc.*, 2015, **137**, 2800–2803.
371 S. Zeng, K. V. Sreekanth, J. Shang, T. Yu, C. K. Chen, F. Yin, D. Baillargeat, P. Coquet, H. P. Ho, A. V. Kabashin and K. T. Yong, *Adv. Mater.*, 2015, **27**, 6163–6169.
372 Q. Xiang, B. Cheng and J. Yu, *Angew. Chem., Int. Ed.*, 2015, **54**, 11350–11366.
373 A. Penezic, G. Deokar, D. Vignaud, E. Pichonat, H. Happy, P. Subramanian, B. Gasparović, R. Boukherroub and S. Szunerits, *Plasmonics*, 2014, **9**, 677–683.
374 C. Sönnichsen, T. Franzl, T. Wilk, G. von Plessen, J. Feldmann, O. Wilson and P. Mulvaney, *Phys. Rev. Lett.*, 2002, **88**, 077402.
375 A. Primo, A. Corma and H. Garcia, *Phys. Chem. Chem. Phys.*, 2011, **13**, 886–910.
376 A. Primo, T. Marino, A. Corma, R. Molinari and H. Garcia, *J. Am. Chem. Soc.*, 2011, **133**, 6930–6933.
377 D. Tsukamoto, Y. Shiraishi, Y. Sugano, S. Ichikawa, S. Tanaka and T. Hirai, *J. Am. Chem. Soc.*, 2012, **134**, 6309–6315.
378 S. Naya, A. Inoue and H. Tada, *J. Am. Chem. Soc.*, 2010, **132**, 6292–9293.
379 H. Liu, J. Wang, Z. Feng, Y. Lin, L. Zhang and D. Su, *Small*, 2015, **11**, 5059–5064.
380 M. Zhou, J. Li, Z. Ye, C. Ma, H. Wang, P. Huo, W. Shi and Y. Yan, *ACS Appl. Mater. Interfaces*, 2015, **7**, 28231–28243.
381 S. T. Kochuveedu, Y. H. Jang and D. H. Kim, *Chem. Soc. Rev.*, 2013, **42**, 8467–8493.
382 Y. Shi, J. Wang, C. Wang, T. T. Zhai, W. J. Bao, J. J. Xu, X. H. Xia and H. Y. Chen, *J. Am. Chem. Soc.*, 2015, **137**, 7365–7370.
383 Z. Yin, B. Chen, M. Bosman, X. Cao, J. Chen, B. Zheng and H. Zhang, *Small*, 2014, **10**, 3537–3543.

384 P. Zhang, T. Wang and J. Gong, *Adv. Mater.*, 2015, **27**, 5328–5342.
385 A. J. Cheah, W. S. Chiu, P. S. Khiew, H. Nakajima, T. Saisopa, P. Songsiriritthigul, S. Radiman and M. A. A. Hamid, *Catal. Sci. Technol.*, 2015, **5**, 4133–4143.
386 F. Schwierz, *Nat. Nanotechnol.*, 2010, **5**, 487–496.
387 H. Tang, C. M. Hessel, J. Wang, N. Yang, R. Yu, H. Zhao and D. Wang, *Chem. Soc. Rev.*, 2014, **43**, 4281–4299.
388 J. J. Shao, W. Lv and Q. H. Yang, *Adv. Mater.*, 2014, **26**, 5586–5612.
389 M. K. Chuang, S. W. Lin, F. C. Chen, C. W. Chu and C. S. Hsu, *Nanoscale*, 2014, **6**, 1573–1579.
390 B. Deng, P. C. Hsu, G. Chen, B. N. Chandrashekar, L. Liao, Z. Ayitimuda, J. Wu, Y. Guo, L. Lin, Y. Zhou, M. Aisijiang, Q. Xie, Y. Cui, Z. Liu and H. Peng, *Nano Lett.*, 2015, **15**, 4206–4213.
391 P. K. Mohseni, A. Behnam, J. D. Wood, X. Zhao, K. J. Yu, N. C. Wang, A. Rockett, J. A. Rogers, J. W. Lyding, E. Pop and X. Li, *Adv. Mater.*, 2014, **26**, 3755–3760.
392 I. N. Kholmanov, C. W. Magnuson, A. E. Aliev, H. Li, B. Zhang, J. W. Suk, G. Shvets and R. S. Ruoff, *Nano Lett.*, 2012, **12**, 5679–5683.
393 K. K. Kim, A. Reina, Y. Shi, H. Park, L. J. Li, Y. H. Lee and J. Kong, *Nanotechnology*, 2010, **21**, 285205.
394 C. Jeong, P. Nair, M. Khan, M. Lundstrom and M. A. Alam, *Nano Lett.*, 2011, **11**, 5020–5025.
395 M. Lee, K. Lee, S. Kim, H. Lee, J. Park, K. Choi, H. Kim, D. Kim, D. Lee, S. Nam and J. Park, *Nano Lett.*, 2013, **13**, 2814–2821.
396 I. N. Kholmanov, S. H. Domingues, H. Chou, X. Wang, C. Tan, J. Kim, H. Li, R. Piner, A. J. G. Zarbin and R. S. Ruoff, *ACS Nano*, 2013, **7**, 1811–1816.
397 A. R. B. Mohd Yusoff, D. Kim, F. K. Schneider, W. J. da Silva and J. Jang, *Energy Environ. Sci.*, 2015, **8**, 1523–1537.
398 Q. Zhang, Y. Di, C. M. Huard, L. J. Guo, J. Wei and J. Guo, *J. Mater. Chem. C*, 2015, **3**, 1528–1536.
399 Y. Shi, K. Kang. Kim, A. Reina, M. Hofmann, L. Li and J. Kong, *ACS Nano*, 2010, **4**, 2689–2694.
400 P. Ho, Y. Liou, C. Chuang, S. Lin, C. Tseng, D. Wang, C. Chen, W. Hung, C. Wen and C. Chen, *Adv. Mater.*, 2015, **27**, 1724–1729.
401 X. Liu, X. W. Zhang, Z. G. Yin, J. H. Meng, H. L. Gao, L. Q. Zhang, Y. J. Zhao and H. L. Wang, *Appl. Phys. Lett.*, 2014, **105**, 183901.
402 G. Q. Fan, Q. Q. Zhuo, J. J. Zhu, Z. Q. Xu, P. P. Cheng, Y. Q. Li, X. H. Sun, S. T. Lee and J. X. Tang, *J. Mater. Chem.*, 2012, **22**, 15614–15619.
403 Z. Liu, K. Parvez, R. Li, R. Dong, X. Feng and K. Mullen, *Adv. Mater.*, 2014, **27**, 669–675.
404 K. Jiao, C. Duan, X. Wu, J. Chen, Y. Wang and Y. Chen, *Phys. Chem. Chem. Phys.*, 2015, **17**, 8182–8186.
405 X. Li, W. Zhang, Y. Wu, C. Min and J. Fang, *ACS Appl. Mater. Interfaces*, 2013, **5**, 8823–8827.
406 X. Yang, W. Fu, W. Liu, J. Hong, Y. Cai, C. Jin, M. Xu, H. Wang, D. Yang and H. Chen, *J. Mater. Chem. A*, 2014, **2**, 7727–7733.
407 P. Qin, G. Fang, W. Ke, F. Cheng, Q. Zheng, J. Wan, H. Lei and X. Zhao, *J. Mater. Chem. A*, 2014, **2**, 2742–2756.
408 X. Li, W. C. H. Choy, X. Ren, J. Xin, P. Lin and D. C. W. Leung, *Appl. Phys. Lett.*, 2013, **102**, 153304.
409 X. H. Li, W. C. H. Choy, H. F. Lu, W. E. I. Sha and A. H. P. Ho, *Adv. Funct. Mater.*, 2013, **23**, 2728–2735.
410 M. Shanmugam, T. Bansal, C. A. Durcan and B. Yu, *Appl. Phys. Lett.*, 2012, **100**, 153901.
411 J. Weiss, M. Thomalla and H. Tributsch, *J. Photochem. Photobiol., A*, 2013, **255**, 36–40.
412 A. Bruno, C. Borriello, S. A. Haque, C. Minarini and T. Di Luccio, *Phys. Chem. Chem. Phys.*, 2014, **16**, 17998–18003.
413 M. Thomalla and H. Tributsch, *J. Phys. Chem. B*, 2006, **110**, 12167–12171.
414 G. Xu, R. Lu, J. Liu, H. Y. Chiu, R. Hui and J. Z. Wu, *Adv. Opt. Mater.*, 2014, **2**, 729–736.
415 F. Schwierz, J. Pezoldt and R. Granzner, *Nanoscale*, 2015, **7**, 8261–8283.
416 J. Zhang, Z. Zhu, W. Liu, X. Yuan and S. Qin, *Nanoscale*, 2015, **7**, 13530–13536.
417 J. T. Ye, S. Inoue, K. Kobayashi, Y. Kasahara, H. T. Yuan, H. Shimotani and Y. Iwasa, *Nat. Mater.*, 2010, **9**, 125–128.
418 W. Wang, A. Klots, D. Prasai, Y. Yang, K. I. Bolotin and J. Valentine, *Nano Lett.*, 2015, **15**, 7440–7444.
419 J. Lin, H. Li, H. Zhang and W. Chen, *Appl. Phys. Lett.*, 2013, **102**, 203109.
420 J. Miao, W. Hu, Y. Jing, W. Luo, L. Liao, A. Pan, S. Wu, J. Cheng, X. Chen and W. Lu, *Small*, 2015, **11**, 2392–2398.
421 S. R. Tamalampudi, Y. Y. Lu, U. R. Kumar, R. Sankar, C. D. Liao, B. K. Moorthy, C. H. Cheng, F. C. Chou and Y. T. Chen, *Nano Lett.*, 2014, **14**, 2800–2806.
422 P. Hu, Z. Wen, L. Wang, P. Tan and K. Xiao, *ACS Nano*, 2012, **6**, 5988–5994.
423 P. Hu, L. Wang, M. Yoon, J. Zhang, W. Feng, X. Wang, Z. Wen, J. C. Idrobo, Y. Miyamoto, D. B. Geohegan and K. Xiao, *Nano Lett.*, 2013, **13**, 1649–1654.
424 L. Hu, M. M. Brewster, X. Xu, C. Tang, S. Gradecak and X. Fang, *Nano Lett.*, 2013, **13**, 1941–1947.
425 S. Zhang, H. Li, Z. Wang, J. Liu, H. Zhang, B. Wang and Z. Yang, *Nanoscale*, 2015, **7**, 8495–8502.
426 L. Zhan, C. M. Li, W. B. Wu and C. Z. Huang, *Chem. Commun.*, 2014, **50**, 11526–11528.
427 D. K. Lim, A. Barhoumi, R. G. Wylie, G. Reznor, R. S. Langer and D. S. Kohane, *Nano Lett.*, 2013, **13**, 4075–4079.
428 X. Li, Y. Zhang, Y. Wu, Y. Duan, X. Luan, Q. Zhang and Q. An, *ACS Appl. Mater. Interfaces*, 2015, **7**, 19353–19361.
429 Y. K. Kim, H. K. Na, S. Kim, H. Jang, S. J. Chang and D. H. Min, *Small*, 2015, **11**, 2527–2535.
430 S. Linic, U. Aslam, C. Boerigter and M. Morabito, *Nat. Mater.*, 2015, **14**, 567–576.
431 H. Moon, D. Kumar, H. Kim, C. Sim and D. K. Lim, *ACS Nano*, 2015, **9**, 2711–2719.
432 J. Ma, G. Xie, P. Lv, W. Gao, P. Yuan, L. Qian, U. Griebner, V. Petrov, H. Yu, H. Zhang and J. Wang, *Sci. Rep.*, 2014, **4**, 5016–5021.

433 F. Xiong, J. Zhang, Z. Zhu, X. Yuan and S. Qin, *Sci. Rep.*, 2015, **5**, 16998.
434 J. Kim, M. S. Lee, S. Jeon, M. Kim, S. Kim, K. Kim, F. Bien, S. Y. Hong and J. U. Park, *Adv. Mater.*, 2015, **27**, 3292–3297.
435 Z. Huang, T. Koschny and C. M. Soukoulis, *Phys. Rev. Lett.*, 2012, **108**, 187402.
436 A. Marimuthu, J. Zhang and S. Linic, *Science*, 2013, **339**, 1590–1593.
437 Y. Ide, N. Kawamoto, Y. Bando, H. Hattori, M. Sadakane and T. Sano, *Chem. Commun.*, 2013, **49**, 3652–3654.
438 S. i. Naya, K. Kimura and H. Tada, *ACS Catal.*, 2013, **3**, 10–13.
439 R. L. Cropley, F. J. Williams, A. J. Urquhart, O. P. H. Vaughan, M. S. Tikhov and R. M. Lambert, *J. Am. Chem. Soc.*, 2005, **127**, 6069–6076.
440 F. Li, S.-F. Zhao, L. Chen, A. Khan, D. R. MacFarlane and J. Zhang, *Energy Environ. Sci.*, 2016, **9**, 216–223.
441 A. Dhakshinamoorthy, A. A. C. Sergio Navalon and H. Garcia, *Energy Environ. Sci.*, 2012, **5**, 9217–9233.
442 C. An, J. Wang, W. Jiang, M. Zhang, X. Ming, S. Wang and Q. Zhang, *Nanoscale*, 2012, **4**, 5646–5650.
443 B. D. Mankidy, B. Joseph and V. K. Gupta1, *Nanotechnology*, 2013, **24**, 405402.
444 C. Wang, O. Ranasingha, S. Natesakhawat, J. Paul, R. Ohodnicki, M. Andio, J. P. Lewisac and C. Matranga, *Nanoscale*, 2013, **5**, 6968–6974.
445 V. P. Indrakanti, J. D. Kubicki and H. H. Schobert, *Energy Environ. Sci.*, 2009, **2**, 745–758.
446 S. Gao, Y. Lin, X. Jiao, Y. Sun, Q. Luo, W. Zhang, D. Li, J. Yang and Y. Xie, *Nature*, 2016, **529**, 68–71.